



**HAL**  
open science

# Hybrid circuit quantum electrodynamics with a hole spin in silicon

Cécile Yu

► **To cite this version:**

Cécile Yu. Hybrid circuit quantum electrodynamics with a hole spin in silicon. Condensed Matter [cond-mat]. Université Grenoble Alpes [2020-..], 2022. English. NNT: 2022GRALY053. tel-03907697

**HAL Id: tel-03907697**

**<https://theses.hal.science/tel-03907697v1>**

Submitted on 20 Dec 2022

**HAL** is a multi-disciplinary open access archive for the deposit and dissemination of scientific research documents, whether they are published or not. The documents may come from teaching and research institutions in France or abroad, or from public or private research centers.

L'archive ouverte pluridisciplinaire **HAL**, est destinée au dépôt et à la diffusion de documents scientifiques de niveau recherche, publiés ou non, émanant des établissements d'enseignement et de recherche français ou étrangers, des laboratoires publics ou privés.

THÈSE

Pour obtenir le grade de

**DOCTEUR DE L'UNIVERSITÉ GRENOBLE ALPES**

École doctorale : PHYS - Physique

Spécialité : Physique de la Matière Condensée et du Rayonnement

Unité de recherche : PHotonique, ELelectronique et Ingénierie QuantiqueS

## **Electrodynamique quantique en circuit hybride avec un spin de trou dans le silicium**

### **Hybrid circuit quantum electrodynamics with a hole spin in silicon**

Présentée par :

**Cécile YU**

Direction de thèse :

**Silvano DE FRANCESCHI**

INGENIEUR HDR, Université Grenoble Alpes

Directeur de thèse

**Romain MAURAND**

INGENIEUR CHERCHEUR, Université Grenoble Alpes

Co-encadrant de thèse

**Benoit BERTRAND**

CEA Grenoble

Co-encadrant de thèse

Rapporteurs :

**GUIDO BURKARD**

Professeur, Universität Konstanz

**THOMAS IHN**

Professeur, Ecole Polytechnique Fédérale de Zurich

Thèse soutenue publiquement le **15 septembre 2022**, devant le jury composé de :

**GUIDO BURKARD**

Professeur, Universität Konstanz

Rapporteur

**THOMAS IHN**

Professeur, Ecole Polytechnique Fédérale de Zurich

Rapporteur

**ANDREAS FUHRER**

Docteur en sciences, IBM Research

Examineur

**HERVE COURTOIS**

Professeur des Universités, UNIVERSITE GRENOBLE ALPES

Président

**JEREMIE VIENNOT**

Chargé de recherche, CNRS DELEGATION ALPES

Examineur

Invités :

**ROMAIN MAURAND**

Ingénieur de recherche, CEA CENTRE DE GRENOBLE



致我最亲爱的妈妈。

# Abstract

Coherent and strong coupling between photons and solid-state qubits, in the form of circuit quantum electrodynamics (QED), has been harnessed for two-qubit gates mediated by photons and high-fidelity quantum non-demolition readout, which are the building blocks of large-scale quantum computation. Recently, circuit QED has been extended to gate-defined semiconductor quantum dots. In this thesis, we develop a novel hybrid circuit QED architecture composed of a high-impedance superconducting microwave resonator and spins localized in silicon-MOS quantum dots. To control and measure the spin degrees of freedom, this hybrid system needs to operate at finite magnetic field. Consequently, we develop and characterize microwave resonators based on thin niobium nitride (NbN) films featuring a high kinetic inductance. We demonstrate the magnetic field resilience and low photon loss rates of high-impedance resonators. We then co-integrate the NbN resonators on silicon spin qubit chips. With a hole confined in a double quantum dot (DQD), we report the first realization of a strong hole charge-photon interaction bordering the ultra-strong coupling regime. At finite magnetic field, putting the spin transition energy in resonance with the microwave cavity, we observe large vacuum Rabi mode splittings, signature of a strong spin-photon coupling. Our findings are well captured by the modelling of a hole in a DQD with different anisotropic Zeeman response in each dot and spin-orbit coupling dependent tunnel rates. We also find a sizeable spin-photon coupling when the hole is localized in the single quantum dot, in line with recent theoretical predictions. The different works presented in this manuscript pave the way for circuit QED with hole spins in gate-defined semiconductor quantum dots.

## Résumé

Le couplage cohérent et fort entre les photons et les qubits basés sur des matériaux solides, sous la forme de l'électrodynamique quantique de circuit (en anglais circuit QED), a été exploité notamment pour les portes logiques à deux qubits et la lecture haute fidélité sans démolition d'état formant les blocs fondateurs du calcul quantique. Récemment, la circuit QED a été étendue aux boîtes quantiques définies par des grilles dans des matériaux semiconducteurs. Dans cette thèse, nous développons une nouvelle architecture hybride de circuit QED composée d'un résonateur micro-onde supraconducteur à haute impédance et de spins localisés dans des boîtes quantiques en silicium-MOS. Afin de contrôler et mesurer le degré de liberté de spin, ce système hybride doit opérer dans un champ magnétique fini. Par conséquent, nous avons développé et caractérisé des résonateurs à haute impédance micro-ondes formés dans un film mince de nitrure de niobium (NbN) comportant une haute inductance cinétique. Nous avons démontré que ces résonateurs résistent à de forts champs magnétiques tout en gardant une faible perte de photons. Nous avons ensuite co-intégré ces résonateurs sur les puces des qubits de spin en silicium. Avec le confinement d'un trou dans une double boîte quantique, nous présentons ici la première démonstration d'une interaction forte entre une charge de trou et un photon à la limite du régime de couplage ultra-fort. Sous champ magnétique fini, nous avons observé des répulsions des états de Rabi du vide caractéristiques d'un couple fort spin-photon. Nos résultats sont bien reproduits par la modélisation d'un trou dans une double boîte quantique avec une réponse anisotrope différente dans chaque boîte et des taux de tunnel dépendants du couplage spin-orbite. Nous avons également mesuré un couplage spin-photon conséquent lorsque le trou est localisé dans une boîte quantique unique, en accord avec les prédictions théoriques récentes. Ces différents travaux présentés dans ce manuscrit ouvrent la voie à une circuit QED avec des spins de trous dans une boîte quantique semi-conductrice définie par des grilles.

## Acknowledgements

As a master student, I would never imagine myself starting a PhD but now I have almost completed this journey. I regret nothing about this decision four years after (maybe just the COVID-19) and I would like to thank warmly all the people who have played an important role in it. My time in Grenoble would not be as great without you.

I would like to first thank my supervisor **Romain** who trusted me four years ago, while at this time I didn't even know what a spin qubit is. I have been pushed by your enthusiasm even if it had led us to some obscure results at the beginning, but finally our efforts have been rewarded. You always know how to explain the complicated physics with simple words and hand waving arguments. Thank you also for your encouragements each time I started to doubt myself.

Thank you **Simon** for joining this spin-photon project. You have always shown patience and pedagogy to my questions, even the dumbest ones. Thank you for building and taking care of our dilution fridge, **Blue Lagoon**. You have taught me everything in the lab from soldering a cable to measuring a spin qubit. Thank you also for being a good friend outside the lab, in a bar or in the mountains (even if you never wanted to build an igloo with me).

A special word goes to **Marc** who has left us in 2021. Until the end, you have shown your scientific and human support. Thank you **Silvano** for accepting being my PhD director, it was always good to benefit from your infinite knowledge of the solid-state physics.

Thank you **Frederic** for teaching me all the secrets of nano-fabrication. Thanks to your involvement, we have brought this co-integration project to its success. Also thank you **Jean-Luc** for doing a weekly e-beam lithography for us, I know that our devices are not the simplest but you have always managed to perform the lithography in time. By the way, sorry **Jean-Luc** but I have never stopped being the girl from Paris and would never wear a Quechua fleece jacket at work.

I also want to thank **Yann-Michel** for providing the theoretical support to us, along with **José** and **Vincent** for modeling our spin-photon platform. It has always been a pleasure to discuss about the results together. Thank you for your effort in explaining without any Hamiltonian.

Thank you also the quantum silicon team of CEA-LETI, especially **Benoit**, **Heimanu**, **Niels**, **Thomas B.** and **Maud**. Thank you for keep improving the quality of the quantum dots and making the necessary changes in the fabrication process on the 300 mm such that this spin-photon project is possible.

CEA is a complicated administrative bubble, and **Marielle** knows all the cheat codes to survive there. Thank you for your help in all the paper works.

Thank you also **Michel** for all the mechanical pieces you have made for our measurement set-up and all the screws you have provided, without which we would not be able to settle up the experiment.

I am also grateful for the help from our colleagues in the D5 building, especially **Karine** for performing the annealing of our sample.

I would also like to thank **Franck Balestro** at Néel Institute for letting me use one of his dilution fridge to perform the first experiments on the superconducting resonators with the help of **Jéréemie Viennot**. I am also grateful of the discussions we had with **Nicolas Roch** who has shared with us his knowledge about microwave engineering and thank you also for being a member of CSI. I would also like to thank **Louis Hutin** for providing us the first transistors of this project and also for being a member of CSI and the valuable advice you gave me regarding the end of my PhD.

I would also like to thank all the permanents of the LATEQS group, **Xavier** (I really love your jokes in meetings or e-mails and thank you for being our IT guardian), **Etienne** (I hope that one day you will have a lama!), **Louis, Vincent** (thank you for giving me the opportunity to teach and thank you for your encouragements when I lose confidence), **Claude** and **Christophe**, but also from IMAPEC group, **Jean-Pascal, Iulian, Georg, Alexandre** and **Daniel** and our favorite theoretician **Michele**. It has always been a pleasure to chat with you around the coffee machine, either about scientific topics or not.

This journey would not be the same without my great colleagues, but most importantly friends. Starting from the generation before me, thank you **Romain A., Florian V., Florian B., Thomas, Anthony** and **Estelle M.** for inviting me at board game parties and hiking when I first arrived in Grenoble. Especially, thank you **Romain A.** for letting me discover the pleasure of sleeping in a tent after walking 20km with more than 1000m of elevation. And **Thomas**, but also **Claire**, for the bivouacs, barbecues or just dinners together even after you have finished your PhDs.

Thank you **Estelle V.** and **Gonzalo** for sharing the office with me and for our dinners and board game parties together. I wish you all the best for the future, either in Antarctic or on a sunny island.

**Nicolas**, even if your presentation about the darts game was crap, it was actually a good idea to buy one for the coffee room. You were never brought down by the challenges of your experiment and kept coming to work with a shirt even if we were all laughing at your way of dressing. Good luck for the end of your PhD, you are very close to the finishing line!

**Florie**, thank you for the dinners at your place, movie sessions with **Martin** and all the outdoors activities we did together from chestnuts hunting to ski touring during the hard COVID times. I am such a big fan of you, I admire your endless energy and cheerfulness. You will be a great scientist!

Thank you **Marion** for finding a badminton club in Grenoble, at that time I didn't know how much I would like this sport. I also enjoyed a lot talking with you in or outside the lab about anything.

Thank you **Victor M.** for being a great colleague but also a great badminton partner, even if we haven't won a single match yet. You are always available to help anyone who is in need but sometimes don't forget to focus on yourself!

**Chotivut** thank you for let us discover the thai cuisine and good luck with all the French administrative things!

**Vivien**, or chef Vivi now, you are the handyman of this lab but also a very good partner at darts game. Going at the March Meeting in Chicago with you was a great experience, I enjoyed collecting the goodies together and thank you for introducing me to your Australian and Delft friends there.

**Boris** you are such a great scientist and adventurer. I loved watching you flying with your para-glider during our lab ski days and discussing about the itinerary of going on a bike trip. By the way I really love the sirwall!

I have also enjoyed all the time I have spent in the lab or outside with **Tom**, **Rami**, **Agostino**, **Alessandro**, **Marco**, **Zoltan**, **Valentin** and **James**, but also the theoreticians **Biel**, **Esteban** Eventually, good luck to the next generation of PhDs in the group **Nathan**, **Elyjah**, **Victor C.**, **Axel**, **Thomas H.** and **Nesrine**. A special thought goes to **Léo** who is taking over this spin-photon experiment. You will be doing great and the two-qubit gates is yours (with the help of **Simon** of course)!

**Baptiste**, we were bold enough to move in together in Grenoble four years ago. Since then, we have experienced confinements together and even adopted our lovely **Yuzu**. Now let's move on forwards and face the future challenges together, namely the absence of mountains around and the rain.

I also want to thank my **family** for their support during all these years. Especially, thank you **Mama** for always being proud of me!

Last but not least, I would like to thank the members of the jury, **Thomas Ihn**, **Guido Burkard**, **Andreas Fuhrer**, **Hervé Courtois** and **Jérémie Viennot**, for reviewing this work and attending the defense. Thank you for all of your questions and remarks during the defense.





# CONTENTS

	Page
<b>List of Figures</b>	<b>xiii</b>
<b>List of Tables</b>	<b>xvii</b>
<b>Introduction</b>	<b>1</b>
<b>1 Circuit quantum electrodynamics with Si hole spins</b>	<b>5</b>
1.1 Superconducting coplanar waveguide resonators . . . . .	6
1.1.1 Transmission line model . . . . .	6
1.1.2 Coplanar waveguides . . . . .	7
1.1.3 Half-wavelength CPW resonators . . . . .	9
1.2 Light matter interaction in circuit QED . . . . .	12
1.2.1 Jaynes-Cummings Hamiltonian . . . . .	12
1.2.2 Dressed eigenstates . . . . .	15
1.2.3 Strong coupling regime . . . . .	17
1.3 Circuit QED with a charge qubit . . . . .	17
1.3.1 Quantum dots physics . . . . .	17
1.3.2 Charge-photon coupling via electric-dipole interaction . . . . .	22
1.4 Circuit QED with a hole spin . . . . .	24
1.4.1 Hole spin in a DQD . . . . .	25
1.4.2 Rashba spin-orbit coupling (SOC) . . . . .	28
1.4.3 Spin-photon coupling via intrinsic SOC . . . . .	29
<b>2 Experimental methods</b>	<b>33</b>
2.1 Si-MOS quantum dots fabrication . . . . .	34
2.1.1 Silicon spin qubits architecture . . . . .	34
2.1.2 Fabrication . . . . .	36
2.2 Thin NbN films . . . . .	39
2.2.1 Film growth parameters . . . . .	40
2.2.2 Film characterization . . . . .	41

2.3	Co-integration of superconducting coplanar waveguide resonators with quantum dots . . . . .	45
2.3.1	Resonators design . . . . .	45
2.3.2	Co-integration fabrication flow . . . . .	46
2.4	Measurement set-up . . . . .	49
<b>3</b>	<b>NbN superconducting resonators in the coplanar waveguide geometry</b>	<b>55</b>
3.1	NbN superconducting resonators characterizations on Si substrates	56
3.1.1	Basic characterization . . . . .	56
3.1.2	Power dependence . . . . .	58
3.1.3	Magnetic fields resilience . . . . .	60
3.2	Extra microwave challenges in the cQED geometry . . . . .	63
3.2.1	Influence of the substrate . . . . .	63
3.2.2	Microwave leakage due to additional gate lines . . . . .	65
<b>4</b>	<b>Dispersive coupling of a single hole to a single photon</b>	<b>71</b>
4.1	Characterisation of the hybrid system . . . . .	73
4.1.1	Nanowire transistor characterization . . . . .	73
4.1.2	Superconducting resonator characterization . . . . .	74
4.2	Charge-photon interaction . . . . .	76
4.2.1	Characterisation of a double quantum dot . . . . .	76
4.2.2	Dispersive charge/photon strong coupling . . . . .	79
<b>5</b>	<b>Strong hole spin-photon coupling</b>	<b>85</b>
5.1	Strong single spin-photon coupling . . . . .	86
5.2	Anisotropic Zeeman response of the hole spin . . . . .	89
5.2.1	Detuning-magnetic field maps . . . . .	89
5.2.2	In-plane g-factors of the dots . . . . .	91
5.3	Modulation of the spin-photon coupling strength . . . . .	92
5.3.1	Magnetic field angular dependence of $g_s$ . . . . .	92
5.3.2	Spin-photon coupling model . . . . .	96
5.3.3	Single quantum dot regime . . . . .	97
5.4	Spin decoherence . . . . .	100
5.4.1	Two-tone spectroscopy . . . . .	100
5.4.2	Noise estimation . . . . .	102
	<b>Conclusion and perspectives</b>	<b>105</b>
	<b>Appendix A Input-output theory</b>	<b>107</b>
	<b>Appendix B Fabrication Recipes</b>	<b>111</b>
B.1	Alignment crosses . . . . .	111
B.2	Resonators fabrication . . . . .	111
B.2.1	NbN deposition . . . . .	111

B.2.2	E-beam Lithography . . . . .	112
B.2.3	Plasma etching . . . . .	112
B.2.4	Resist removal . . . . .	114
B.2.5	Dicing . . . . .	114
B.2.6	Annealing . . . . .	115
<b>Appendix C Kinetic inductance extraction by two-tone spectroscopy</b>		<b>117</b>
<b>Appendix D Average number of photons in a <math>\lambda/2</math> resonator</b>		<b>119</b>
D.1	Derivation of $V_{RLC}$ . . . . .	120
D.2	Derivation of resonator impedance . . . . .	121
D.3	The resonance shift . . . . .	121
D.4	Coupling quality factor . . . . .	122
D.5	Average number of photons in a $\lambda/2$ resonator . . . . .	122
<b>Publications</b>		<b>125</b>
<b>Bibliography</b>		<b>127</b>



# LIST OF FIGURES

1.1	Lumped-element circuit model for an infinitesimal length $\Delta z$ of a transmission line with the resistance $R$ , inductance $L$ , capacitance $C$ and conductance $G$ per unit length. . . . .	6
1.2	Coplanar waveguide geometry. . . . .	8
1.3	Voltage and current variations along a half-wavelength and a quarter-wavelength coplanar waveguide resonator. . . . .	10
1.4	Lumped-element circuit model of a resonator, as a parallel RLC circuit, coupled to a feedline via a coupling capacitor $C_c$ . . . . .	10
1.5	Energy spectrum of the bare (in red) and dressed (in blue) states at zero qubit-resonator detuning. . . . .	16
1.6	Vacuum Rabi splitting for a strongly coupled qubit-resonator system.	16
1.7	Representation of a quantum dot. . . . .	18
1.8	Coulomb blockade in a single quantum dot with holes. . . . .	19
1.9	Coulomb diamonds of a single quantum dot. . . . .	20
1.10	Representation of a double quantum dot in series. . . . .	21
1.11	Charge stability diagram of a double quantum dot with holes for different interdot coupling. . . . .	22
1.12	Energy diagram of a single charge in a double quantum dot as a function of the detuning. . . . .	23
1.13	Dispersive and resonant charge-photon coupling. . . . .	24
1.14	Energy diagram of a single charge in a double quantum dot in a finite magnetic field as a function of the detuning with identical $g$ -factors ( $g = 2$ ) and at $B = 200$ mT. . . . .	27
1.15	Schematic model of the spin-photon flopping mode experiment. . .	29
1.16	Strong spin-photon coupling evidenced by the vacuum Rabi splitting.	30
2.1	Hybrid fabrication project between Si nanowire devices from LETI and superconducting resonators from an academic clearroom, PTA.	34
2.2	Comparison of different quantum dot structures in Si. . . . .	35
2.3	Major steps of the Si-MOS transistors fabrication. . . . .	36

LIST OF FIGURES

2.4	Topography of the wafer after silicidation of the transistors. . . . .	37
2.5	Attempts of dummy structures removal. . . . .	38
2.6	Fabrication process of the planarized transistors wafer with electrical contacts in tungsten. . . . .	39
2.7	Target voltage as a function of nitrogen flow. . . . .	40
2.8	DC characterization of the NbN films. . . . .	42
2.9	Upper critical magnetic field of a 10 nm thick NbN film. . . . .	43
2.10	Resonators simulation on Sonnet. . . . .	46
2.11	Images of a die from macroscopic to microscopic. . . . .	47
2.12	Fabrication process of the alignment crosses. . . . .	48
2.13	Fabrication process of the superconducting NbN resonators. . . . .	48
2.14	SEM image of a NbN resonator connected to a two-gate silicon transistor. . . . .	50
2.15	Photographs of the measurement set-up. . . . .	51
2.16	Schematic of the measurement setup for a DQD device with the sample chip bonded on the daughter PCB. . . . .	52
3.1	Experimental implementation for the resonators characterization. . . . .	57
3.2	Normalized transmission spectrum of a resonator. . . . .	57
3.3	Transmission amplitude of a 4.1 k $\Omega$ resonator around its resonance frequency at different output power of the VNA. . . . .	58
3.4	Power dependence of the resonators' internal quality factors. . . . .	59
3.5	Power dependence of the external quality factor for the 4.1 k $\Omega$ resonators. . . . .	60
3.6	Evolution of the resonators characteristics with a magnetic field. . . . .	61
3.7	Resonance of a 4.1 k $\Omega$ resonator in the single photon regime at finite in-plane magnetic field. . . . .	62
3.8	Resonator characterization on a Si-MOS chip. . . . .	64
3.9	Hybrid Si QD-cavity system design in the cQED architecture. . . . .	64
3.10	Colourized SEM image of a LC low-pass filter with a cut-off frequency of 1.2 GHz. . . . .	65
3.11	Quarter-wave transformer at the resonator voltage node point in addition of the LC filter. . . . .	66
3.12	Microwave resonances dependence on the ground plane definition. . . . .	67
4.1	Hybrid device with four-gate nanowire transistor embedded in a high-impedance NbN cavity. . . . .	72
4.2	Transport measurement of all the gates at room temperature. . . . .	73
4.3	Transport measurement of the 4-gates transistor at 8 mK. . . . .	74
4.4	Transmission spectrum of the resonator from 4 GHz to 8 GHz probed with $P_{in} = -90$ dBm. . . . .	75
4.5	Transmission spectrum of the resonator with less than one photon on average. . . . .	75

4.6	Charge stability diagram as a function of $V_{g2}$ and $V_{g3}$ probed by the microwave cavity. . . . .	77
4.7	Charge stability diagram as a function of $V_{g1}$ and $V_{g2}$ probed by the microwave cavity. . . . .	78
4.8	Interdot charge transition with a single hole oscillating in the DQD.	79
4.9	Charge-photon interaction. . . . .	80
4.10	Temperature dependence of the resonance frequency dispersive shift.	81
4.11	Charge-photon coupling strength and lever arm. . . . .	82
5.1	Double quantum dot charge qubit in a Si-MOS device and the charge-photon interaction characteristics. . . . .	86
5.2	Normalized transmission amplitude as a function an in-plane magnetic fields for $\phi = 90^\circ$ . . . . .	87
5.3	Normalized transmission amplitude of the cavity as a function of in-plane magnetic field and the vacuum Rabi splitting. . . . .	88
5.4	Cavity transmission as a function of $B$ and $\varepsilon$ for different magnetic field angles. . . . .	90
5.5	Measurement of the g-factor for the left and right dot using the detuning-magnetic field map for $\phi = 67^\circ$ . . . . .	91
5.6	g-factors of the dots below G1 and G2 as a function of the in-plane magnetic field angle $\phi$ extracted at $\varepsilon = 200 \mu\text{V}$ from the resonance condition with the resonator. . . . .	92
5.7	Spin sweet spot for the spin-photon coupling at $\phi = 101^\circ$ . . . . .	93
5.8	Cavity transmission as a function of $B$ and $f_p$ for different magnetic field angles showing vacuum Rabi splittings. . . . .	94
5.9	Magnetic field angular dependence of the spin-photon interaction. . . . .	95
5.10	Spin-photon interface. . . . .	95
5.11	Energy diagrams of the four spin states different magnetic field angles.	98
5.12	Spin-photon interaction in the single quantum dot limit for $\phi = 11.25^\circ$ . . . . .	99
5.13	Two tone spectroscopy of the spin transition as a function of applied spectroscopy power for $\phi = 101.25^\circ$ . . . . .	101
5.14	Angular dependence of the spin and photon decoherences. . . . .	102
3.1	Two-tone spectroscopy to extract the kinetic inductance of the NbN film. . . . .	118
4.1	Electrical circuit model of a parallel resonator, as a RLC circuit, coupled to a feedline via a coupling capacitor $C_c$ . . . . .	119





# LIST OF TABLES

2.1	Influence of sputtering parameters of bulk (50 nm) NbN on the critical temperature. . . . .	41
2.2	NbN film characterization for different sputtering temperatures. . .	44
3.1	Characteristic impedance of the resonators with different geometries	56
4.1	Device characteristics and dimensions . . . . .	72



# INTRODUCTION

**I**n 1981, Richard Feynman formulated the idea of using quantum computers to simulate quantum systems which are too complex for classical computers [45] and gave birth to the field of quantum computing. The ambition to realize a quantum computer, way more powerful than its classical digital counterpart, inspired many physicists in the 80s, notably Peter Shor. Shor developed in 1994 a quantum algorithm to find prime factors for integers [129], the so-called Shor algorithm. Two years later, Shor also came up with the theory of error correction codes and fault tolerant quantum computations which set the long-term goal of the quantum computing field. The aspiration of a quantum computer is based on its promise of very powerful computational methods. Indeed, it can help to solve problems much faster in drug design, generative chemistry, energy storage and production, cryptography for instance [92, 115].

Experimentally, the building block of a quantum computer, a quantum bit (qubit), can be created from any two-level quantum system. Over the past decades, theoretical and experimental demonstrations of qubits have flourished using for example ion traps, nuclear spins, photons, superconducting circuits or semiconductor quantum dots. Among these different platforms, entangled photons enable the realization of a quantum cryptography system [68] while the first implementation of the Shor algorithm is demonstrated using seven nuclear spins to factorize the number 15 [140]. More recently, in 2019, Google Quantum AI team claimed the quantum supremacy with the Sycamore chip composed of 53 superconducting qubits [8]. In this experiment, the control and read out of each qubit is performed by a superconducting resonator and based on light-matter interactions in a circuit quantum electrodynamics (QED) architecture. It proves therefore the importance of circuit QED for large scale quantum computation. In this thesis, we explore the circuit QED for spins in gate-defined silicon quantum dots, which present long lifetime [137], fault tolerant control fidelity [100, 108, 154] and massive production using classical microelectronics fabrications [139].

## Cavity to circuit quantum electrodynamics

The foundation of circuit QED lays on the cavity QED which explores the coherent interaction between a two-level atom and a photon [60]. In cavity QED, the atom is placed in a cavity which reflects photons inside back and forth many times before they leak out. In this way, the cavity confines photons to a small volume, increasing their energy density and giving them many chances to interact with the atom, and thereby enhancing the effective light-matter interaction strength. When the photon is resonant with the atom, and if the interaction strength is larger than the relaxation time of the photon and the atom, then the strong coupling regime is attained. In this regime, the atom can emit and reabsorb a single photon several times before the atom decays or the photon escapes from the cavity. A periodic oscillation of the photon and atom excitation therefore appears, known as the vacuum Rabi oscillation [60]. This regime is of particular interest as a single energy quantum is shared coherently between the photon and the atom.

Later on, QED experiments were implemented with superconducting circuits as artificial atoms and the circuit QED field emerged from it [18]. Superconducting qubits are anharmonic oscillators based on Josephson junctions which have a non linear inductance [32]. This non-linearity results in a different energy spacing between the ground state to the first excited or to the higher states in the system. Compared to cavity QED, circuit QED devices are much more compact as the cavity is now a coplanar waveguide resonator which can be fabricated on the same chip than the superconducting qubits [17]. The strong coupling regime in circuit QED has also found its interest in the quantum computing field. The coherent photon-qubit interaction can be used as a quantum non-demolition measurement [87] or long-range qubits coupling using virtual photons [89, 76]. In the latter experiment, if a very large photon-coupling rate is achieved, then when two qubits are dispersively coupled to the same cavity, there will be a transverse exchange interaction between both qubits which depends on the coupling strength and the detuning of both qubits with respect to the cavity. As the qubits are detuned from the cavity, no real photons are emitted or absorbed, then it is insensitive to the photon loss of the cavity. These experiments are essential for large-scale quantum information processing and explain the great success of circuit QED in this field.

## Semiconductor spin qubits

Superconducting qubits have proven their great potential notably with the Google 53-qubit chip [8] but also with the 127-qubit processor of IBM [31]. However in the perspective of large-scale quantum computations requiring millions physical qubits [46], semiconductor qubits may appear to be more suitable platforms. Indeed the semiconductor qubits can benefit from a smaller footprint size and a possible mass production by the semiconductor microelectronics industries [139].

The first theoretical proposal of spin qubits in semiconductor quantum dots

(QD) was formulated by Loss and DiVincenzo in 1998 [86]. The spin degree of freedom of a single charge carrier is one of the most fundamental natural two-level system that is insensitive to electric fields noise, leading to long coherence times and it can be isolated and controlled in semiconductor quantum dots within nanometer-scale. Early realizations of spin qubits were demonstrated with on gallium-arsenide (GaAs) heterostructures [111] with very high charge carrier density. However, in GaAs structures there is a nuclear spin bath which magnetic moment fluctuations destroy the dephasing coherence of the spin states. To address this limitation, the spin qubit community began to explore silicon (Si) based devices. The natural isotope of silicon,  $^{28}\text{Si}$ , has zero nuclear spin, providing a clean magnetic environment and therefore Si-based spin qubits have much longer dephasing time, which can be increased even more with isotopically enriched  $^{28}\text{Si}$  [137]. A single spin qubit can achieve a dephasing time  $T_2$  as long as 2 ms [137] and a single qubit control fidelity of 99.9% [155]. Due to the environmental isolation of electronic spin states, the relaxation times  $T_1$  of QD spin qubits are typically very long, ranging from 100 ms to as long as a few seconds [153, 130]. Different implementations of two-qubit gates have been demonstrated as well [143, 150], with fidelities up to 99% [64, 154, 100, 108].

However, due to its degree of environment isolation, spin qubits are typically difficult to address and couple. In addition, the very long coherence times are obtained only for qubits controlled with magnetic fields leading to low Rabi frequencies. To circumvent this limitation, electrical control can be achieved using intrinsic or artificial spin-orbit coupling (SOC) of a material and electric-dipole spin resonance (EDSR) [54, 23]. More recently hole states in silicon and germanium gained a lot of attention as a potential candidate for quantum information technology [125]. The stronger SOC of the valence bands enables fast and all-electric control of the spin state via the EDSR mechanism. Following the first experimental demonstration of a hole spin qubit in silicon [91], a  $2 \times 2$  hole qubit processor in germanium has also been realized [63] paving the way toward the large scale quantum computation.

Parallel to the realization of quantum processors, there is also a need of connectivity between the qubits. Indeed, the Heisenberg exchange interaction, which has enabled the demonstration of two-qubit gates [100, 108, 154] and a six-qubit processor in silicon [112], is limited to an effective distance of about 100 nm. A long-range coupling of spin qubits is then needed to achieve the individual readout of each qubit and the connectivity for quantum error correction. This challenge can be addressed by the integration of spin qubits with circuit QED, as a coplanar waveguide cavity can couple spin qubits over microns to millimeters distances [17].

## Coupling spins to microwave photons

Whereas charges in QDs readily couple to the electric field of a microwave cavity through the electric-dipole interaction [47, 110] resulting in strong charge-

photon coupling [96, 132], a spin only couples to the magnetic field component through magnetic-dipole interaction, which is too weak to allow coherent exchange between a photon and a spin [66, 16]. Therefore, a coherent spin-photon interface needs to rely on the indirect interaction of the spin with the electric field of the cavity through a hybridization between the charge degrees of freedom with the spin degrees of freedom. This coherent spin-photon coupling via spin-charge hybridization has been recently accomplished for electron spins in silicon double quantum dots (DQDs) by introducing transverse magnetic field gradients [124, 95] or by exchange interactions within a double or triple QDs [82]. Working with hole states in the valence band, the spin-charge hybridization mechanism is naturally given by the SOC, offering a priori a stronger coupling strength [136, 74, 106, 104]. It is therefore of fundamental interest to integrate a hole spin qubit with circuit QED elements, which can enable remote spin-spin interactions [15] and single-shot high fidelity dispersive spin readout [39].

## Thesis outline

In this thesis, we explore a novel spin circuit QED architecture with a hole spin qubit in silicon. **Chap. 1** introduces the microwave engineering of coplanar waveguide resonators and the theoretical background of circuit QED applied to hole spin qubits. **Chap. 2** provides the experimental methods of this work, from the fabrication of the silicon devices and their co-integration with the circuit QED elements, to the experimental measurement set-up. **Chap. 3** focuses on the superconducting microwave resonators and their behaviour at zero and finite magnetic fields, we also discuss about the challenges of the integration of the resonators on the silicon qubit chips. With this, we have all the ingredients to define a circuit QED system with hole states, which is explored in **Chap. 4** by studying the hole charge-photon interaction. In **Chap. 5**, we operate at finite magnetic fields to explore the spin-photon interaction and demonstrate the dependence of the interaction strength on the magnetic field orientation as predicted by the Rashba SOC for 1-dimensional devices. Finally we conclude this work and discuss about perspectives to further explore the circuit QED architecture with hole spin qubits.

Chapter **1**

# CIRCUIT QUANTUM ELECTRODYNAMICS WITH SI HOLE SPINS

## Contents

---

<b>1.1 Superconducting coplanar waveguide resonators . . . . .</b>	<b>6</b>
1.1.1 Transmission line model . . . . .	6
1.1.2 Coplanar waveguides . . . . .	7
1.1.3 Half-wavelength CPW resonators . . . . .	9
<b>1.2 Light matter interaction in circuit QED . . . . .</b>	<b>12</b>
1.2.1 Jaynes-Cummings Hamiltonian . . . . .	12
1.2.2 Dressed eigenstates . . . . .	15
1.2.3 Strong coupling regime . . . . .	17
<b>1.3 Circuit QED with a charge qubit . . . . .</b>	<b>17</b>
1.3.1 Quantum dots physics . . . . .	17
1.3.2 Charge-photon coupling via electric-dipole interaction . . . . .	22
<b>1.4 Circuit QED with a hole spin . . . . .</b>	<b>24</b>
1.4.1 Hole spin in a DQD . . . . .	25
1.4.2 Rashba spin-orbit coupling (SOC) . . . . .	28
1.4.3 Spin-photon coupling via intrinsic SOC . . . . .	29

---



In this thesis, we study the light-matter interactions between a single hole spin and a microwave photon as a first step towards long-range interactions of two distant hole spins. In this chapter, we therefore present the microwave engineering of superconducting resonators used



to trap single photons. After we derive the Jaynes-Cummings Hamiltonian describing the light-matter interaction and focus on the strong coupling regime where coherent exchange of energy between light and matter becomes reversible. We then describe the quantum dots physics and how a charge in a double quantum dot can interact with a microwave photon. Finally we present the hole spin flopping mode qubit model, namely a hole spin in a double quantum dot, and the spin-photon interaction enabled by the spin-orbit coupling.

## 1.1 Superconducting coplanar waveguide resonators

A single photon and a single two-level system lay at the heart of circuit QED experiments. In this section, we focus on the cavity in the microwave frequency regime in order to be able to match the spin transition energy. We first introduce the transmission line model and then present the half-wavelength coplanar waveguide resonators used to trap single photons.

### 1.1.1 Transmission line model

The transmission line theory asserts that an infinitesimal length  $\Delta z$  of the transmission line can be modelled as a lumped-element circuit, *i.e.* the voltage and current can be estimated constant over this small length. The lumped-element description of a infinitesimal line is shown in Fig. 1.1 with  $\Delta z \ll \lambda$ , the electric wavelength.

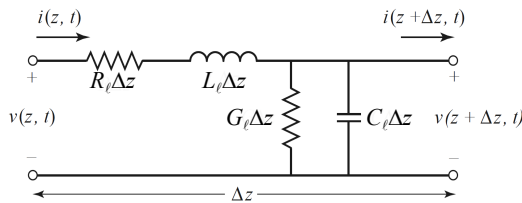


Figure 1.1 – Lumped-element circuit model for an infinitesimal length  $\Delta z$  of a transmission line with the resistance  $R_\ell$ , inductance  $L_\ell$ , capacitance  $C_\ell$  and conductance  $G_\ell$  per unit length.

From the lumped-element model, the circuit can be described by the telegrapher equations [117]

$$\frac{\partial v(z, t)}{\partial z} = -R_\ell i(z, t) - L_\ell \frac{\partial i(z, t)}{\partial t}, \quad (1.1)$$

$$\frac{\partial i(z, t)}{\partial z} = -G_\ell v(z, t) - C_\ell \frac{\partial v(z, t)}{\partial t}, \quad (1.2)$$

with the resistance  $R_\ell$ , inductance  $L_\ell$ , capacitance  $C_\ell$  and conductance  $G_\ell$  per unit length,  $v(z, t)$  the voltage and  $i(z, t)$  the current flowing through the transmission line at position  $z$ .

Assuming that the system is in a sinusoidal steady-state, the equations can then be simplified as

$$V(z) = V^+ e^{-\gamma z} + V^- e^{\gamma z}, \quad (1.3)$$

$$I(z) = I^+ e^{-\gamma z} + I^- e^{\gamma z}, \quad (1.4)$$

where  $\gamma = \alpha + j\beta = \sqrt{(R_\ell + j\omega L_\ell)(G_\ell + j\omega C_\ell)}$  is the complex propagation constant, with  $\alpha$  the attenuation constant and  $\beta$  the phase constant [117].

From Eq. (1.3) and Eq. (1.4), the characteristic impedance of the transmission line can be written as

$$Z_c = \frac{V^+}{I^-} = -\frac{V^-}{I^+} = \sqrt{\frac{R_\ell + j\omega L_\ell}{G_\ell + j\omega C_\ell}}. \quad (1.5)$$

The electric wavelength of the line is defined as

$$\lambda = \frac{2\pi}{\beta}, \quad (1.6)$$

and the phase velocity is given by

$$v_p = \frac{\omega}{\beta}. \quad (1.7)$$

The series resistance  $R_\ell$  represents the resistivity of the individual conductors, which can be neglected for superconducting circuits. The shunt  $G_\ell$  is the dielectric loss in the material between the conductors, which is usually also neglected. Thus we can rewrite the characteristic impedance as

$$Z_c = \sqrt{\frac{L_\ell}{C_\ell}}, \quad (1.8)$$

and the phase velocity as

$$v_p = \frac{1}{\sqrt{L_\ell C_\ell}}. \quad (1.9)$$

## 1.1.2 Coplanar waveguides

In this work, we are interested in coplanar waveguide (CPW) geometry resonators, which have the advantage of an one-step fabrication process. A CPW consists of a center strip line of width  $w$  as the central conductor of the transmission line, which is separated from the ground planes by a gap of width  $s$  as illustrated by Fig. 1.2.(a). The electromagnetic distribution on a cross-section is shown in Fig. 1.2.(b), the electric field is oriented from the central conductor to the ground planes.

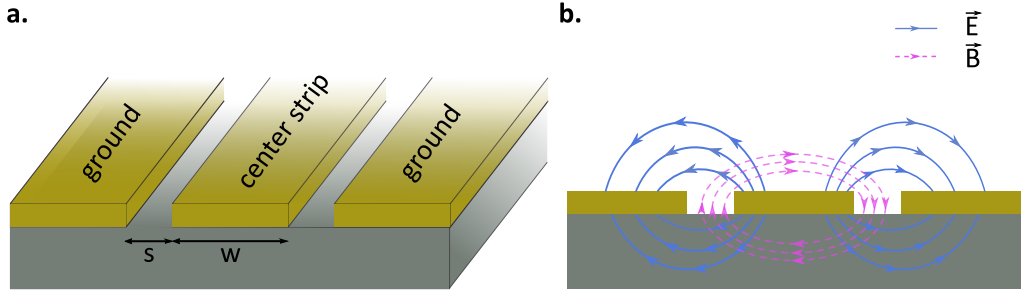


Figure 1.2 – Coplanar waveguide geometry. (a) Coplanar waveguide design with a central strip of width  $w$  and a gap to ground of width  $s$ . (b) Cross section with the electromagnetic field distribution.

The geometric inductance and capacitance per unit length of a coplanar waveguide can be calculated using the conformal transformations [131, 50]:

$$C_\ell = 4\varepsilon_0\varepsilon_{\text{eff}} \frac{K(k_0)}{K(k'_0)}, \quad (1.10)$$

$$L_\ell = \frac{\mu_0}{4} \frac{K(k'_0)}{K(k_0)} \quad (1.11)$$

with  $k_0 = w/(w + 2s)$ ,  $k'_0 = \sqrt{1 - k_0^2}$ ,  $K$  the complete elliptic integral of the first kind,  $\varepsilon_0$  the vacuum permittivity,  $\varepsilon_{\text{eff}}$  the effective permittivity of the substrate and  $\mu_0$  the vacuum permeability. If we consider a substrate of thickness  $h$ , then  $\varepsilon_{\text{eff}}$  can be written as

$$\varepsilon_{\text{eff}} = 1 + \frac{(\varepsilon_r - 1) K(k_1) K(k'_0)}{2 K(k'_1) K(k_0)}, \quad (1.12)$$

with  $\varepsilon_r$  the permittivity of the substrate and  $k_1 = \sinh(\pi w/4h)/\sinh(\pi(w + 2s)/4h)$ .

The characteristic impedance is [131]

$$Z_0 = \frac{1}{c\sqrt{\varepsilon_{\text{eff}}}C_{\text{air}}}, \quad (1.13)$$

where

$$C_{\text{air}} = 4\varepsilon_0 \frac{K(k_0)}{K(k'_0)}. \quad (1.14)$$

Then using the numerical approximations that  $\varepsilon_0 = \frac{1}{36\pi} \cdot 10^{-9}$  F/m and  $c = 3 \cdot 10^8$  m/s, we obtain

$$Z_0 = \frac{30\pi}{\sqrt{\varepsilon_{\text{eff}}}} \frac{K(k'_0)}{K(k_0)} = \sqrt{\frac{L_\ell}{C_\ell}}, \quad (1.15)$$

which is in agreement with the characteristic impedance given by the transmission line model.

As in circuit QED experiments, the coupling between the charge degree of freedom of the hole and a microwave photon depends on the zero point fluctuation (ZPF) voltage of the cavity with  $V_{\text{ZPF}} \propto \sqrt{Z_c}$  [29, 98]. To enhance the charge-photon coupling we can then use a high-impedance resonator. To do so, either we can decrease the capacitance  $C_\ell$  of the line by either reducing the central width of the CPW to a nanowire or increasing the gap width, or we can increase the inductance  $L_\ell$ . Here again, two solutions are possible to increase the inductance. First, we can boost the geometric inductance by reducing the central conductor's width, which is in line with decreasing the capacitance. Second, we can select disordered superconducting films such as NbN [105], NbTiN [123], TiN [83, 128, 4], InOx [9, 41] or granular Al [161, 56], which possess a large kinetic inductance contribution. Indeed, kinetic inductance can be observed in superconductors as the manifestation of the inertial mass of the Cooper pairs and can be estimated from [135]

$$L_{\text{kin}}(H/\square) = \frac{\hbar R_\square}{\pi \Delta_0} \quad (1.16)$$

with  $R_\square$ , in the unit of  $\Omega/\square$ , the sheet resistance,  $\Delta_0$  the superconducting gap and  $\hbar$  the reduced Planck constant.

For a coplanar waveguide where  $s \gg w$ , we can approximate it as a nanowire, then the kinetic inductance per unit length can be approximated as

$$L_\ell^{\text{kin}} = \frac{L_{\text{kin}}(H/\square)}{w}. \quad (1.17)$$

We can then subsequently increase the characteristic impedance when adding a kinetic inductance component.

### 1.1.3 Half-wavelength CPW resonators

We have introduced the coplanar waveguides but so far it does not form a cavity to trap photons. There are two common categories of coplanar waveguide resonators, which are half-wavelength [57] or quarter wavelength [50]. Both geometries have their advantages. A  $\lambda/4$  resonator presents a lower capacitance, which would be an asset to boost the characteristic impedance. However, the voltage distribution of a  $\lambda/2$  resonator has two anti-nodes, which will be important when coupling two distant qubits to the same resonator as the voltage fluctuations are maximal at both ends. In Fig. 1.3 is displayed the voltage and current variations of both geometries.

Once we have decided for the half-wavelength resonators, we still have other decisions to make in terms of design. The open-ended ( $Z_L = +\infty$ ) half-wavelength resonators used in the previous reports of spin-photon coupling in silicon are of two different kinds. The first one is a capacitively coupling to the input and output feedline by a capacitance gap on each end of the resonator [57, 97]. The second one is a capacitively coupling to a  $50\Omega$  transmission line in a hanger geometry [121, 124].

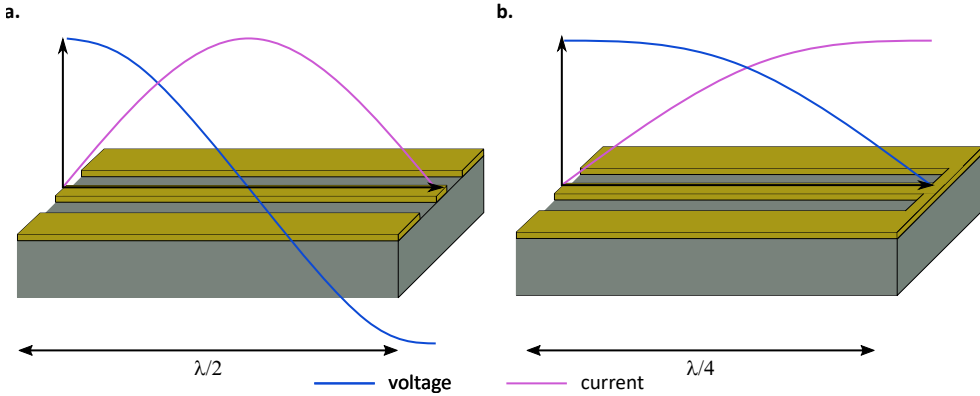


Figure 1.3 – Voltage and current variations along a half-wavelength and a quarter-wavelength coplanar waveguide resonator. (a) Open-ended half-wavelength resonator with two voltage anti-nodes. (b) Short-ended quarter-wavelength resonator with one voltage anti-node.

We have chosen the hanger geometry for our devices with the simple reason that there is the possibility of probing several different resonators connected to different quantum dots with the same input and output RF ports. Hence, the discussion now focuses on a half-wavelength open-ended transmission line resonator coupled capacitively to a  $50\ \Omega$  transmission line read in transmission. The length of the resonator is set as  $\ell = \lambda/2$ . The lumped-element description of such a resonator is shown in Fig. 1.4.

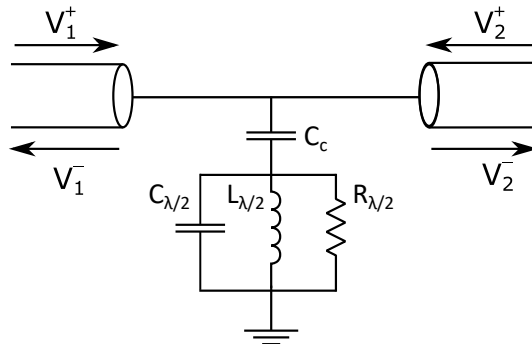


Figure 1.4 – Lumped-element circuit model of a resonator, as a parallel RLC circuit, coupled to a feedline via a coupling capacitor  $C_c$ . The resonator is described by a capacitance  $C_{\lambda/2}$ , an inductance  $L_{\lambda/2}$  and a resistance  $R_{\lambda/2}$ , which can be neglected for a superconducting resonator.

The parameters of the equivalent RLC circuit are given by [117]

$$R_{\lambda/2} = \frac{Z_c}{\alpha \ell}, \quad (1.18)$$

$$C_{\lambda/2} = \frac{\pi}{2\omega_r Z_c}, \quad (1.19)$$

$$L_{\lambda/2} = \frac{1}{\omega_r^2 C_{\lambda/2}}, \quad (1.20)$$

with  $\omega_r$  the resonance frequency of the resonator,  $\ell$  its length,  $\alpha$  its attenuation constant and  $Z_c$  the characteristic impedance.

The resonance frequency is given by

$$f_r = \frac{\omega_r}{2\pi} = \frac{1}{2\pi \sqrt{L_{\lambda/2} C_{\lambda/2}}}. \quad (1.21)$$

Around resonance, we can write  $f_r$  as a function of the capacitance and inductance per unit length, as these values can be extracted by simulation or calculation. Using Eq. (1.8) and  $v_p = \lambda \cdot f_r = 1/\sqrt{L_\ell C_\ell}$ , the equivalent lumped-element can be transformed into a distributed  $\lambda/2$  resonator with

$$C_{\lambda/2} = \frac{\ell}{2} C_\ell, \quad (1.22)$$

$$L_{\lambda/2} = \frac{2\ell}{\pi^2} L_\ell. \quad (1.23)$$

thus the resonance frequency can be written as

$$f_r = \frac{1}{2\ell} \frac{1}{\sqrt{L_\ell C_\ell}}. \quad (1.24)$$

Note that Eq. (1.24) does not consider the coupling capacitance to the feedline  $C_c$ . This is justified only if  $C_{\lambda/2} \gg C_c$ , meaning that the transmission line is long compared to the coupling length. Otherwise, Eq. (1.24) has to be corrected as

$$f_r = \frac{1}{2\pi} \frac{1}{\sqrt{L_{\lambda/2}(C_{\lambda/2} + C_c)}}. \quad (1.25)$$

The resonators performance is quantified by its quality factor which is defined as [117]

$$Q = \omega_r \frac{\text{total energy stored}}{\text{total power dissipated}}. \quad (1.26)$$

$Q$  can be directly measured with the transmission spectrum of the resonator as  $Q = f_r/\Delta f_r$  where  $\Delta f_r$  is the linewidth of the resonance where the signal is attenuated by  $-3$  dB.

When the resonator is coupled to an environment, the losses are split into two categories:

- The internal quality factor  $Q_{\text{int}}$  which is the resistive and dielectric losses. For a superconducting resonator, the resistive loss is negligible and the dielectric loss is commonly referred as the loss tangent  $\tan \delta$ .
- The external quality factor  $Q_{\text{ext}}$  which is the radiative loss, depends on the coupling of the resonator to its environment. This includes the capacitive coupling of the resonator to the feedline, to the quantum dots and all the fanout lines present on the chip.

The total quality factor is then given by

$$\frac{1}{Q} = \frac{1}{Q_{\text{int}}} + \frac{1}{Q_{\text{ext}}}. \quad (1.27)$$

We can also translate the quality factors as a photon loss rate such that  $\kappa/2\pi = f_{\text{r}}/Q$ . We will characterize experimentally in [Sec. 3.2](#) all these loss mechanisms that limit the quality factors of the resonators coupled to quantum dots and try to minimize them.

## 1.2 Light matter interaction in circuit QED

Circuit QED emerged with the extensive research on superconducting circuits [17], it allowed the study and control of quantum interaction at an unprecedented level. Thereafter, the circuit QED has been extended to hybrid systems such as spins, charges, magnons or Rydberg atoms [33]. Here we introduce the formalism of the Jaynes-Cummings model which sheds light on the light-matter interaction. In this section, we consider a simple two-level system, which can be called a qubit, coupled to a superconducting cavity. We derive the Jaynes-Cummings Hamiltonian governing the interaction and then we discuss about the strong coupling regime where coherent exchange happens between the photon and the qubit.

### 1.2.1 Jaynes-Cummings Hamiltonian

The most famous light-matter interaction description is the Jaynes-Cummings model. The model was first developed in 1963 by Edwin Jaynes and Fred Cummings [67] for a quantum mechanical treatment of the interacting system between an atom and a single mode of an electromagnetic field. It can naturally be transposed to our circuit QED system with a single particle in a double quantum dot (DQD) considered as a charge two-level system or charge qubit and a single mode of the microwave cavity.

The Hamiltonian description of such system is given by

$$H = H_0 + H_{\text{field}} + H_{\text{int}}, \quad (1.28)$$

with  $H_0$  the Hamiltonian of the qubit,  $H_{\text{field}}$  the Hamiltonian of the field and the interaction Hamiltonian  $H_{\text{int}}$ .

Before further investigations, we introduce the following operators in the  $\{|L\rangle, |R\rangle\}$  basis of the DQD

$$\tau_- = \begin{pmatrix} 0 & 0 \\ 1 & 0 \end{pmatrix}, \quad (1.29)$$

$$\tau_+ = \begin{pmatrix} 0 & 1 \\ 0 & 0 \end{pmatrix}, \quad (1.30)$$

$$\tau_z = \begin{pmatrix} 1 & 0 \\ 0 & -1 \end{pmatrix}, \quad (1.31)$$

where  $\tau_-$  ( $\tau_+$ ) is the operator that moves the particle from left (right) to right (left) and  $\tau_z$  the Pauli matrix associated to the charge qubit subspace.

The different components of the Hamiltonian are

$$H_{field} = \hbar\omega_r a^\dagger a, \quad (1.32)$$

$$H_{\text{DQD}} = \begin{pmatrix} \varepsilon/2 & t_c \\ t_c & -\varepsilon/2 \end{pmatrix}, \quad (1.33)$$

$$H_{int} = \begin{pmatrix} g_c(a + a^\dagger) & 0 \\ 0 & -g_c(a + a^\dagger) \end{pmatrix} = g_c(a + a^\dagger)\tau_z, \quad (1.34)$$

where  $a$  and  $a^\dagger$  are the annihilation and creation operators of the electromagnetic field mode at  $\omega_r$  inside the resonator,  $\varepsilon$  is the detuning between the two dots and  $t_c$  is the tunnelling rate, and  $g_c = E_0 d_{01}$  the charge-cavity coupling rate with  $d_{01}$  the dipole moment associated to the transition from the ground to the excited state and  $E_0$  the ZPF of the cavity. In the circuit QED architecture, the resonator is connected to one dot. The ZPF of the cavity will then induce a detuning fluctuation of the DQD by  $g_c(a + a^\dagger)$ , which affects on  $\tau_z$ .

One can write the total Hamiltonian in the eigenbasis of  $H_{\text{DQD}}$ . The eigenenergies of  $H_{\text{DQD}}$  are

$$E_\pm = \pm \sqrt{t_c^2 + \left(\frac{\varepsilon}{2}\right)^2} = \pm \frac{1}{2} \sqrt{4t_c^2 + \varepsilon^2} = \pm \frac{\Omega}{2}. \quad (1.35)$$

One can deduce normalized eigenvectors associated with  $E_\pm$

$$\lambda_+ = \begin{pmatrix} \frac{\varepsilon + \Omega}{\sqrt{(\varepsilon + \Omega)^2 + 4t_c^2}} \\ \frac{2t_c}{\sqrt{(\varepsilon + \Omega)^2 + 4t_c^2}} \end{pmatrix},$$

$$\lambda_- = \begin{pmatrix} \frac{\varepsilon - \Omega}{\sqrt{(\varepsilon - \Omega)^2 + 4t_c^2}} \\ \frac{2t_c}{\sqrt{(\varepsilon - \Omega)^2 + 4t_c^2}} \end{pmatrix}.$$



We can rewrite the Hamiltonians in the new eigenstates basis.  $H_{\text{DQD}} = \frac{\Omega}{2}\tau_z$  and  $H_{\text{field}}$  remain unmodified. The interaction Hamiltonian becomes

$$H_{\text{int}} = g_c(a + a^\dagger) \begin{pmatrix} \frac{\varepsilon}{\Omega} & \frac{2t_c}{\Omega} \\ \frac{2t_c}{\Omega} & -\frac{\varepsilon}{\Omega} \end{pmatrix}. \quad (1.36)$$

Thus,

$$H_{\text{int}} = g_c(a + a^\dagger) \left[ \frac{\varepsilon}{\Omega}\sigma_z + \frac{2t_c}{\Omega}(\tau_+ + \tau_-) \right] \quad (1.37)$$

is the interaction term of the quantized field with the two-level system. Be careful that now  $\tau_-$  and  $\tau_+$  are different from Eq. (1.29) and Eq. (1.30) due to the basis change. This interaction term has first been introduced by Isidor Rabi [118], which becomes the Rabi model with the following Hamiltonian

$$H_{\text{Rabi}} = \frac{\Omega}{2}\tau_z + \hbar\omega_r a^\dagger a + g_c(a + a^\dagger) \left[ \frac{\varepsilon}{\Omega}\tau_z + \frac{2t_c}{\Omega}(\tau_+ + \tau_-) \right]. \quad (1.38)$$

In most of systems we can neglect the counter-rotating terms and transform the Rabi Hamiltonian into the Jaynes-Cummings Hamiltonian. To derive the Jaynes-Cummings Hamiltonian, we have to change the dynamical representation of the system. Indeed, there are three different dynamical representations of the quantum mechanics [34], known as the Schrödinger, Heisenberg and Dirac pictures. Up to now, we are in the Schrödinger's picture of quantum mechanics representation where the time-dependence is on the wave-vectors. To apply the counter-rotating wave approximation of Jaynes-Cummings model we switch to the Heisenberg representation. We then attribute the time-dependence to the field operators, while the state vectors become time-independent. Then, we introduce the following operators

$$\begin{aligned} \hat{a} &= a e^{-i\omega_r t}, \\ \hat{a}^\dagger &= a^\dagger e^{i\omega_r t}, \\ \hat{\tau}_z &= \tau_z, \\ \hat{\tau}_- &= \tau_- e^{-i\Omega t/\hbar}, \\ \hat{\tau}_+ &= \tau_+ e^{i\Omega t/\hbar}. \end{aligned}$$

The interaction Hamiltonian can be rewritten as

$$H_{\text{int}} = g_c(a e^{-i\omega_r t} + a^\dagger e^{i\omega_r t}) \left[ \frac{\varepsilon}{\Omega}\tau_z + \frac{2t_c}{\Omega}(\tau_+ e^{i\Omega t/\hbar} + \tau_- e^{-i\Omega t/\hbar}) \right]. \quad (1.39)$$

Using the rotating wave approximation (RWA) by neglecting the fast oscillating terms, Eq. (1.39) becomes

$$H_{\text{int}} = g_c \frac{2t_c}{\Omega} (a \tau_+ e^{i(\Omega - \omega_r)t} + a^\dagger \tau_- e^{i(\omega_r - \Omega)t}). \quad (1.40)$$

One last transformation to get rid of the time-dependency of the operators and go back to the Schrödinger picture

$$H_{int} = \tilde{g}_c(a\tau_+ + a^\dagger\tau_-), \quad (1.41)$$

with  $\tilde{g}_c = 2g_c t_c / \Omega$ .

Finally the famous Jaynes-Cummings Hamiltonian is given by

$$H_{\text{JC}} = \frac{\Omega}{2}\tau_z + \tilde{g}_c(a\tau_+ + a^\dagger\tau_-) + \hbar\omega_r a^\dagger a. \quad (1.42)$$

The Jaynes-Cummings Hamiltonian is derived in the framework of the RWA. However, if the coupling strength is comparable with the cavity or qubit energies, then this approximation is not valid and the system has to be modelled by the Rabi Hamiltonian [48].

### 1.2.2 Dressed eigenstates

The dressed state, *i.e.* the hybrid state between the single photon and the qubit, of the Jaynes-Cummings Hamiltonian (under RWA) is given by the Bogoliubov-like unitary transformation [19]

$$U = \exp[\Lambda(N_T)(a^\dagger\tau_- - a\tau_+)], \quad (1.43)$$

with

$$\Lambda(N_T) = \frac{\arctan(2\lambda\sqrt{N_T})}{2\sqrt{N_T}}, \quad (1.44)$$

$N_T = a^\dagger a + \tau_+ \tau_-$  is the operator associated with the total number of excitations and  $\lambda = g/\Delta$ , with  $\Delta = \omega_q - \omega_r$  the qubit-resonator detuning.

Under this transformation, Eq. (1.42) becomes

$$\begin{aligned} H_{\text{dressed}} &= U^\dagger H U \\ &= \hbar\omega_r a^\dagger a + \frac{\hbar\omega_q}{2}\tau_z - \frac{\hbar\Delta}{2}(1 - \sqrt{1 + 4\lambda^2 N_T})\tau_z. \end{aligned} \quad (1.45)$$

From Eq. (1.45), the energy of the dressed states  $|g, n\rangle$  and  $|e, n-1\rangle$  can be written as

$$E_{g,n} = \hbar m\omega_r - \frac{\hbar}{2}\sqrt{\Delta^2 + 4g^2 n}, \quad (1.46)$$

$$E_{e,n-1} = \hbar n\omega_r + \frac{\hbar}{2}\sqrt{\Delta^2 + 4g^2 n} \quad (1.47)$$

If the energy of the photon matches the energy of the qubit state ( $\Delta = 0$ ), then we can reach a hybridized state, then the two dressed states energies are split by  $2g\sqrt{n}$ , with  $n$  the number of photons. The energy spectrum is depicted in Fig. 1.5 with the bare and dressed states representation.

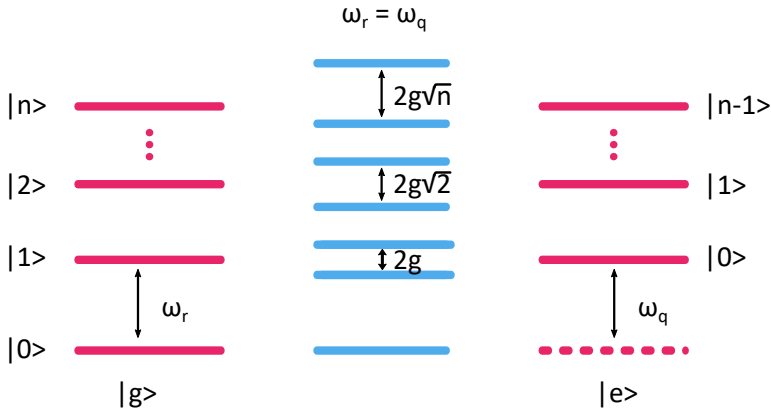


Figure 1.5 – Energy spectrum of the bare (in red) and dressed (in blue) states at zero qubit-resonator detuning. The qubit states are labelled as  $|g\rangle$  and  $|e\rangle$  while the number of photon is labelled as  $|n\rangle$  with  $n \in \mathbb{N}$ . The dressed states are split by  $2g\sqrt{n}$ .

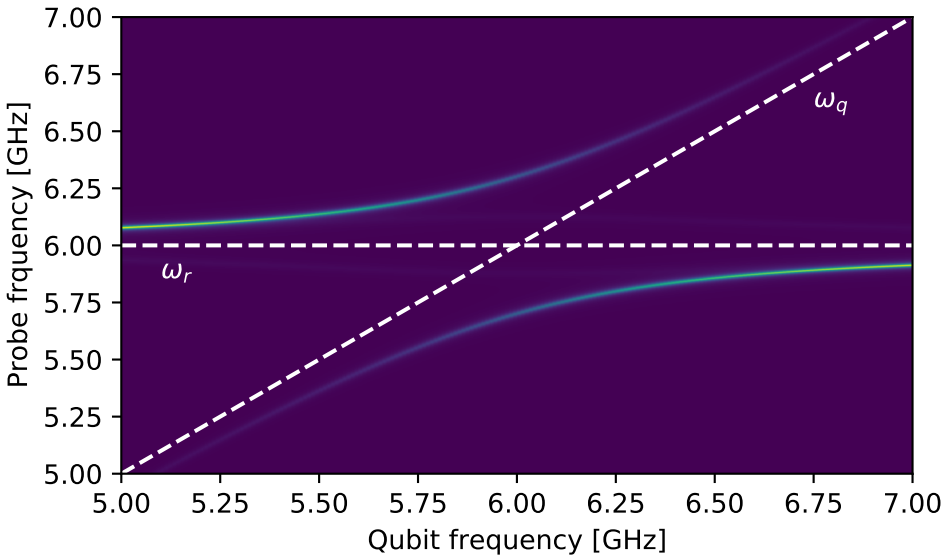


Figure 1.6 – Vacuum Rabi splitting for a strongly coupled qubit-resonator system. The bare energies of the qubit and the resonator are showed in dashed lines. The dressed states are spectroscopically resolved are split by the quantity of  $2g$ . The simulation is made using the quantum toolbox QuTip [69].

### 1.2.3 Strong coupling regime

The strong coupling is of particular interest as quantum information can be coherently exchanged between the qubit and the photon before being lost by decoherence processes. We then define the loss of the interacting system as  $\kappa$  the photon loss rate of the cavity and  $\gamma$  the qubit decoherence rate. The strong coupling,  $g > \kappa, \gamma$ , can then be observed under two conditions [17]:

- the splitting between the two dressed states  $2g$  is larger than  $\kappa/2 + \gamma$ , which is the linewidth of the dressed states
- the dressed states have to be resolved spectroscopically

When these two conditions are fulfilled, we can observe a doublet of peaks at  $\omega_r \pm g$  which is called the vacuum Rabi splitting. This is the hallmark of the strong coupling regime. Fig. 1.6 shows the simulation of such a vacuum Rabi splitting. Such a 2D map can be measured by probing the microwave transmission and analysed using the input-output theory which is derived in Appendix A.

## 1.3 Circuit QED with a charge qubit

The Jaynes-Cummings Hamiltonian derived in the previous section can be implemented with a single photon and a hole in a DQD which behaves as a charge qubit. In this section, we briefly describe the physics of a DQD, for a more extensive review readers can refer to [138, 59], and how a charge qubit can be coupled to a photonic mode of the superconducting resonator.

### 1.3.1 Quantum dots physics

#### Single quantum dot

A quantum dot (QD) can be seen as an island where electrons or holes can tunnel in. The dot is tunnel coupled to Fermi reservoirs, so-called source and drain, which are filled with either electrons or holes. To tune the electrostatic potential of the dot with respect to the reservoirs, the QD is capacitively coupled to one or more gate electrodes. A schematic picture of a quantum dot with one gate electrode is represented in Fig. 1.7.(a). The formalism presented in this chapter is equivalent for electrons or holes.

The quantum dot physics is dominated by two phenomena [59]:

- due to Coulomb repulsion between electrons, adding an electron in the dot costs a charging energy  $E_C$  such that the current-voltage relation of the dot is no longer a Ohm's law due to Coulomb blockade [79].
- the 3D confinement of the hole/electron in the dot leads to a discrete energy spectrum of the hole/electron bound states.

The charging of the quantum dot can be described by the constant interaction model [78] with two assumptions. The first one assumes that the coupling between

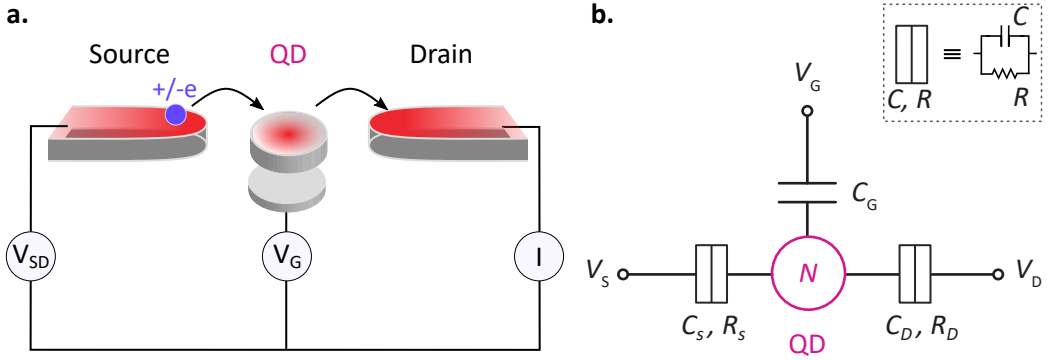


Figure 1.7 – Representation of a quantum dot. (a) Schematic picture of a quantum dot coupled to the reservoirs with electrons or holes. The source is biased with the voltage  $V_{SD}$ , the gate is biased by a voltage  $V_G$  and the current  $I$  is measured through the dot. (b) Constant interaction model of the quantum dot, with  $N$  charges, tunnel coupled to the source, drain and capacitively coupled to the gate electrode. The tunnel barrier is equivalent to a capacitance parallel to a resistance.

the dot and the gates or reservoirs are modelled by a constant capacitance (see Fig. 1.7.(b)). The total capacitance  $C$  is the sum of the capacitances from the gate  $C_G$ , the source  $C_S$  and the drain  $C_D$ :  $C = C_G + C_S + C_D$ . The tunnel barrier can be modelled as a capacitance in parallel with a resistance. The second assumption is that the single particle energy level spectrum is independent of the number of electrons. Under these assumptions, the total energy a dot filled with  $N$  electrons  $U(N)$  is given by

$$U(N) = \frac{[-e(N - N_0) + C_S V_S + C_D V_D + C_G V_G]^2}{2C} + \sum_{n=1}^N E_n(B), \quad (1.48)$$

with  $e$  the elementary charge,  $N_0 e$  is the charge in the dot compensating the background charge originating from impurities in the structure,  $B$  the applied magnetic field, and  $E_n(B)$  is the energy of an occupied level.

The electrochemical potential  $\mu(N)$  is defined as

$$\mu(N) \equiv U(N) - U(N - 1). \quad (1.49)$$

If the electrochemical potential of the dot is alignment with the one of the reservoirs then particles can tunnel in or out of the dot. The bias voltage  $V_{SD} = V_S - V_D$  defines a bias window between the reservoirs such that  $\mu_S - \mu_D = -eV_{SD}$ . If the electrochemical potential of the dot lies within this window, then a particle can tunnel from one reservoir to the dot and to an empty state of the other reservoir.

There are two possible configurations of the bias window: the low-bias regime and the high-bias regime. At low-bias voltage, transport is only possible when the energy level of the dot is in the bias window. If not, the number of particles in

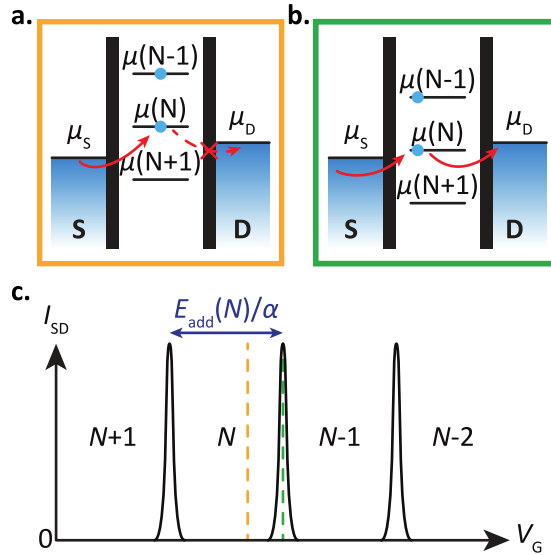


Figure 1.8 – Coulomb blockade in a single quantum dot with holes. (a) The electrochemical potential level diagram in the Coulomb blockade regime. All the levels are outside the bias window, then there is no hole tunnelling event and the number of holes in the dot is fixed. (b) The level  $\mu(N)$  lies in the bias window then a single particle can tunnel through the dot. (c) The current  $I_{SD}$  through the dot as a function of the gate voltage showing Coulomb peaks related to single hole tunnelling events. The peaks separation is directly proportional to the addition energy  $E_{add}$ , which can be related to the gate voltage by the lever arm  $\alpha$ . The gate voltages where (a) and (b) occur are indicated. (Schematic from [43])

the dot remains unchanged and no current flows across the dot. This is called the Coulomb blockade regime. The Coulomb blockade can be lifted by changing the gate voltage, this tunes the electrochemical potential of the dot and can enable single-particle tunnelling. Fig. 1.8 shows the Coulomb peaks measured in current as a function of gate voltage. The distance between two peaks is proportional to the addition energy

$$E_{\text{add}} = \mu(N+1) - \mu(N) = E_C + \Delta E, \quad (1.50)$$

with  $E_C$  the charging energy and  $\Delta E$  the energy spacing between two levels. The proportionality between the energy and the applied gate voltage is given by the lever arm  $\alpha$ , also called the lever-arm coefficient as depicted in Fig. 1.8.(c). In the following, we assume that the temperature is negligible compared to the energy-level spacing  $k_B T \ll E_{\text{add}}$ , such that only one state of the dot can contribute to current.

At high-bias voltage, multiple dot levels can participate in the tunnelling process. When the bias voltage is highly increased, excited states also falls in the bias window and two paths become possible for the particles to tunnel through the dot: the ground or the excited state. If we sweep the gate voltage across multiple charge transitions and for positive and negative bias voltage, then the Coulomb blockade regions appear as diamonds, as shown in Fig. 1.9. These patterns are called Coulomb diamonds.

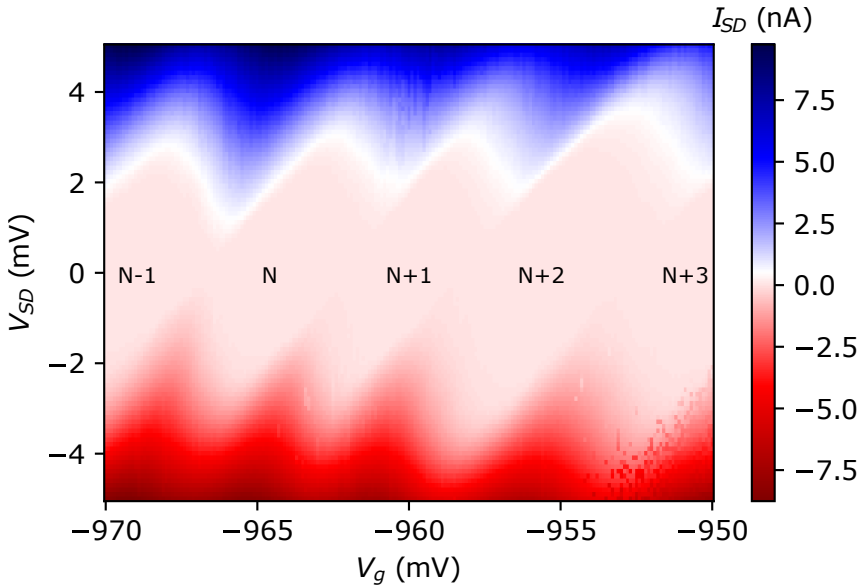


Figure 1.9 – Coulomb diamonds of a single quantum dot with  $N$  charges in the Coulomb blockade region.

## Double quantum dot

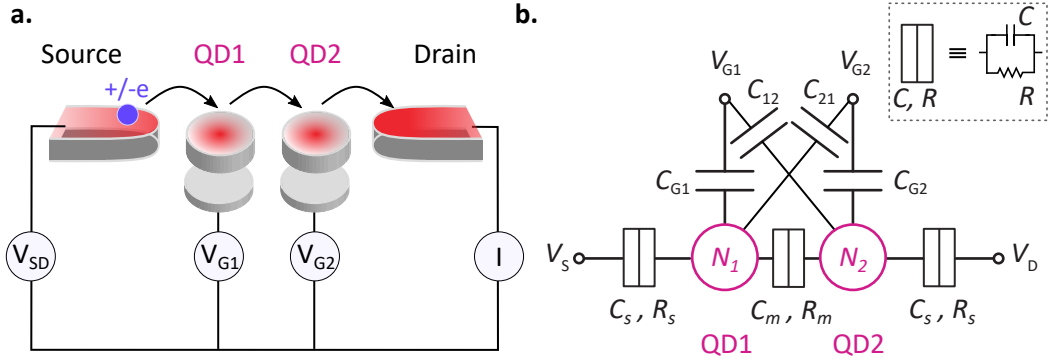


Figure 1.10 – Representation of a double quantum dot in series. (a) Schematic picture of a double quantum dot coupled to reservoirs. The source is biased with the voltage  $V_{SD}$ , the gate 1(2) is biased by a voltage  $V_{G1}(V_{G2})$  and the current  $I$  is measured through the dots. (b) Constant interaction model for a double quantum dot, with  $N_1(N_2)$  particles in the dot 1(2). The dots are tunnel coupled to the reservoirs and capacitively coupled to the gate electrodes. The coupling between the dot is also governed by a tunnel barrier.

Now we consider a DQD as represented in Fig. 1.10. The dots are controlled by two distinct gate voltages,  $V_{g1}$  and  $V_{g2}$ , the gate electrode associated to dot 1 (2) is also capacitively connected to dot 2 (1) such that there is a cross-capacitance. The coupling between the two dots is given by a tunnel barrier characterized by a capacitance  $C_m$  and a resistance  $R_m$ . Fig. 1.11 shows the number of holes ( $N_1, N_2$ ) in the dot 1 and 2 as a function of  $V_{g1}$  and  $V_{g2}$  for different interdot coupling. Such a plot is called the charge stability diagram.

Fig. 1.11.(a) shows the stability diagram of an uncoupled double dot,  $C_{12,21} = 0$ . The vertical and horizontal lines correspond to the dot to lead transitions at a given gate voltage value. These lines correspond to values of the gate voltages at which a hole tunnels from the reservoir to the dot, hence the number of holes in the dot grows as the gate voltage decreases. Since there is no coupling between the two dots, the lines are exactly vertical and horizontal as each gate electrode only affects its corresponding dot.

When the dots are capacitively coupled, see Fig. 1.11.(b), the shape of the diagram changes into a hexagonal honeycomb lattice. Indeed, addition of a hole in one dot will affect the electrostatic energy of the other dot meaning that the gate voltage  $V_{g1}(V_{g2})$  has a capacitive coupling on the dot 2(1). Hence the dot-lead transitions (in blue) have a finite slope now. The lines in magenta correspond to interdot charge transitions. There, the total number of holes in the DQD is kept constant while one hole moves from one dot to another. The length of the interdot charge transition is tuned by the interdot capacitance  $C_m$ . Now the electrochemical



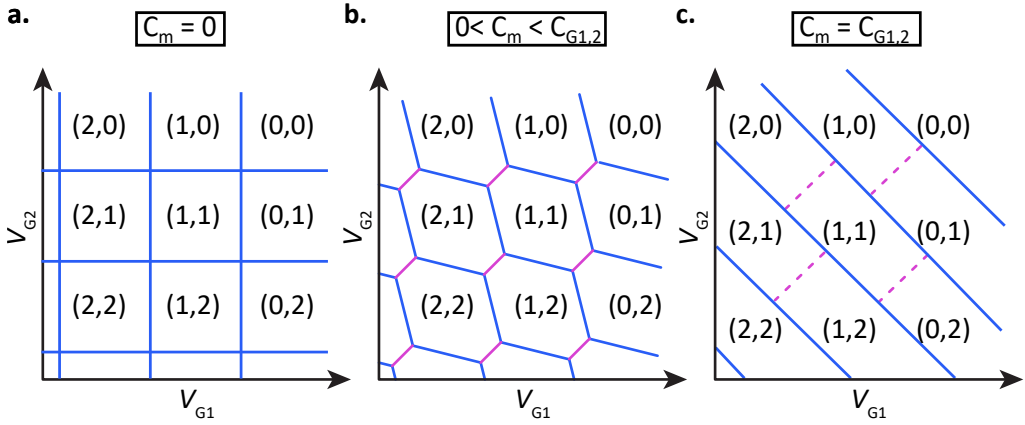


Figure 1.11 – Charge stability diagram of a double quantum dot with holes for different interdot coupling. (a) Uncoupled double quantum dots. (b) Intermediate coupled DQD with the dot-lead transition in blue and interdot charge transition in magenta. (c) Single dot limit for a very large cross-capacitance with the dot-lead transitions oriented at  $45^\circ$ .

potential of dot 1 is given by [59]

$$\begin{aligned}
 \mu_1(N_1, N_2) &\equiv U(N_1, N_2) - (N_1 - 1, N_2) \\
 &= \left(N_1 - \frac{1}{2}\right) E_{C1} + N_2 E_{Cm} \\
 &\quad - \frac{E_{C1}}{|e|} (C_S V_S + C_{G1} V_{G1} + C_{12} V_{G2}) \\
 &\quad + \frac{E_{Cm}}{|e|} (C_D V_D + C_{G2} V_{G2} + C_{21} V_{G1}),
 \end{aligned} \tag{1.51}$$

where  $C_{ij}$  is the cross-capacitance of the gate  $j$  on the dot  $i$ ,  $C_{Gi}$  is the capacitance of the gate  $i$  on the dot  $i$  and  $E_{Ci}$  is the charging energy of the dot  $i$ . All the variables are defined in Fig. 1.10.(b). Similarly, the electrochemical potential of dot 2 can be obtained by interchanging 1 with 2 and  $C_D V_D$  with  $C_S V_S$ .

Fig. 1.11.(c) shows the limit when  $C_{12,21} \gg C_{G1,2}$ . In this case, the transitions to reservoirs merge into a single line and the distance between triple points is maximal. The double dot behaves like a single dot and the dot-lead transitions are oriented at  $45^\circ$ .

### 1.3.2 Charge-photon coupling via electric-dipole interaction

#### A charge qubit

Now we consider a single charge in a DQD. We denote  $|L\rangle$  ( $|R\rangle$ ) the left (right) dot. Then in the  $(|L\rangle, |R\rangle)$  basis, the eigenstates are

$$E_{|+\rangle/|-\rangle} = \pm \frac{1}{2} \sqrt{4t_c^2 + \varepsilon^2}, \tag{1.52}$$

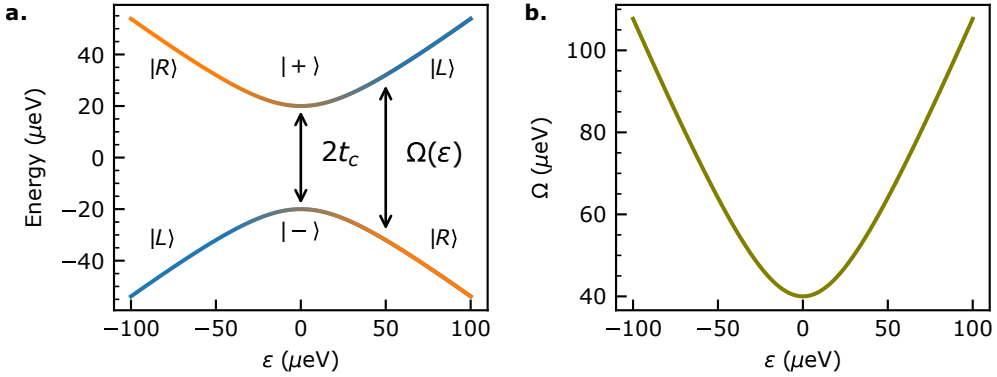


Figure 1.12 – Energy diagram of a single charge in a double quantum dot as a function of the detuning. The left (right) charge state is plotted in blue (orange). At zero detuning, the two charge states are hybridized and the energy levels are separated by  $2t_c$  with  $t_c$  the tunnelling coupling between the two dots.

with  $\varepsilon$  the detuning between the two dots and  $t_c$  the tunnelling rate. Fig. 1.12.(a) depicts the energy of a single charge in a DQD as a function of the detuning energy between the two dots. The energy diagram features a bonding  $|-\rangle$  and an antibonding  $|+\rangle$  state defining a charge qubit of energy splitting  $\Omega(\varepsilon) = \sqrt{4t_c^2 + \varepsilon^2}$ , see Fig. 1.12.(b).

At zero detuning,  $\varepsilon = 0$  eV, the particle is delocalized between the two dots. It also corresponds to the charge sweet spot, with  $\partial\Omega/\partial\varepsilon = 0$ , since in this case small variation of detuning  $\varepsilon$  will barely affect the qubit energy.

### Electric-dipole interaction

The charge degree of freedom of a single hole readily couples to a photonic mode thanks to the electric-dipole interaction [54]. At  $\varepsilon = 0$ , the dipole moment of a single hole in the DQD is increased as the hole is delocalised between the two QDs [47, 110]. The coupling strength of a single photonic mode to the electric dipole of the charge qubit is given by [40]

$$g_c = \frac{1}{2}|e|\alpha V_{\text{ZPF}}, \quad (1.53)$$

with  $e$  the elementary charge,  $\alpha$  the lever-arm to detuning of the gate which is connected to the cavity and  $V_{\text{ZPF}}$  the zero-point fluctuation (ZPF) of the cavity with  $V_{\text{ZPF}} = \omega_r \sqrt{\frac{\hbar Z_c}{\pi}}$  [29, 98], where  $Z_c$  is the impedance of the cavity and  $\omega_r$  its resonance frequency. The charge-photon coupling is therefore device geometry dependent which can be modulated only with a tunable resonance frequency of the cavity as in [132].

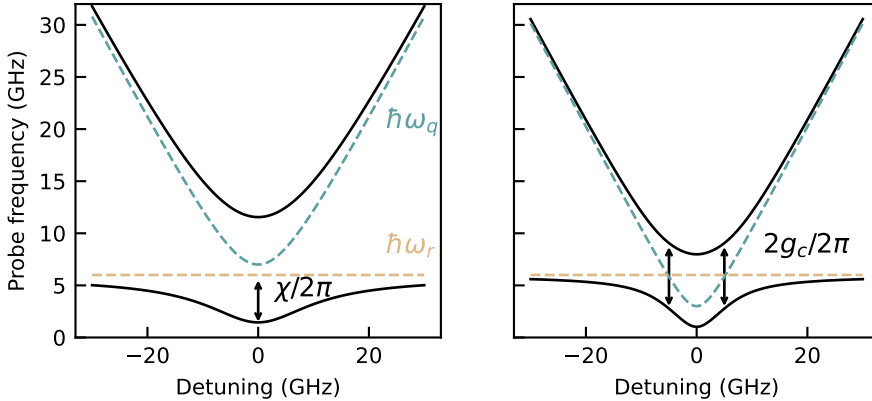


Figure 1.13 – Dispersive and resonant charge-photon coupling. (a) Dispersive charge-photon coupling for  $\hbar\omega_q > \hbar\omega_r$ : the cavity (charge qubit) energy is downshifted (upshifted) by the quantity  $\chi = g_c^2/(\omega_q - \omega_r)$  (valid in the rotating wave approximation). (b) Resonant charge-photon coupling for  $\hbar\omega_q < \hbar\omega_r$ : when the photon is resonant with the charge qubit, there is an avoided crossing split by  $2g_c/2\pi$ .

To achieve the strong coupling regime,  $g_c$  has to be greater than the photon loss  $\kappa$  of the cavity and  $\gamma_c$  the decoherence rate of the charge qubit. This regime has been attained with electrons in silicon QDs in [96, 132]. Experimentally, the charge-photon coherent interaction is illustrated in Fig. 1.13 for  $\hbar\omega_q > \hbar\omega_r$  and  $\hbar\omega_q < \hbar\omega_r$ , with  $\omega_q$  the charge qubit energy. When  $\hbar\omega_q > \hbar\omega_r$  and  $g_c \gg \kappa, \gamma_c$ , then the photon energy in the cavity will downshift by  $\chi/2\pi$  as a consequence of the charge-photon interaction, while the qubit energy will up shift also by  $\chi/2\pi$ . The quantity  $\chi$  is called the dispersive shift. When  $\hbar\omega_q < \hbar\omega_r$ , then at the resonance energy  $\hbar\omega_q = \hbar\omega_r$ , an avoided crossing occurs and the separation between the two states is  $2g_c/2\pi$ . Both situations highlight a charge-photon interaction.

## 1.4 Circuit QED with a hole spin

Compared to the charge qubit, the spin of a single carrier appears to be an even more promising candidate due to its large coherence time [137] and its insensitivity to electrical noise [114]. However, compared to the charge degree of freedom of a single hole or electron, the spin degree of freedom is not a natural candidate for circuit QED experiments as it only has a small magnetic moment, which does not couple naturally and efficiently to photons. In this section, we first describe the theory of a DQD when the spin degeneracy is lifted and introduce the mechanisms which allow spin-photon couplings.

### 1.4.1 Hole spin in a DQD

In the previous section, we were focusing on spinless particles. Here we discuss the spin physics in a DQD. Two configurations are possible, either there is an even number of particles in the DQD or an odd one. In this thesis we only focus on the odd configuration. Compared with electrons, holes have some specificity such as an anisotropic gyromagnetic matrix (g-matrix) [147, 38, 85, 114] and spin-orbit coupling (SOC) [88, 152]. The SOC is a relativistic effect that couples the spin of the hole to its motion and it is our key ingredient to couple the spin to a photon.

We consider the same charge qubit with a single hole in a DQD described in Sec. 1.3.2. At zero magnetic field, the two spin states are degenerated. At finite magnetic field, the spin up  $|\uparrow\rangle$  and the spin down  $|\downarrow\rangle$  are split by the Zeeman energy  $E_Z$  with four possible spin states:  $|L, \downarrow\rangle$ ,  $|L, \uparrow\rangle$ ,  $|R, \downarrow\rangle$  and  $|R, \uparrow\rangle$ . We also introduce the Pauli operators for the spin  $\sigma = (\sigma_x, \sigma_y, \sigma_z)$  and dot basis  $\tau$  with  $\tau_x = |R\rangle\langle L| + |L\rangle\langle R|$ ,  $\tau_y = i(|R\rangle\langle L| - |L\rangle\langle R|)$  and  $\tau_z = |L\rangle\langle L| - |R\rangle\langle R|$ .

First, we can write the detuning contribution as

$$\begin{aligned}\mathcal{H}_\varepsilon &= \frac{\varepsilon}{2}\tau_z, \\ &= \frac{\varepsilon}{2}(|L, \downarrow\rangle\langle L, \downarrow| + |L, \uparrow\rangle\langle L, \uparrow| - |R, \downarrow\rangle\langle R, \downarrow| - |R, \uparrow\rangle\langle R, \uparrow|).\end{aligned}\tag{1.54}$$

The second mechanism comes into play is the Zeeman splitting of the spin states due to an external magnetic field  $B$

$$\begin{aligned}\mathcal{H}_Z &= \frac{1}{2}\mu_B g_{L/R} \cdot B \cdot \sigma, \\ &= \frac{1}{2}g_L\mu_B B(|L, \uparrow\rangle\langle L, \uparrow| + |L, \downarrow\rangle\langle L, \downarrow|) \\ &\quad + \frac{1}{2}g_R\mu_B B(|R, \uparrow\rangle\langle R, \uparrow| + |R, \downarrow\rangle\langle R, \downarrow|),\end{aligned}\tag{1.55}$$

with  $g_L/g_R$  the g-matrix of the left/right dot,  $\mu_B$  the Bohr magneton and  $B$  the static external magnetic field. The g-matrices have  $3 \times 3$  components and generalize the isotropic gyromagnetic response of an electron spin ( $g \sim 2 \times \mathbb{1}_{3 \times 3}$ ) to the anisotropic response of hole spins. The gyromagnetic response of the hole results of the interplay between the confinement of the hole, the SOC and the magnetic field [144, 38, 114]. The confinement shapes an anisotropic hole wave function down to the atomic scale. The SOC mixes the orbitals of the silicon atoms with the spin of the hole, as the valence band wave functions are a mixture of heavy hole and light hole components, it results in anisotropic hole properties. Last, the magnetic field acts on the spin and orbital degrees of freedom of the hole.

The detuning and the Zeeman Hamiltonians characterize each dot individually. We have to model the tunnelling event of the hole spin from one dot to the other. To do so we separate two situations, the hole spin can keep the same spin state or flip after tunnelling in the DQD. We can then introduce the spin conserving Hamiltonian and the spin flip one at a given external magnetic field

$$\begin{aligned}\mathcal{H}_{\text{sc}} &= t_{\text{sc}}\tau_x, \\ &= t_{\text{sc}}(|L, \uparrow\rangle \langle R, \uparrow| + |R, \uparrow\rangle \langle L, \uparrow| + |L, \downarrow\rangle \langle R, \downarrow| + |R, \downarrow\rangle \langle L, \downarrow|),\end{aligned}\quad (1.56)$$

and

$$\begin{aligned}\mathcal{H}_{\text{sf}} &= t_{\text{sf}}\tau_y\sigma_y, \\ &= t_{\text{sf}}(|L, \uparrow\rangle \langle R, \downarrow| - |L, \downarrow\rangle \langle R, \uparrow| - |R, \uparrow\rangle \langle L, \downarrow| + |R, \downarrow\rangle \langle L, \uparrow|),\end{aligned}\quad (1.57)$$

with  $t_{\text{sc}}/t_{\text{sf}}$  the spin conserving/flip tunnelling coupling. Note that Eq. (1.56) and Eq. (1.57) are only valid for a given magnetic field and the Zeeman states  $|\uparrow\rangle$  and  $|\downarrow\rangle$  in the left and right dot are the eigenstates of the uncoupled dots. For dots with similar g-matrices, the tunnelling physics is governed by the Rashba spin-orbit interaction that we present in Sec. 1.4.2.

The total Hamiltonian of the hole spin in the DQD is then

$$\mathcal{H} = \mathcal{H}_{\text{sc}} + \mathcal{H}_{\text{sf}} + \mathcal{H}_Z + \mathcal{H}_\varepsilon, \quad (1.58)$$

which can be expressed in the the orbital ground state basis  $\{|L, \uparrow\rangle, |L, \downarrow\rangle, |R, \uparrow\rangle, |R, \downarrow\rangle\}$  as

$$\mathcal{H} = \begin{pmatrix} \frac{\varepsilon}{2} - \frac{1}{2}g_L\mu_B B & 0 & t_{\text{sc}} & t_{\text{sf}} \\ 0 & \frac{\varepsilon}{2} + \frac{1}{2}g_L\mu_B B & -t_{\text{sf}} & t_{\text{sc}} \\ t_{\text{sc}} & -t_{\text{sf}} & -\frac{\varepsilon}{2} - \frac{1}{2}g_R\mu_B B & 0 \\ t_{\text{sf}} & t_{\text{sc}} & 0 & -\frac{\varepsilon}{2} + \frac{1}{2}g_R\mu_B B \end{pmatrix}. \quad (1.59)$$

By diagonalizing the Hamiltonian of Eq. (1.59), we can plot its eigenenergies as a function of detuning as shown in Fig. 1.14 with and without SOC. For these energy diagrams the g-factors are taken to be equal in both dots and the magnetic field is set at 200 mT.

Fig. 1.14.(a) is the energy diagram of the spin states without SOC where the spin degeneracy is lifted and the split by the Zeeman energy. With non SOC, the  $|-, \uparrow\rangle$  will not interact with the  $|+, \downarrow\rangle$  and the energy of the spin transition from the ground state to the first excited state is constant over detuning and given by the Zeeman energy (see Fig. 1.14.(b)). It is therefore a pure spin transition without any electric dipole moment.

Whereas in Fig. 1.14.(c) SOC is introduced and the first excited state becomes a mixture of  $|-, \uparrow\rangle$  and  $|+, \downarrow\rangle$  states at zero detuning. The spin transition from the ground to the first excited state now has an electric dipole moment. It also gives rise to the spin conserving and spin flip tunnelling coupling. The balance between  $t_{\text{sf}}$  and  $t_{\text{sc}}$  results from a competition between the Zeeman Hamiltonian and the

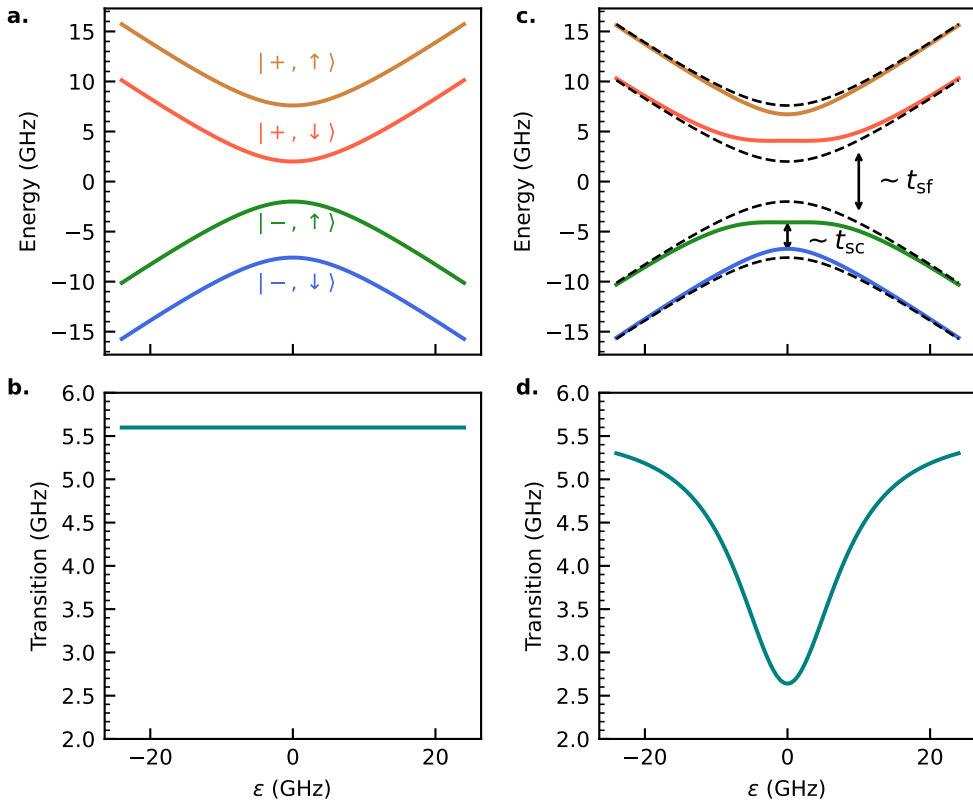


Figure 1.14 – Energy diagram of a single charge in a double quantum dot in a finite magnetic field as a function of the detuning with identical  $g$ -factors ( $g = 2$ ) and at  $B = 200$  mT. (a) In a finite magnetic field, there are four different states available. The spin  $|\uparrow\rangle$  and the spin  $|\downarrow\rangle$  are split by the Zeeman energy  $E_Z$ . The transition energy from ground state  $|-, \downarrow\rangle$  to the first excited state  $|-, \uparrow\rangle$  is plotted in (b). This transition energy is independent of  $\epsilon$  which makes it insensitive to charge noise. (c) Energy diagram of the spin states with a spin-orbit interaction plotted in colour (the black dashed lines shows the spin states without spin-orbit interaction) with the spin-flip and spin conserving tunnel couplings. The  $|-, \uparrow\rangle$  state now mixes with  $|+, \downarrow\rangle$  and the transition from  $|-, \downarrow\rangle$  to  $|-, \uparrow\rangle$  has a charge flavour. The energy of this transition is plotted in (d) and has a detuning sweet spot at  $\epsilon = 0$  GHz.

tunnelling Hamiltonians  $\mathcal{H}_{\text{sc}}$  and  $\mathcal{H}_{\text{sf}}$ . In presence of SOC, the spin transition from the  $|-, \downarrow\rangle$  to the first excited state becomes dependent of  $\varepsilon$  and dips at zero detuning. The dip in energy is directly related to the strength of the SOC and is a spin sweet spot in detuning.

### 1.4.2 Rashba spin-orbit coupling (SOC)

The single dots physics is well described by the detuning and the g-matrices. Now we focus on the tunnelling of the hole spin between the two dots. Spin-dependent tunnelling may arise because the Larmor vectors are different in each dot and/or the hole experiences Rashba spin-orbit interaction. In the former case, a hole with a given spin in the left dot projects onto a different spin in the right dot, which gives rise to a spin-flip process in the tunnelling Hamiltonian [113, 13]. This mechanism thus becomes ineffective if the two dots are sufficiently similar. On the contrary, Rashba-like spin-orbit interactions act even if the dots are identical. The Rashba spin-orbit Hamiltonian typically takes the form (for a motion along  $x$ -axis) [90, 73, 99, 49]:

$$H_{\text{so}} = \frac{\hbar^2}{m_{\parallel} \ell_{\text{so}}} k_x \mathbf{n}_{\text{so}} \cdot \sigma, \quad (1.60)$$

where  $\ell_{\text{so}}$  is the spin-orbit length,  $m_{\parallel}$  is the effective mass of the hole,  $\sigma$  is the spin Pauli operator and  $\mathbf{n}_{\text{so}}$  is the unit vector of an effective spin-orbit magnetic field  $\mathbf{B}_{\text{so}}$  which is  $\propto \mathbf{E} \times \mathbf{k}$  with  $\mathbf{E}$  the electrical field introduced by the gates and  $\mathbf{k}$  the hole momentum vector of the hole. As we work with nanowire devices, we can assume that the motion of the hole is along one axis, the  $x$ -axis.

The Rashba Hamiltonian can be interpreted as a spin-dependent field, which induces a spin rotation around  $\mathbf{B}_{\text{so}}$  associated with the motion of the hole.  $\mathbf{B}_{\text{so}}$  is given by the geometry of the device, which is enhanced with 1-dimensional device [73, 21, 98]. The spin-photon coupling results hence from an interplay of the Zeeman interaction and the Rashba SOC such that  $g_s \propto |\mathbf{g}\mathbf{B} \times \mathbf{g}\mathbf{B}_{\text{so}}|$  with  $\mathbf{g}$  the average g-matrix of the two dots. It is then expected to be the most effective when the spin Larmor vector  $\mathbf{g}\mathbf{B}$  is perpendicular to the spin-orbit field. On the other hand, if both vectors point in the same direction, the spin will not rotate.

We can translate the SOC mechanism into a spin-charge mixing parameter  $\theta$ , which is given by

$$t_{\text{sf}} = t_c \cdot \sin \theta \quad (1.61)$$

and

$$t_{\text{sc}} = t_c \cdot \cos \theta, \quad (1.62)$$

such that

$$t_c = \sqrt{t_{\text{sc}}^2 + t_{\text{sf}}^2}, \quad (1.63)$$

we retrieve the tunnelling coupling of the charge qubit.

### 1.4.3 Spin-photon coupling via intrinsic SOC

We summarize in this section the underlying mechanisms allowing for spin-photon coupling with hole spins. A schematic of the hole spin flopping mode qubit [104] coupled to a cavity can be found in Fig. 1.15.

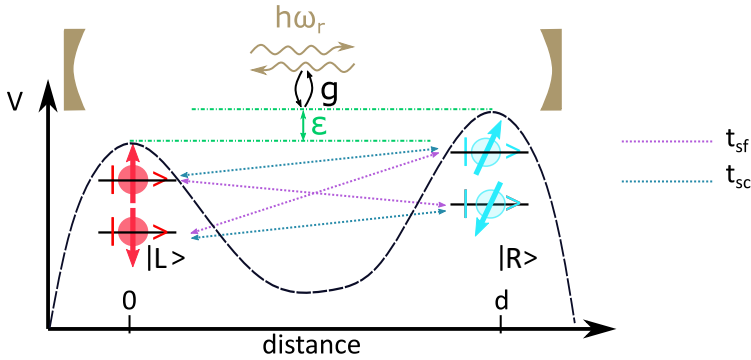


Figure 1.15 – Schematic of the spin-photon flopping mode experiment. The electric component of the cavity is coupled to the motion of the hole via electric dipole interaction and the spin couples to the hole’s motion via spin-orbit interaction and  $g$ -matrix anisotropy.

An in-plane magnetic field  $\mathbf{B}$  lifts the spin degeneracy of the DQD charge states as sketched Fig. 1.14. The two lowest spin-polarized states define a flopping mode spin qubit [104] that we want to couple to a single photon.

Spin-photon coupling is a two steps process. First the single photon is coupled to the electric dipole of the hole in a DQD, which can be tuned with the detuning between the two dots. Second, a hybridization between the charge degrees of freedom to the spin degrees of freedom is needed to enable the "indirect" spin-photon coupling. The spin-charge hybridization can be achieved through exchange interactions in a double or triple QDs [24, 82] or using spin-orbit interactions, which can be intrinsic to the QDs [73, 103, 104, 98] or induced by a magnetic field gradient [136, 36, 14]. For hole spins, we harness the intrinsic SOC in the valence band to achieve the spin-photon interaction. As the  $g$ -matrix of hole spins depends on the confinement in the dot [38], the  $g$ -matrix of both dots are different, giving rise to a different spin basis in each dot. In addition, the holes are localized in a nanowire and experience direct Rashba SOC [73]. As the spin basis are different for both dots, even if the Rashba contribution to the tunnelling is negligible, the projection of the spin state of left dot to right will carry some spin flip flavour. The Rashba SOC will rotate the spin as described in the previous section.

Fig. 1.16 shows the signature of the strong spin-photon coupling that we can probe experimentally as a function of magnetic field. The dashed lines are the non-interacting spin and photon energies, while the solid black lines are the coherent interacting states with a clear avoided crossing at the resonance condition between



the photon and the spin. This is the so-called vacuum Rabi splitting from which we can read the spin-photon coupling strength  $g_s/2\pi$ .

1

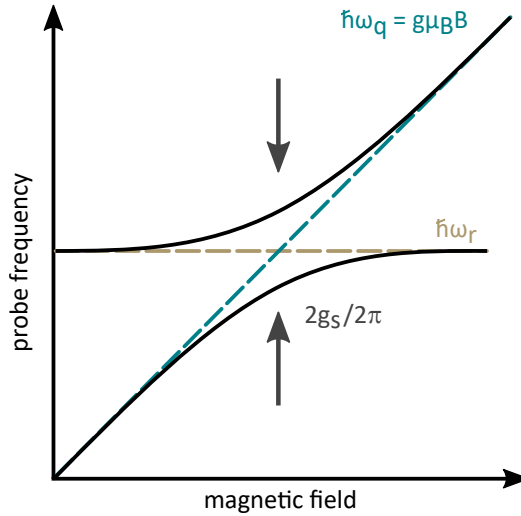


Figure 1.16 – Strong spin-photon coupling evidenced by the vacuum Rabi splitting. The non-interacting spin (blue) and photon (khaki) energies are displayed in dashed lines. In the strong coupling regime, an avoided crossing is observed at the resonance condition between the spin and the photon, this is the so-called vacuum Rabi splitting.

Hence, compared to previous circuit QED experiments of spin-photon interaction with a single electron spin in a DQD [145, 95, 124, 20, 61], hole spins give us the advantage of a simpler architecture with no micromagnet or ferromagnetic reservoirs. Indeed, the intrinsic SOC of the valence band can be many times stronger than for electron spins [22, 23]. We thus expect to probe a spin-photon coupling with a hole spin by combining the electric-dipole interaction with the charge qubit and the SOC which gives us the spin-charge hybridization.

**TAKEAWAY MESSAGES:**

- The microwave resonators are described by the transmission line model.
- The impedance and the resonance frequency of a superconducting transmission line resonator depend on its capacitance and inductance per unit length.
- Transport in a single QD is possible only when the electrochemical potential of the dot is in the bias window, otherwise the transport is forbidden by Coulomb blockade.
- A single charge in a DQD forms a charge qubit featuring an antibonding and bonding state with a qubit energy  $\hbar\omega_c = \sqrt{\varepsilon^2 + 4t_c^2}$ , with  $\varepsilon$  the detuning of the two dots and  $t_c$  the tunnel rate.
- In a finite magnetic field, the spin degeneracy of the DQD charge states is lifted up and the two lowest spin-polarized states defined a flopping mode spin qubit.
- Light-matter interaction can be described by the Jaynes-Cummings Hamiltonian.
- The strong coupling regime is attained if  $g \gg \kappa, \gamma$ .
- Hole spin-photon is governed by an interplay between an anisotropic Zeeman energy and a strong spin-orbit coupling.



# EXPERIMENTAL METHODS

## Contents

<b>2.1</b>	<b>Si-MOS quantum dots fabrication</b>	<b>34</b>
2.1.1	Silicon spin qubits architecture	34
2.1.2	Fabrication	36
<b>2.2</b>	<b>Thin NbN films</b>	<b>39</b>
2.2.1	Film growth parameters	40
2.2.2	Film characterization	41
<b>2.3</b>	<b>Co-integration of superconducting coplanar waveguide resonators with quantum dots</b>	<b>45</b>
2.3.1	Resonators design	45
2.3.2	Co-integration fabrication flow	46
<b>2.4</b>	<b>Measurement set-up</b>	<b>49</b>

We will now focus on the experimental techniques involved in this thesis. First, we want to point out that the device fabrication is a co-integration project, see [Fig. 2.1](#). The quantum dots are hosted in a nanowire silicon-MOS (metal-oxide-semiconductor) device fabricated at CEA-LETI on 300 mm wafers. The single photons are trapped in a microwave superconducting resonator fabricated in a research cleanroom facility, at the PTA (Advanced Technology Platforms) of CEA. The goal is to obtain a final device with a superconducting resonator on top of the quantum dots chip.

In this chapter, we pinpoint the different type of Si-MOS QDs and present the fabrication process of the nanowire devices from LETI. Then we focus on the challenges of the co-integration process in a circuit QED architecture. We conclude the chapter with the measurement set-up.

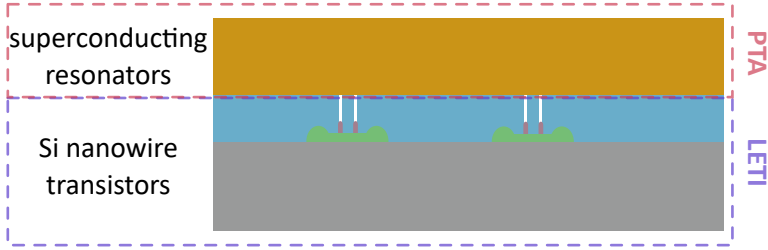


Figure 2.1 – Hybrid fabrication project between Si nanowire devices from LETI and superconducting resonators from an academic clearroom, PTA.

## 2.1 Si-MOS quantum dots fabrication

In the great race of quantum computers, silicon turns out to be a natural host platform for qubits with two obvious reasons. First, silicon is known for decades in the microelectronics industries with very mature fabrication processes for mass production. Second, silicon represents a remarkably clean magnetic environment witnessed by spins in highly purified and isotopically enriched silicon material.

In this section, we introduce different type Si-MOS quantum dots seen in the literature of spin qubits. After we give a brief description of the fabrication process of the nanowire transistors used in this project. For an extensive description of the device fabrication, readers may refer to the work of Barraud *et al.* [11].

### 2.1.1 Silicon spin qubits architecture

Spin qubits rely on the 3D confinement of electrons or holes. The most common semiconductor quantum dots in silicon are based on a layered semiconductor heterostructure Si/SiGe, which provides the  $z$ -axis confinement of the dot, and electrostatic gates are patterned on top for the confinement in the  $xy$ -plane [159, 101, 58]. These heterostructure devices have hit many milestones of quantum computation such as high-fidelity single qubit [155] and two-qubit gates [143, 150, 160]. However full-scale quantum computers require the integration of millions of qubits [46] and to meet this end the industrial microelectronics fabrication techniques would be a clear asset [139, 65]. It is then natural to develop industrial manufacturing compatible silicon devices with notably the metal-oxide-semiconductor (MOS) technology.

Fig. 2.2 summarizes the current existing structures for silicon-MOS quantum dots. They are split into three different categories: planar quantum dots, fin-FET (field-effect-transistor) and Si-MOS nanowire devices. In the planar device, fabricated in a research facility, the 3-dimensional confinement of the charges is provided by a active silicon layer with overlapping gate electrodes. The voltages applied on the gates form electrostatic potential barriers which enable the charges to tunnel in and out of the quantum dots. The fin-FET devices are fabricated in

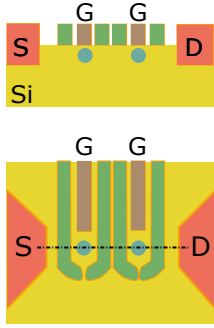
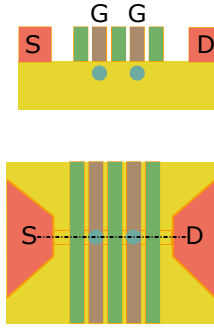
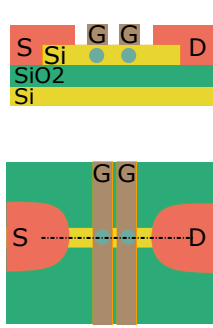
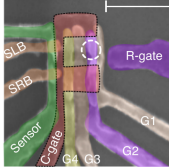
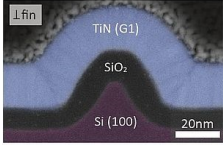
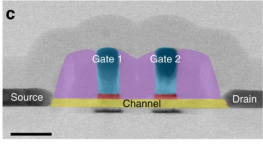
Geometry	Planar Si-MOS based quantum dots	Fin-FET based quantum dots	SOI nanowire based quantum dots
Schematic (side & top)			
Example of a device			

Figure 2.2 – Comparison of different quantum dot structures in Si. The first column shows the planar 2D quantum dots using two dimensional structures. The example shows a planar Si-MOS quantum dot from [85]. The second column shows a fin-FET based quantum dots with an example from [52]. The third column shows a nanowire on silicon oxide base quantum dots. The example is a two-gate device from [91]. The cross section schematic corresponds to the cut indicated by the black dashed lines. The plunger (barrier) gates are colorized in brown (green).

industrial-scale foundries while the nanowire devices also are from a MOS compatible cleanroom made on 300 mm wafers. The active fins are directly etched on a silicon substrate while in the nanowire device are fabricated on a silicon-on-insulator wafer. In both geometry the gate electrodes are wrapping around the active region with an oxide barrier in between. In the following we will only focus on the silicon-on-insulator nanowire devices which are key ingredients to the circuit QED experiment that we want to perform.

### 2.1.2 Fabrication

Now we cover the fabrication process of the nanowire silicon-MOS devices performed at CEA-LETI to form quantum dots as small as  $40 \times 40 \times 40 \text{ nm}^3$ .

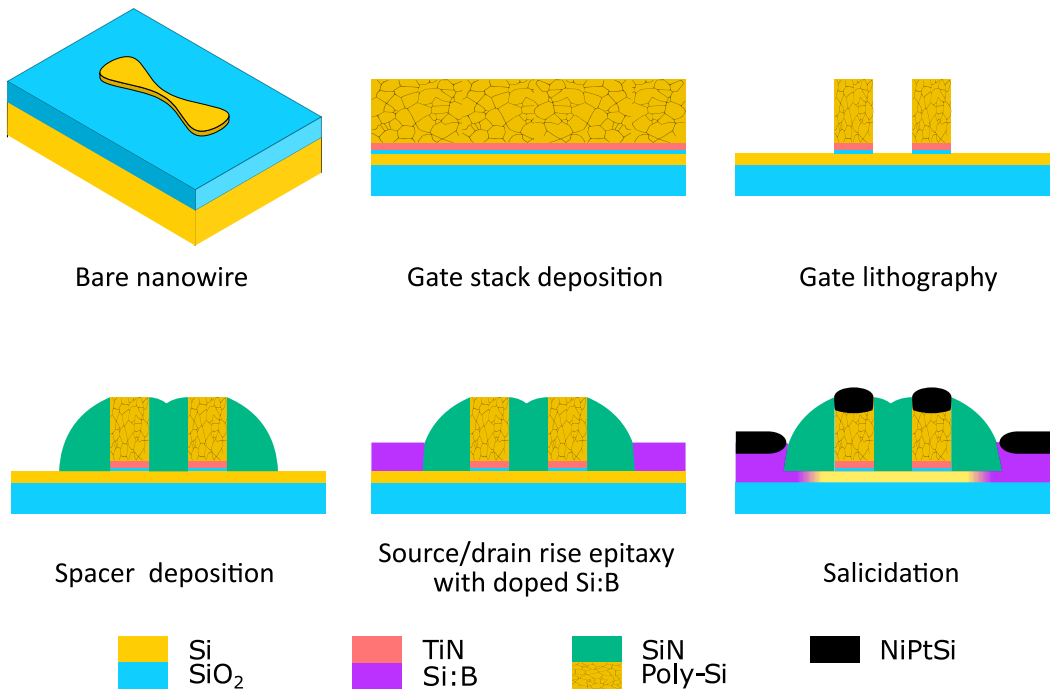


Figure 2.3 – Major steps of the Si-MOS transistors fabrication. (Adapted from [35])

The fabrication of the Si-nanowire transistors starts with a 300 mm silicon-on-oxide (SOI) wafer. The thin (8-20 nm) Si layer on top of the 145 nm thick buried oxide (BOX) is structured into narrow Si channels. The silicon nanowires are patterned using deep ultra-violet (DUV) lithography and then transferred to the silicon layer by plasma etching. To reach feature sizes below the optical resolution size, trimming (*i.e.* the resist is overetched) is performed such that the nanowires are 20-100 nm wide. Then, the gate stack is deposited on top of the nanowires, consisting of 5 nm of thermal SiO<sub>2</sub>, 5 nm of TiN and 60 nm of heavily doped poly-

Si. The gate stack is patterned using electron beam lithography (EBL) to achieve a gate pitch below 100 nm. A dry etching is performed to transfer the pattern from the resist mask to the gate stack. Then, a spacer layer made of 31 nm thick SiN is patterned to isolate the gates from each others and to protect the channel between the gates from the epitaxy process. After, on the source and drain contacts, a layer of in-situ doped silicon is grown by epitaxy and the dopants are activated in an oven at 1500 °C for 30 s. Finally, the surface of all the contacts is metallized by depositing a layer of NiPt to form the silicide alloy NiPtSi to reduce the contact resistance. The fabrication process is sketched in Fig. 2.3.

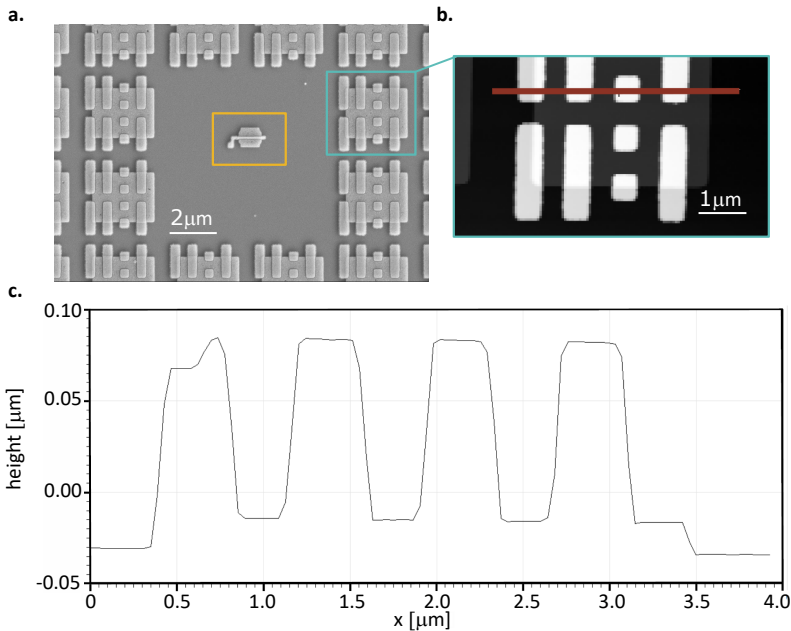


Figure 2.4 – Topography of the wafer after silicidation of the transistors. (a) Scanning microscope image of an one-gate transistor (highlighted by the yellow box) surrounded by dummy structures. (b) Atomic force microscope (AFM) image of a dummy structure. (c) Height of the dummy structure measured by AFM along the red line shown in (b). The extracted topography is  $\sim 100$  nm.

For the co-integration, we want to deposit a thin layer ( $\sim 10$  nm) of superconducting metal on top of the transistors, however at this stage of the fabrication, the wafer has a topography of  $\sim 100$  nm which makes it extremely challenging. Fig. 2.4 shows the topography of the wafer after the transistors definition. Fig. 2.4.(a) show the scanning electron microscope (SEM) image of an one-gate transistor (highlighted by the yellow box) with the dummies structures around. The dummy structures are fake transistors to maintain a constant density on the surface such that the different fabrication steps are homogeneous on the wafer scale. Indeed real transistors are only few hundreds nanometres big separated by a few micrometers from each others, the blank space in between transistors is



covered with dummies to avoid fabrication issues with isolated areas. Fig. 2.4.(b) and (c) show the atomic force microscope images of a dummy structure and its height, we extract a topography of the wafer of  $\sim 100$  nm, which is impossible to cover with a 10 nm thick film. At the early stage of this project, we have tried to remove the dummy structures while protecting the transistors. This was very challenging due to the diversity of material compositing the dummies and their aspect ratio (100 nm high but more than  $2\ \mu\text{m}$  wide).

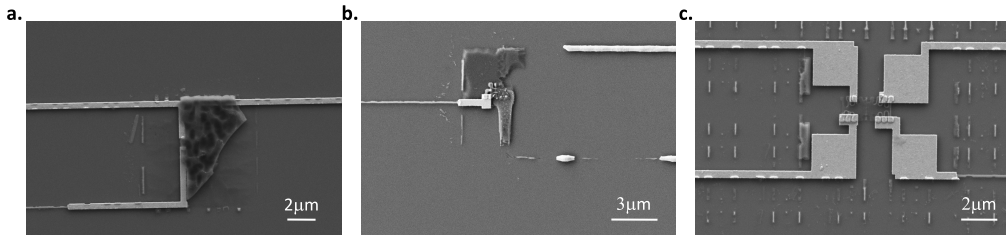


Figure 2.5 – Attempts of dummy structures removal.

The strategy to remove the dummy structures is as follows

1. Pattern sets of alignment crosses of the chip with EBL and metal evaporation.
2. Find the correspondence between the coordinates of the transistors and the crosses such that the next lithography steps would be aligned with the existing devices.
3. Contact transistors (gates, source and drain) by metal evaporation and lift-off technique.
4. Protect the transistors with a  $1\ \mu\text{m}$  thick resist (ma-N 2410).
5. Remove the dummy structures with a combination of active dry etching to thinner the dummy structures and buffered oxide etching to lift-off the dummies by attacking the oxide layer below.

Fig. 2.5 shows different attempts of removing the dummy structures. The success rate until recontacting the transistor is kind of high but the dummies removing part was kind of unsuccessful. The etching process was too heavy and the protection was not efficient enough. We never succeeded to remove completely the dummies while keeping the transistors.

Removing the topography of the wafer is a very hot issue and after discussions with the LETI team, we have obtained an extra step of planarization. The extra fabrication steps are recapitulated in Fig. 2.6. First a contact etch stop layer (CESL) made of 34 nm thick of SiN is grown everywhere, followed by the growth of 450 nm thick of SiO<sub>2</sub> by plasma-enhanced chemical vapour deposition (PECVD). Since the contacts of the source and drain are not at the same level than the contacts of the gates, the CESL layer will enable a non-uniform etching to reach the contacts. A first planarization is performed by CMP to thin down the SiO<sub>2</sub>

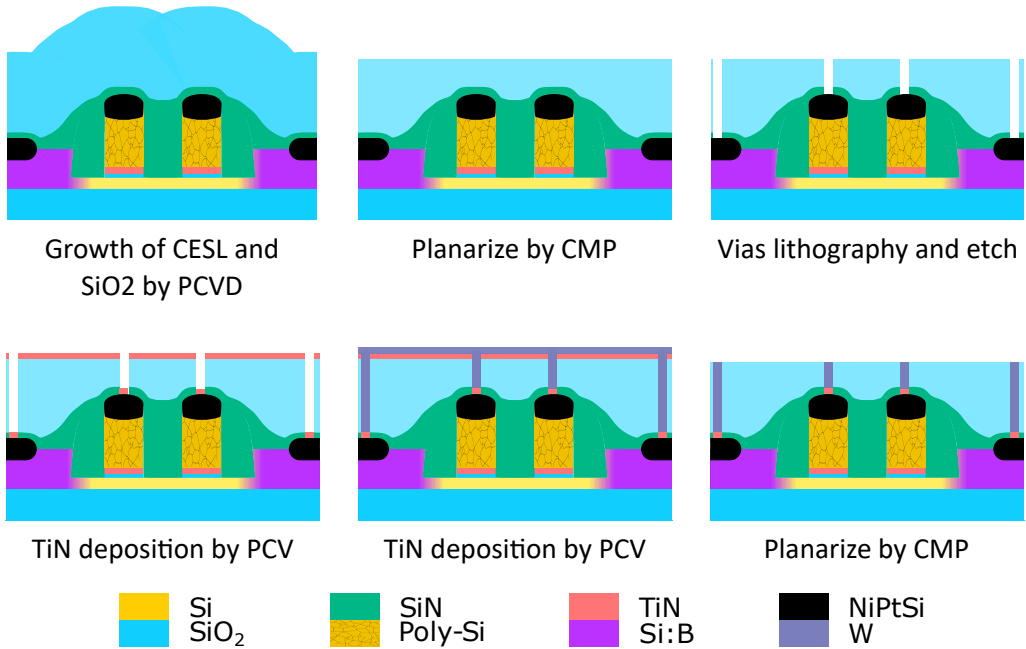


Figure 2.6 – Fabrication process of the planarized transistors wafer with electrical contacts in tungsten.

layer to 200 nm. Vias are patterned by DUV lithography then a first etch is performed down to the CESL followed by a second etch step to remove the CESL locally. A few nanometers of TiN is deposited by plasma vapour deposition (PVD) before the filling of the vias with tungsten by chemical vapour deposition (CVD). Finally the wafer is planarized by CMP again to remove any topography and is ready to be processed for the superconducting resonators.

## 2.2 Thin NbN films

Now that the fabrication of the silicon MOS transistors is reviewed, we can proceed with the second ingredient of the circuit QED experiment, the superconducting resonators. Our superconducting candidate is a thin film of niobium nitride (NbN) due to the following reasons. First, NbN films have a high critical temperature of 16 K in the bulk material and  $\sim 7$  K for 10 nm thick films, allowing film characterizations at 4 K in liquid helium. Second, NbN is also highly resilient to magnetic fields, due to its high critical magnetic field, which is a great asset to work with spin qubits that require the presence of a magnetic field. Last, thin films of NbN show a high kinetic inductance which helps to create high characteristic impedance resonators.

In addition, there is a history of NbN growth in our group for microwave

photonics applications [122, 55]. However when I arrived in the laboratory, a new sputtering machine was bought, then I started by some optimization work on it, together with F. Gustavo, to find a new recipe suited for the circuit QED experiment. This section presents, hence, the growth and optimization of thin NbN films for the circuit QED experiments with spins.

### 2.2.1 Film growth parameters

The NbN films are made by sputtering in a Plassys MP600S confocal sputtering system. The chamber is equipped with a pure niobium (Nb) target and NbN is formed by introducing a small flow of nitrogen gas during the deposition in addition of the inert argon gas. Indeed, as the partial pressure of  $N_2$  increases, the outermost surface of the Nb target will transit from a purely metallic state to a nitride state [53, 10]. Here we describe some of the growth parameters optimization of the NbN deposition.

As the NbN films depend on the quantity of nitrogen introduced in the plasma chamber, we start with the exploration of the target voltage as a function of nitrogen flow, see Fig. 2.7. This curve is obtained with a target current of 1 A and an Ar flow of 70 sccm, which are parameters directly inherited from the previous sputter system. The evolution of the target voltage is an indicator of the nitridation state of it [141].

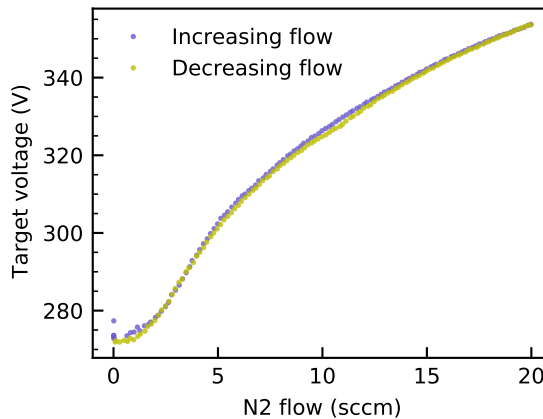


Figure 2.7 – Target voltage as a function of nitrogen flow. The voltage response is similar for an increasing or decreasing nitrogen flow.

First, the target voltage increases very fast. At this stage, the nitrogen inside the chamber is consumed by the Nb target in order to form the NbN compound. Then at higher nitrogen flow, the target is saturated in the nitriding process [141] and the voltage increases slower. Hence for pre-sputtering time (the target is covered), the nitrogen flow is set to a high value achieve the formation of NbN, then the target is exposed to the plasma and we reduce the flow of nitrogen.

Current	Pressure	Ar flow rate	N <sub>2</sub> flow rate	$T_c$
2.0 A	10 <sup>-2</sup> mbar	18 sccm	5 sccm	9.5 K
0.9 A	10 <sup>-2</sup> mbar	18 sccm	5 sccm	9.8 K
2.0 A	10 <sup>-2</sup> mbar	60 sccm	15 sccm	10.6 K
2.0 A	10 <sup>-2</sup> mbar	70 sccm	15 sccm	11.2 K
2.0 A	10 <sup>-2</sup> mbar	35 sccm	42-45%	11.8 K

Table 2.1 – Influence of sputtering parameters of bulk (50 nm) NbN on the critical temperature.

The nitrogen flow is one parameter among many others that can be tuned to change the properties of the NbN films. [Table 2.1](#) summarizes different sputtering recipes varying the target current, the argon flow or the nitrogen flow and the obtained critical temperature,  $T_c$  of a bulk NbN (at least 50 nm thick). The measurement  $T_c$  is detailed in the next section. Based on the critical temperatures, we have chosen the last sputtering conditions presented with the higher  $T_c$ , with a deposition rate of  $\sim 0.9 \text{ nm s}^{-1}$ . As the final objective of the NbN film is to create a microwave cavity that is galvanically connected to a gate electrode of a transistor, we perform a soft 30 s Ar milling before sputtering to remove any oxide on the wafer preventing from electrical contact. The detailed sputtering conditions are given in [Appendix B](#).

## 2.2.2 Film characterization

Now we focus on a 10 nm thick NbN film and its superconducting properties. The deposition here is performed on  $525 \pm 25 \mu\text{m}$  thick p-type silicon wafers (1-15  $\Omega \text{ cm}$ ), covered by  $400 \pm 80 \text{ nm}$  of thermally grown  $\text{SiO}_2$ .

### Kinetic inductance

The important characteristics of films are the critical superconducting temperature and the kinetic inductance. Both information can be extracted using a physical property measurement system (PPMS) by Quantum Design which measures the resistance of a given film as a function of the temperature by a four-probe measurement technique. The sample is inserted in a helium dewar which covers temperature from 2 K to 400 K with an out-of-plane magnetic field up to 9 T.

To extract the resistivity of the film, we pattern a four-probe structure on the NbN film as shown in [Fig. 2.8.\(a\)](#). A typical  $R(T)$  measurement from room temperature to the superconducting transition is shown in the inset of [Fig. 2.8.\(b\)](#) and [Fig. 2.8.\(b\)](#) is a zoom in around the superconducting transition. The sheet resistance increases while lowering the temperature from room temperature to  $\sim 19 \text{ K}$ . From 19 to 5 K the resistance decreases until zero resistance, marking the superconducting transition. The rise of the sheet resistance before the superconducting transition is typical of weak localization and Coulomb interaction in

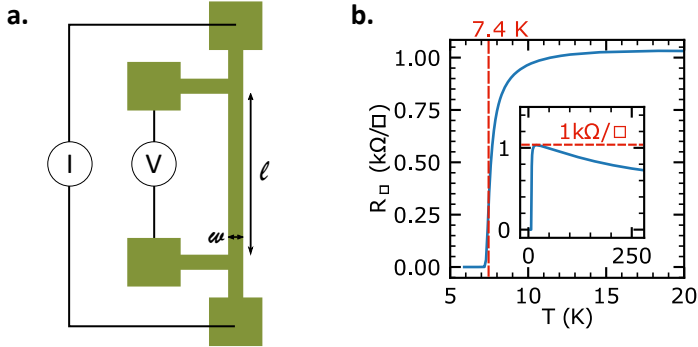


Figure 2.8 – DC characterization of the NbN films. (a) Four-probe resistivity measurement structure. (b)  $R(T)$  characteristics of a 10 nm thick NbN film,  $T_c = 7.40$  K and  $R_{\square} = 1033 \Omega \square^{-1}$ .

strongly disordered superconductors [120].

The critical temperature  $T_c$  can be directly read on the  $R(T)$  curve as the inflection point, see Fig. 2.8(b). The kinetic inductance can be estimated as

$$L_{\text{kin}} = \frac{\hbar R_{\square}}{\pi \Delta_0}, \quad (2.1)$$

where  $R_{\square}$  is the sheet resistance,  $\hbar$  is the reduced Planck constant and  $\Delta_0$  is the superconducting gap at zero temperature. From [6], we assume that the superconducting gap for NbN is given by  $\Delta_0 = 1.76 k_B T_c$  where  $k_B$  the Boltzmann constant. Using a four-probe structure of known dimensions, as shown in Fig. 2.8.(a), the resistance, in  $\Omega$  of the film can be converted into the sheet resistance, in  $\Omega/\square$ :

$$R_{\square}(\Omega/\square) = R(\Omega) \cdot \frac{\ell}{w}, \quad (2.2)$$

with  $\ell = 4600 \mu\text{m}$  and  $w = 100 \mu\text{m}$ .

We extract the sheet resistance  $R_{\square} = 1033 \pm 1 \Omega \square^{-1}$  as the maximal value of the curve and the critical temperature  $T_c = 7.4 \pm 0.1$  K, see Fig. 2.8.(b). For this 10 nm thick NbN film, we deduce a kinetic inductance value of

$$L_{\text{kin}} = 192 \pm 3 \text{ pH } \square^{-1}.$$

This film will be the one used in the fabrication of the resonators, see Chap. 3, and the kinetic inductance contribution is reproducible from one growth to another. Note that the kinetic inductance of a film depends on its thickness, therefore higher value of  $L_{\text{kin}}$  could be attained with thinner films but  $T_c$  would be lower and films below 10 nm thick tend to be less reproducible.

To confirm the kinetic inductance value extracted via Eq. (2.1), we have also performed an independent RF measurement based on a two-tone spectroscopy [81]

to map the dispersion relation of the film. The kinetic inductance extracted with this second technique matches perfectly with the DC measurement. The complete description of this experiment can be found in [Appendix C](#).

### Critical magnetic field

From the PPMS measurement, we can also extract the critical magnetic field of the NbN films. The applied magnetic field is perpendicular to the NbN chip. The Werthamer-Helfand-Hohenbert theory [151] predicts a linear behavior of the upper critical magnetic field  $B_{c2}(T)$  down to  $T = 0$  K as follows

$$B_{c2}(0) = 0.69T_c \left( \frac{dB_{c2}(T)}{dT} \right)_{T_c}. \quad (2.3)$$

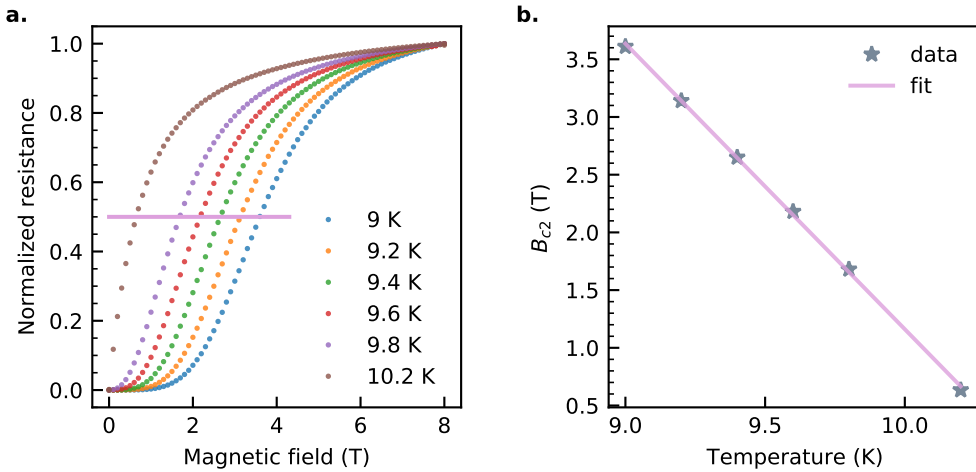


Figure 2.9 – Upper critical magnetic field  $B_{c2}$  of a 10 nm thick NbN film. (a) Resistance as a function of magnetic field at fixed temperatures below  $T_c$ . The pink line indicates the resistance value at which  $B_{c2}$  is determined for each temperature. (b) Temperature dependence of the upper critical magnetic field  $B_{c2}$ .

The 10 nm NbN film is a different one from the kinetic inductance measurement. Here, it has a critical temperature of 10.2 K, which is higher than the one used later on but we never achieve such a high  $T_c$  anymore. To measure the critical magnetic field, we apply an out-of-plane magnetic field up to 8 T and we vary the temperature below  $T_c$  from 9 K to 10.2 K. At each temperature, we sweep the magnetic field from 0 T to 8 T. [Fig. 2.9\(a\)](#) shows the resistance of the film as a function of magnetic field at fixed temperature. From this curve, we extract the upper critical magnetic field  $B_{c2}$  at half of the normalized resistance. We then plot  $B_{c2}$  as a function of temperature, see [Fig. 2.9\(b\)](#), to extract the linear dependence

on  $T$  of  $B_{c2}$ . From the linear fit, we obtain

$$\left(\frac{dB_{c2}(T)}{dT}\right)_{T_c} = 2.5 \text{ T K}^{-1}, \quad (2.4)$$

and the upper critical field at zero temperature is therefore

$$B_{c2}(0) = 17.4 \text{ T}, \quad (2.5)$$

which is agreement with other measurements of  $B_{c2}$  on NbN films [71, 142].

From  $B_{c2}$  we can also extract the coherence length in the dirty limit by [135]

$$\xi(0) = \sqrt{\frac{\Phi_0}{2\pi B_{c2}(0)}}, \quad (2.6)$$

with  $\Phi_0 = \pi\hbar/e$  the magnetic flux quantum,  $e$  the elementary charge and  $\hbar$  the reduced Planck constant. We then estimate the coherence length of our film to be  $\xi(0) = 4.35 \text{ nm}$ , which is consistent with the literature [149, 30, 72]. The short coherence length and the high critical magnetic field of the thin NbN films are clear assets to work in a magnetic field environment for the spin manipulations.

## Substrate temperature

We investigate on one more sputtering parameter which is the substrate temperature. In Table 2.2, we summarize several NbN depositions made at different substrate temperatures in order to investigate its influence on the kinetic inductance of the film. All films are 10 nm thick and the heating process of the substrate always lasts for  $\approx 16 \text{ h}$  prior to deposition. The difference between films with the same substrate temperature shows the variability on the sputtered films.

Table 2.2 – NbN film characterization for different sputtering temperatures.

Temperature ( $^{\circ}\text{C}$ )	$R_{\square}$ ( $\Omega \square^{-1}$ )	$T_c$ (K)	Kinetic inductance ( $\text{pH} \square^{-1}$ )
275	273	10.5	36
275	339	9.6	49
180	480	7.7	86
180	550	7.4	103
22	670	5.9	162
22	705	5.6	174

Note that the kinetic inductance in Table 2.2 is an estimate from the sheet resistances at room temperature. It is a lower bound of the real kinetic inductance as the resistance increases from 300 K to the superconducting transition due to the disordered properties of NbN, see Fig. 2.8.(b) inset. The film with a kinetic inductance estimated at  $103 \text{ pH} \square^{-1}$  corresponds to the one studied in details with

a real kinetic inductance of  $192 \text{ pH} \square^{-1}$ . A substrate temperature of  $180^\circ\text{C}$  is a compromise between the kinetic inductance and the critical temperature.

The material growth is a complex field of physics with a lot of parameters, we can surely further improve the quality of our films but for the high-impedance resonators we will stick to the  $10 \text{ nm}$  thick films with  $L_{\text{kin}} = 192 \pm 3 \text{ pH} \square^{-1}$ .

## 2.3 Co-integration of superconducting coplanar waveguide resonators with quantum dots

We now proceed with the co-integration process of the quantum dots with microwave resonators. We start with a description of the resonators design procedure such that the resonance frequency is in the bandwidth from  $4 \text{ GHz}$  to  $8 \text{ GHz}$  and the characteristic impedance of the resonator is higher than  $50 \Omega$  without putting too much constrain on the fabrication side. Then we review the co-integration fabrication process and its challenges.

### 2.3.1 Resonators design

Once the properties of the NbN films are known, we can proceed to the design of the high-impedance resonators. The most important characteristics of a resonator are its resonance frequency and its characteristic impedance, both are given by the capacitance and inductance per unit length

$$f_0 = \frac{1}{2\ell} \frac{1}{\sqrt{L_\ell C_\ell}}, \quad (2.7)$$

$$Z_0 = \sqrt{\frac{L_\ell}{C_\ell}}. \quad (2.8)$$

Once the kinetic inductance of the film is known, we can use the Sonnet software to estimate the capacitance and the inductance of the coplanar waveguide by using the planar metal loss model with the resistivity set to zero ( $R_{\text{DC}}$  and  $R_{\text{RF}}$ ), the DC reactance to zero and the surface inductance to the kinetic inductance of the NbN film.

The resonators are integrated on top of the MOS wafer. Not only does the wafer have transistors buried below the silicon oxide but also dummies which are fake transistors, as explained in [Sec. 2.1](#). Therefore, microwave simulations of such a wafer are very complex. Then a virtual substrate is created in Sonnet to simulate the resonators as shown in [Fig. 2.10.\(a\)](#). The characteristic impedance and the resonance frequency of a coplanar waveguide resonator can be estimated by simulating a small section of the waveguide and Sonnet can compute the LRCG matrix using the *Output N-coupled line model*. [Fig. 2.10.\(a\)](#) also shows the hanger like geometry of the resonators, which means that one or several resonators are capacitively coupled to a almost  $50 \Omega$  feedline.



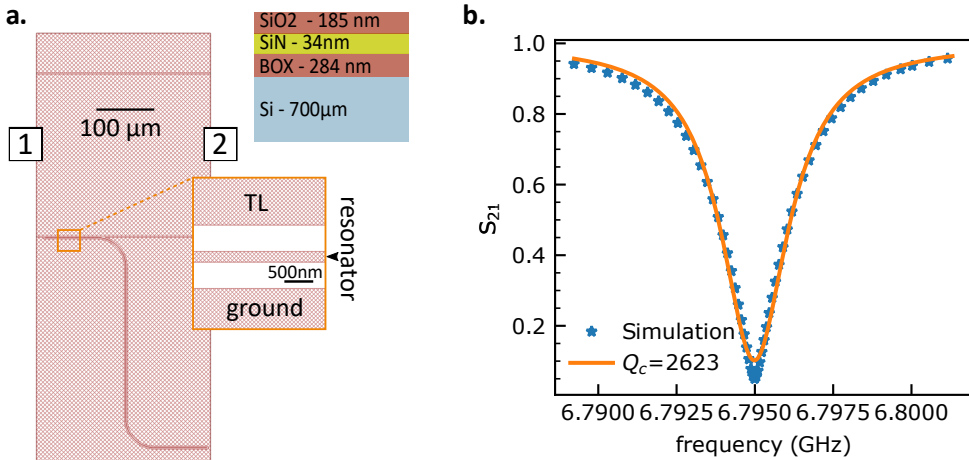


Figure 2.10 – Resonators simulation on Sonnet. (a) Two-port simulation on Sonnet with a  $50\ \Omega$  transmission line and a high-impedance resonator, and the substrate composition to mimic the CMOS wafer. On the resonator design, the metal part is colored in red. The insert part shows the virtual substrate to mimic the transistor wafer. (c)  $S_{21}$  response of the resonator simulated by Sonnet and its Lorentzian fit to extract the  $Q_c$  assuming that  $Q_i$  is infinite. Here  $Q_c = 2623$ .

Besides of the geometry, the internal and external quality factors are also a key parameter in the resonators design. The internal quality factor  $Q_{\text{int}}$  mostly depends on the substrate and the cleanliness of fabrication process, whereas the coupling quality factor  $Q_{\text{ext}}$  is given by geometry. Therefore  $Q_{\text{ext}}$  can be simulated, while  $Q_{\text{int}}$  can only be accessed by a measurement once the sample is fabricated. For the hanger geometry resonators, we extract  $Q_{\text{ext}}$  by simulating the full resonator as shown in Fig. 2.10(a). As the intrinsic losses of the system are set to zero in the simulation, the total quality factor equals to the coupling quality factor. Then by simply fitting the  $S_{21}$  response with a Lorentzian model, the quality factor can be estimated, see Fig. 2.10(b). Armed with the simulation results, we can now turn to the fabrication of the resonators.

### 2.3.2 Co-integration fabrication flow

In this section, we give an overall description of the fabrication process while a complete description can be found in Appendix B. The main challenge in the co-integration of the resonators with the transistors is the alignment of the two components. Indeed, the tungsten vias ensuring the electrical contact to the transistors are  $90\ \text{nm}^2$  big, thus the alignment has to be accurate up to a few tens of nanometers. To achieve such a good accuracy over centimeters long distances, we need a very good precision on the coordinates of the alignment crosses.

After the planarization of the MOS wafer as explained in Sec. 2.1.2, one more DUV lithography step is implemented to define alignment crosses. Once the tran-

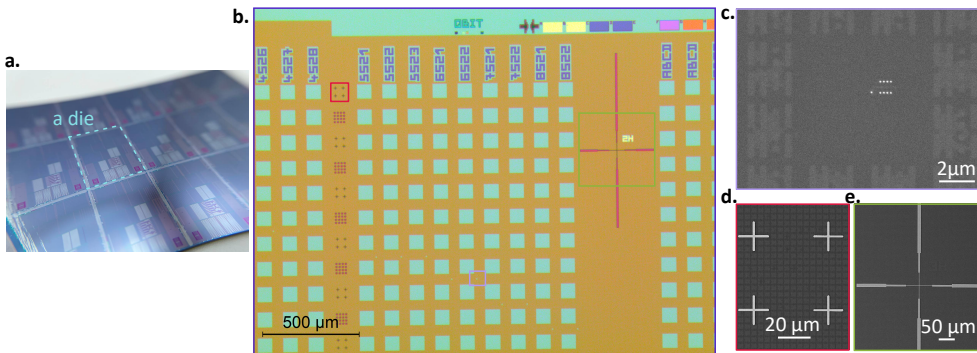


Figure 2.11 – Images of a die from macroscopic to microscopic. (a) Photo of a die on the 300 mm wafer before being cleaved. (b) Optical image of the upper right part of a die with the alignment crosses. The yellow region is the dummy structures and the green region are the buried oxide (BOX). (c) SEM image of a transistor with W vias surrounded by dummies. (d) SEM image of a set of chip crosses made of platinum. (e) SEM image of a global cross made of platinum.

sistors are finished and buried under the silicon oxide layer, a photoresist (TARF P9009) is spin coated on the wafer with a layer of anti-reflective coating (BARC AR19) below. During the DUV lithography step, only the photoresist layer is exposed and developed, while the anti-reflective coating remains all over the wafer. That is the final step performed by the CEA-LETI quantum silicon team.

Fig. 2.11 shows images of a die from macroscopic to nanometric scales. We start with a 300 mm wafer full of identical dies, Fig. 2.11.(a) shows a photo of several dies, each die is  $13 \times 17 \text{ mm}^2$ . For the co-integration, we will proceed with the fabrication die per die that we separate from the 300 mm wafer by cleaving with a diamond pen. Fig. 2.11.(b) shows an optical image of the upper right part of a die with one big global alignment cross, highlighted by a green box, and one column of chip marks composed of small crosses, marked by a red box. Fig. 2.11.(c) is a zoom on one of the transistors using the scanning electron microscope (SEM). The bright white dots are the tungsten vias connecting the transistor to the surface of the die and the features around are the dummies. Fig. 2.11.(d) and (e) are the SEM images of a set of chip marks and a global cross. The fabrication of the crosses are detailed in the paragraph below.

As the first step of the post-processing part, the alignment crosses are defined by metal evaporation and lift-off technique (see Fig. 2.12). Before any metal evaporation, we need to first etch away the BARC layer below the cross patterns, otherwise the lift-off step will fail. To do so, we use an ICP etcher, SI 500 324 from SENTECH, with an oxygen plasma to remove the 82 nm thick BARC layer. During that step, we also etch part of the photoresist but since it is 1 μm thick we can afford such a loss. After, we deposit by evaporation, in a MEB550 from Plassys, 50 nm of platinum with 5 nm of chromium as an adhesion layer. Then the

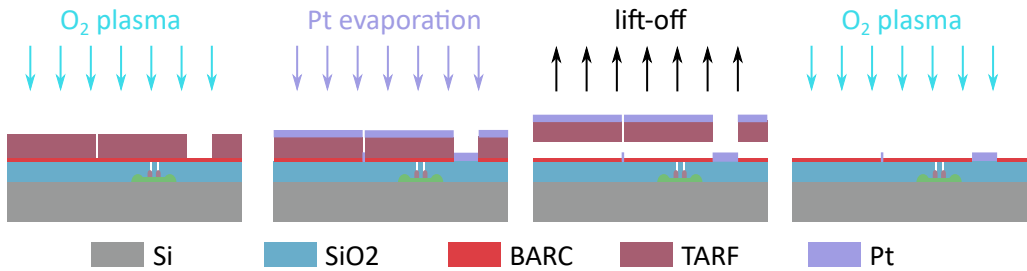


Figure 2.12 – Fabrication process of the alignment crosses. First the anti-reflective layer is etched away by an oxygen plasma. Then 50 nm of Pt is evaporated on the wafer and the crosses are defined by lift-off technique. A second oxygen plasma removes the remaining anti-reflective layer.

extra metal part are lifted-off in ethyl lactate which is a remover for the photoresist. At this stage, there is still a BARC layer on the sample preventing from electrical contacts with the devices. One last oxygen plasma is performed on the sample to remove this layer and the chip is fully marked with alignment crosses and ready to be post-processed. With an automatic detection of the alignment crosses, the EBL can be accurate up to 20 nm using only three global marks and one set of chip marks, which represents the top accuracy of the JBX-6300FS model from JEOL.

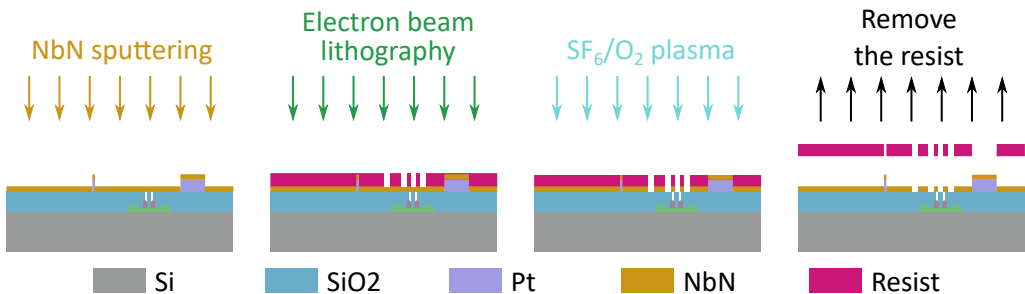


Figure 2.13 – Fabrication process of the superconducting NbN resonators. A 10 nm thick NbN film is deposited by sputtering. A EBL is performed to pattern the resonators, then the pattern is transferred to the NbN layer by dry etching.

Right after the last oxygen plasma step, the 10 nm thick NbN film is deposited as indicated in [Sec. 2.2](#). The resonators are then defined by EBL with a ZEP 502A resist diluted in IPA with a [1:1] ratio. The pattern is transferred to the NbN layer, using the ICP tool Plasmalab100 from Oxford Instruments, with a  $\text{SF}_6/\text{O}_2$  plasma. Eventually, the resist is removed by DUV exposure before being developed in a MIBK:IPA solution. The different steps of the resonators fabrication are sketched in [Fig. 2.13](#).

After the nanofabrication of the resonators, we have to dice the chip such that it fits in our sample holder which is  $1\text{ cm}^2$  big. This is done using an automated

diamond saw, DISCO DAD 321, with a protective resist layer (AZ1512) on the chip. Once the chip is cut into the right size, we clean the chip and remove the protective resist. Last, we perform an annealing step to remove any charges accumulated unwillingly during the fabrication process. The annealing step is done under a forming gas  $N_2/H_2(4\%)$  atmosphere at  $400^\circ\text{C}$  during 1 h with a continuous circulation of the gas. Then the chip is ready to be glued on a PCB with silver paint and bonded for measurements.

Fig. 2.14 shows SEM images of a finished resonator connected to a two-gate silicon transistor with DC bias lines. Each of the DC lines are filtered by an LC filter to prevent from microwave leakage as we will explain in Sec. 3.2.2.

## 2.4 Measurement set-up

Measurements have been performed in a Bluefors dilution refrigerator with a base temperature of  $T_{\text{base}} \approx 8\text{ mK}$ . The cryostat is divided into various temperature stages as indicated in Fig. 2.15.(d). Besides, the fridge is equipped with a bottom-loading system (see Fig. 2.15.(c)), which offers a fast sample exchange solution leaving the dilution unit at 4 K.

The sample is bonded to a printed circuit board (PCB) (see Fig. 2.15.(a)), this is the so-called daughter board with two RF connectors used to measure the microwave resonators in transmission. This daughter board is then mounted to a mother board, as shown in Fig. 2.15.(b), with ten other RF connectors and 24 DC lines. Signals from the mother board are routed to the daughter board through an interposer with fuzz buttons. Once connected, the mother board is mounted on the probe of the bottom loader which inserts the sample in the cryostat.

At room temperature, the top of the fridge is connected to DC electronics for biasing and read-out of the quantum dots and RF electronics to probe the resonators. The DQD gates are biased using digital analog converters (DACs) (iTest BN110) and a matrix box which hosts an electrical switch for each DC line. Inside the cryostat, 24 DC lines with RF and DC filters go to the sample at base temperature. When the transistor can be directly biased on its source, a current-to-voltage (IV) converter (Femto DLPCA200) is used to measure the resulting current at the drain for transport measurements. When the source is hard-grounded, to reduce the number of gates on the chip, a biasable home-built IV converter is used to apply a voltage bias to the transistor such that we can still measure in transport. The electrical transport measurements are usually performed at room temperature to ensure that the alignment or the electrical contact is good, and more importantly the transistors have not been damaged during the fabrication or bonding steps.

The superconducting resonators are measured in transmission using a two-port vector network analyzer (VNA) from Copper Mountain. The input signal is sent to the sample with a discrete attenuation of 60 dB inside the cryostat. The output signal from the resonator is filtered with a 4-8 GHz bandpass filter and a

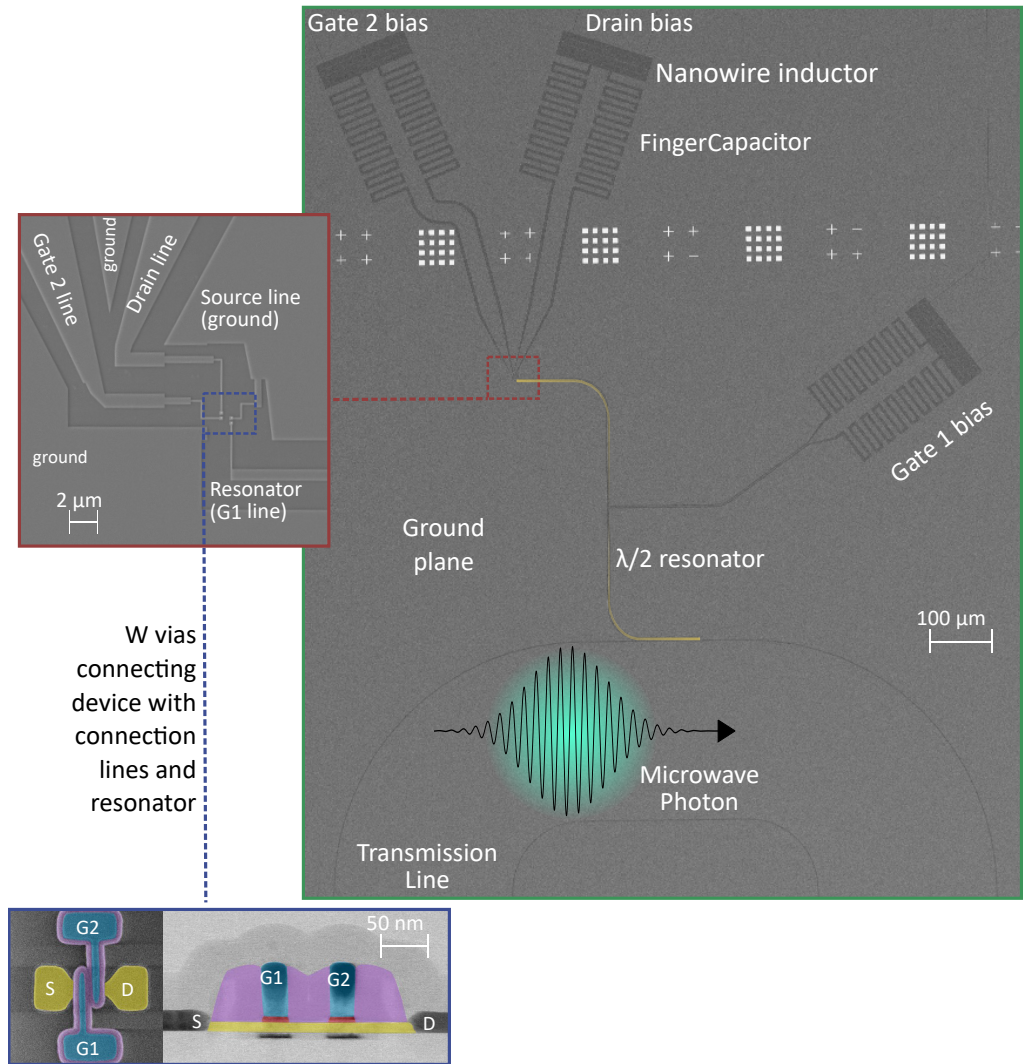


Figure 2.14 – SEM image of a NbN resonator connected to a two-gate silicon transistor. The main panel shows the full circuit QED design with the transmission line, the high-impedance resonator, DC bias lines and alignment marks. The contact geometry of the wiring from the end of the resonator to the tungsten vias of the transistor is shown in the red boxed region. The blue boxed image shows a top view of a two-gate transistor by SEM and its cross-section by transmission electron microscopy. (Adapted from [70])

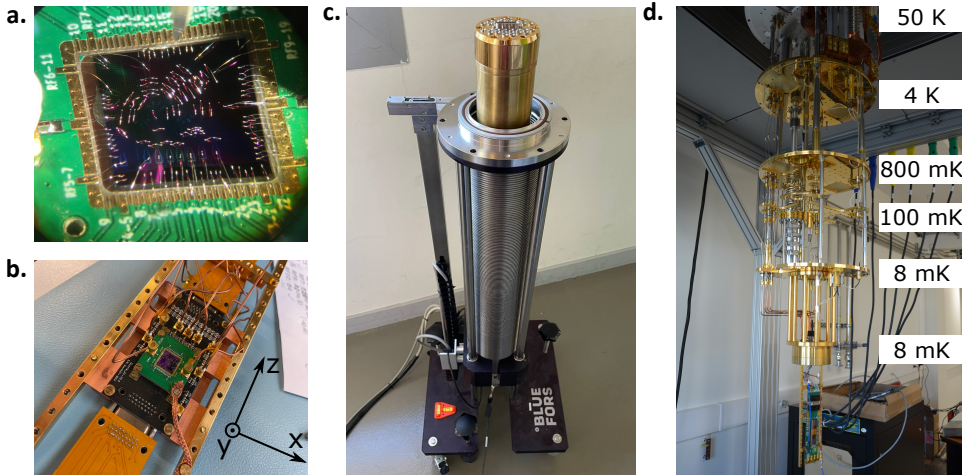


Figure 2.15 – Photographs of measurement set-up. (a) Sample chip bonded to the daughter PCB with RF and DC connections. (b) Daughter board connected to the mother board in the bottom loader's probe with DC (flex PCB) and RF (Cu cables) lines. (c) Bottom-loading system with the sample inside the probe. (d) Cryostat with the different temperature stages and the probe mounted.

two-junction isolator before reaching an HEMT (high electron mobility transistor) low-noise amplifier mounted at 4 K. The signal reaches a circulator (DiTom D3C4080) before being further amplified (Amplitech apt3-04000800-0610-ME3) at room temperature before being measured by the VNA. The bandpass filter, isolator, circulator and attenuators protect the superconducting resonators from thermal radiations. All RF lines are equipped with DC blocks at room temperature before going in the cryostat to avoid ground loops. For two-tone spectroscopy, an Agilent RF source (E8257D) is used in addition to the VNA, whose clocks are synchronised together. In order to reach the single photon regime, room temperature attenuators are usually added at the output of the VNA to reduce the input power at the resonator. See Fig. 2.16 for a typical DQD measurement set-up with the sample chip bonded on the daughter PCB.

In order to manipulate the spin degree of the charge carriers inside the quantum dots, a superconducting 3D vector magnet is placed in the cryostat. It is thermally and mechanically connected to the 4 K plate such that the sample is positioned at the center of the magnetic field. The magnets generate high magnetic fields up to 6 T in the vertical  $z$  direction and up to 1 T in a full sphere in any direction. The magnetic directions as indicated in Fig. 2.15.(b).

2

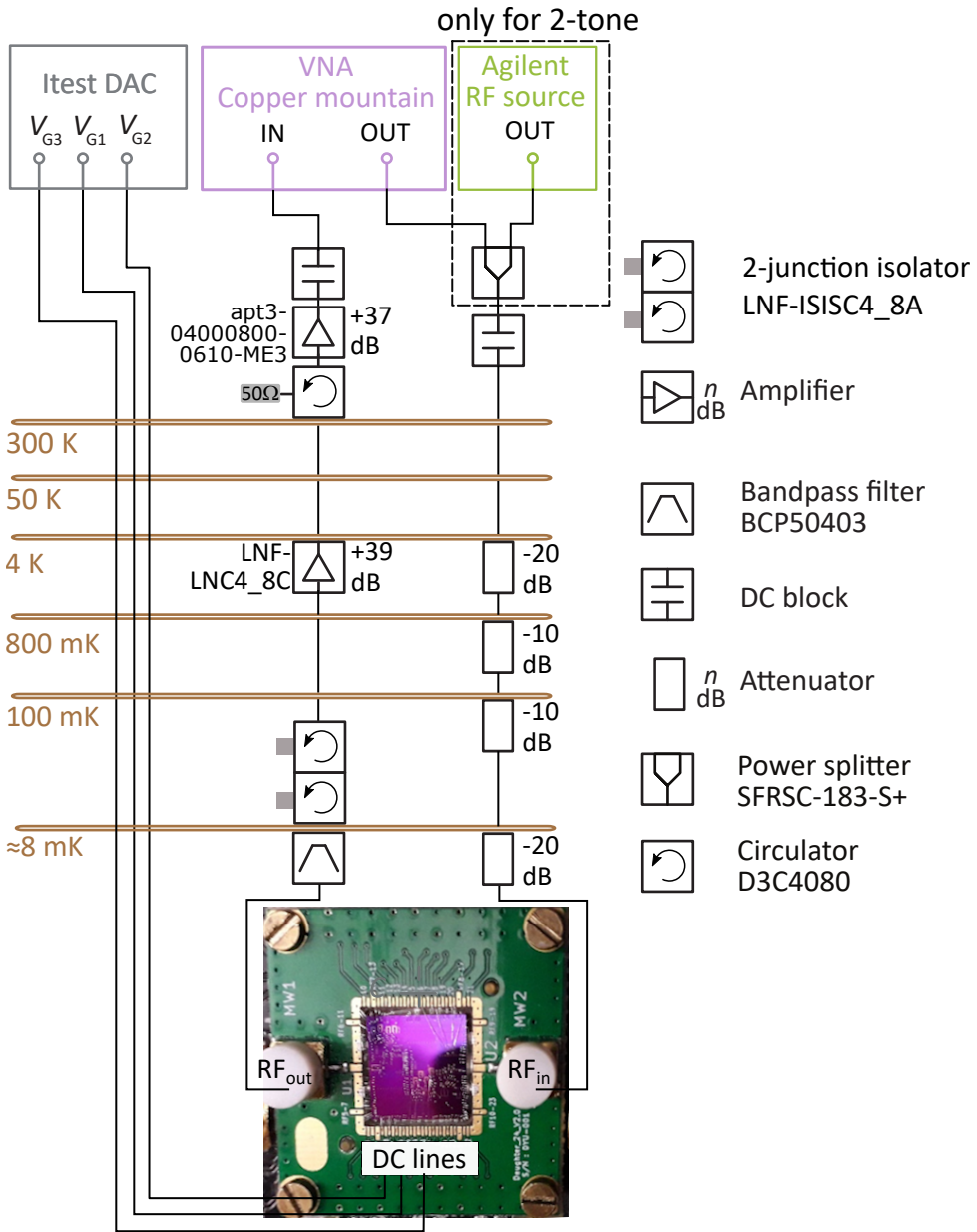


Figure 2.16 – Schematic of the measurement setup for a DQD device with the sample chip bonded on the daughter PCB. The VNA provides microwave signals for the resonator which can be combined with a microwave generator for two-tone measurement. The output signal of the resonator is filtered and amplified.

**TAKEAWAY MESSAGES:**

- The quantum dots are hosted in a silicon MOS nanowire transistor fabricated on 300 mm wafers.
- The back-end-of-line fabrication of the silicon chip is interrupted in order to replace the first metallic interconnect layer with a 10 nm thick NbN film.
- The thin NbN film, deposited by sputtering, shows a high kinetic inductance  $L_{\text{kin}} = 192 \pm 3 \text{ pH } \square^{-1}$ .
- The alignment of the resonators on the transistors is accurate up to 20 nm over a centimeters long distance.
- The samples are held at a temperature  $T_{\text{base}} \approx 8 \text{ mK}$  using a dilution refrigerator equipped with a 3D vector magnet and bottom-loading system.
- The quantum dots transport characterization are performed using low-noise DACs and the resonator's response is read by a VNA.





# NbN SUPERCONDUCTING RESONATORS IN THE COPLANAR WAVEGUIDE GEOMETRY

## Contents

---

<b>3.1 NbN superconducting resonators characterizations on Si substrates</b> . . . . .	<b>56</b>
3.1.1 Basic characterization . . . . .	56
3.1.2 Power dependence . . . . .	58
3.1.3 Magnetic fields resilience . . . . .	60
<b>3.2 Extra microwave challenges in the cQED geometry</b> . .	<b>63</b>
3.2.1 Influence of the substrate . . . . .	63
3.2.2 Microwave leakage due to additional gate lines . . . . .	65

---

**B**efore coupling a photon to a charge or a spin, we first study the resonators to ensure that the photon loss rate is low enough for the coherent interaction with single spins. In order to generate a large ZPF ( $V_{\text{ZPF}} \propto \sqrt{Z_c}$ ), we study high impedance superconducting microwave resonators with a characteristic impedance up to  $4\text{ k}\Omega$ . Moreover for hybrid circuit QED experiments with spins, it is essential that the resonators are magnetic field resilient.

In this chapter, we therefore focus on the characterization of the superconducting resonators designed and fabricated following the process described in the previous chapter. We first measure simple CPW resonators made on Si wafer with a thin layer of thermally grown  $\text{SiO}_2$  to evaluate the quality factors at zero magnetic field and in the in-plane and out-of-plane magnetic fields. We then repeat

the measurement for identical resonators fabricated on the Si-MOS wafer with nanowire devices to assess the influence of a complex substrate structure on the resonators' figures of merit. Then we reiterate the measurement for resonators with DC bias lines, which are necessary to control the quantum dots, to simulate the circuit QED architecture and extract the quality factors.

## 3.1 NbN superconducting resonators characterizations on Si substrates

In this section, we characterize the NbN CPW resonators fabricated on a p-type silicon wafers ( $1\text{-}15\ \Omega\text{cm}$ ) with  $400 \pm 80\ \text{nm}$  of thermally grown  $\text{SiO}_2$ . Note that the same wafers were used to characterize the NbN films. We extract by RF measurement the quality factors and resonance frequencies of the resonators with different characteristic impedances at zero and finite magnetic fields.

### 3.1.1 Basic characterization

From the  $10\ \text{nm}$  thick NbN layer characterized previously with a kinetic inductance of  $192\ \text{pH}\ \square^{-1}$ , we have designed three sets of resonators with impedances of  $110\ \Omega$ ,  $890\ \Omega$  and  $4.1\ \text{k}\Omega$  by just varying the central conductor width  $w$  from  $50\ \mu\text{m}$  to  $200\ \text{nm}$  while keeping the gap width to  $s = 2\ \mu\text{m}$ , see Tab. 3.1. The characteristic impedance is derived using the formulas given in Sec. 1.1.2.

$Z_c$	$110\ \Omega$	$890\ \Omega$	$4.1\ \text{k}\Omega$
$w\ (\mu\text{m})$	50	2	0.2
$s\ (\mu\text{m})$	2	2	2

Table 3.1 – Characteristic impedance of the resonators with different geometries

Representative scanning electron microscopy (SEM) images of the resonators of different characteristic impedances are shown in Fig. 3.1.(a). All the resonators are resonating at a similar frequency, however they have very different lengths meaning that the electric field mode volume is very small for the high-impedance resonators. We designed arrays of resonators in a hanger type geometry coupled to a  $50\ \Omega$  feedline (see Fig. 3.1.(b)), this allows parallel measurements of several resonators in one experimental run. Note that the results shown in this section are performed using an RF tight sample box (see Fig. 3.1(c)) such that the resonators chip is isolated from any microwave radiation. Measurements have been carried out in the dilution fridge described in Sec. 2.4 at  $T_{\text{base}} \approx 8\ \text{mK}$ .

A typical normalized transmission spectrum is shown in Fig. 3.2(a). The transmission spectrum is normalized by setting the background signal to  $0\ \text{dB}$  and by removing the electronic delay and phase shift of the measurement set-up. Once

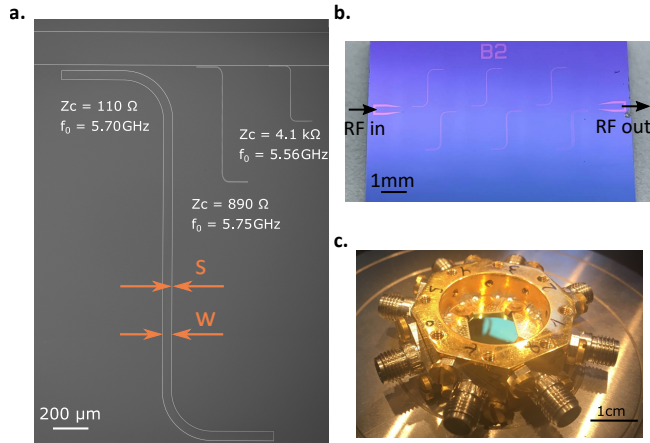


Figure 3.1 – Experimental implementation for the resonators characterization. (a) Three combined SEM images of the NbN CPW resonators with different central conductor widths  $w$  and a same gap width of  $s = 2 \mu\text{m}$ . Despite the length difference, all three resonators resonate around the same frequency. The orientation of the in-plane and out-of-plane fields is also indicated. (b) Photograph of a resonators chip with six resonators capacitively coupled to a  $50 \Omega$  transmission line called the feedline. (c) Image of a chip bonded inside an RF tight sample holder.

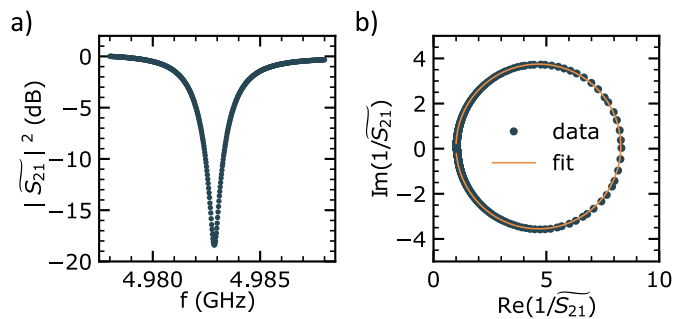


Figure 3.2 – Normalized transmission spectrum of a resonator. (a) Typical normalized  $\widetilde{S}_{21}$  response of a resonator in the many photons regime. (b) Parametric plot (dot) and fit (line) of  $\text{Im}(1/\widetilde{S}_{21})$  vs  $\text{Re}(1/\widetilde{S}_{21})$  (dots) of the same data as in (a).

normalized and close to resonance, the  $\widetilde{S}_{21}$  coefficient can be described by [94]

$$\frac{1}{\widetilde{S}_{21}} = 1 + \frac{Q_i}{Q_c} e^{i\phi} \frac{1}{1 + i2Q_i\delta x}, \quad (3.1)$$

where  $Q_i$ ,  $Q_c$  are the internal and coupling quality factor respectively,  $\phi$  is the rotation in the  $1/\widetilde{S}_{21}$  complex plane due to an impedance mismatch between the feedline and the resonators and  $\delta x = (f - f_0)/f_0$  is the relative frequency to the resonance frequency  $f_0$ . The fit is performed in the  $1/\widetilde{S}_{21}$  complex plane to take into account the resonance response in magnitude and in phase simultaneously. A typical result of such a fit is shown in Fig. 3.2(b). From this fit, we extract the resonance frequency and the quality factors  $Q_i$  and  $Q_c$ .

### 3.1.2 Power dependence

As we want to observe coherent interaction between a single photon and a hole spin, we decrease the input power of the resonators to reach the single photon limit. From a circuit model we derive the average photon number inside the resonator as a function of the input power

$$\langle n_{\text{ph}} \rangle = \frac{Q_c}{\omega_0} \left( \frac{Q_i}{Q_i + Q_c} \right)^2 \frac{P_{\text{in}}}{\hbar\omega_0}, \quad (3.2)$$

where  $P_{\text{in}}$  is the input power and  $\omega_0 = 2\pi f_0$ . We then measure the quality factors of the resonators as a function of the average photon number. The full derivation of  $\langle n_{\text{ph}} \rangle$  can be found in Appendix D.

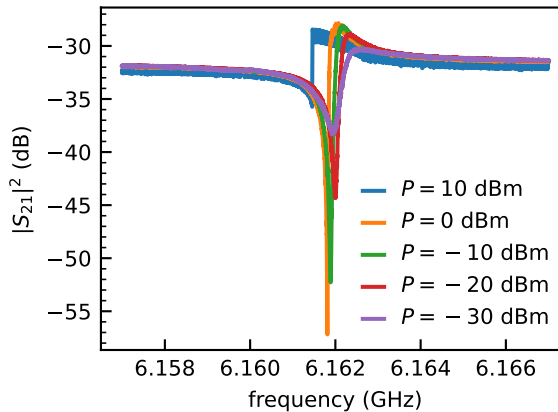


Figure 3.3 – Transmission amplitude of a 4.1 k $\Omega$  resonator around its resonance frequency at different output powers of the VNA. There is a clear resonance frequency shift towards lower frequencies when increasing the power applied to the resonator. At high powers, the resonance also becomes asymmetric due to the non-linear response of the NbN film.

Fig. 3.3 shows the resonance response of a high-impedance resonator at different VNA output powers from 10 dBm to  $-30$  dBm. The resonance becomes asymmetric at high powers and shifts towards lower frequencies, which can be explained by the non linearities in the NbN films [1].

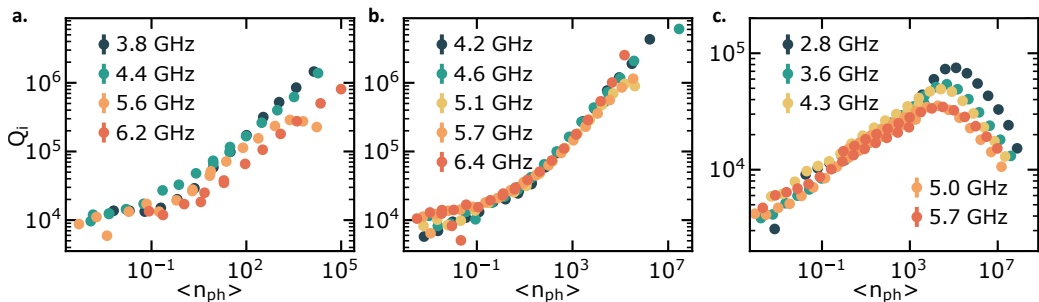


Figure 3.4 – Power dependence of the resonators' internal quality factors. (a)  $Q_i$  as a function of  $\langle n_{\text{ph}} \rangle$  for the 4.1 kΩ resonators with different resonance frequencies. (b)  $Q_i$  as a function of  $\langle n_{\text{ph}} \rangle$  for the 890 Ω resonators. (c)  $Q_i$  as a function of  $\langle n_{\text{ph}} \rangle$  for the 110 Ω resonators.

Thereafter we translate the output power of the VNA to the average number of photons using Eq. (3.2). We then extract the internal quality factors of the resonators as a function of photon number for each impedance, see Fig. 3.4.

Before going into detail we precise that the 110 Ω resonators stayed in ambient atmosphere for a few months during the COVID-19 pandemic shutdown between its fabrication and the characterization. This may explain its different behaviour from the two other sets of resonators, which were protected by a layer of photoresist.

For the 900 Ω and 4.5 kΩ resonators, we observe a clear saturation of the internal quality factor at low power that may be explained by two-level system dynamics [25]. While at high photon number,  $\langle n_{\text{ph}} \rangle > 10^5$ , and for the same set of resonators, self-Kerr non-linearities lead to a strong asymmetry of the measured resonances rendering the analysis of the quality factors beyond the scope of our study.

For the 110 Ω resonators, we do not observe a saturation in the single photon regime. At high power,  $Q_i$  reaches a maximum value around  $\sim 10^4$  photons and then decreases with a further increase in photon number. We do not have any clear explanation of this behaviour at high power, we only suspect that the NbN film suffered from staying in ambient atmosphere.

The internal quality factors remain above  $10^4$  for all the resonators in the single photon limit at zero magnetic field. This is very encouraging for the future circuit QED experiment even if the co-integration of the resonator on the silicon nanowire chip will increase the microwave losses as we will discuss in Sec. 3.2.

Meanwhile, the external quality factor  $Q_c$  is mostly geometry dependent, therefore it is constant as a function of photon number, see Fig. 3.5 for the 4.1 kΩ

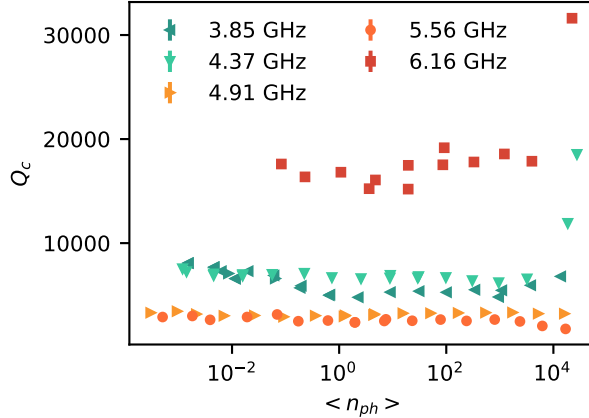


Figure 3.5 – Power dependence of the external quality factor for the 4.1 k $\Omega$  resonators.  $Q_c$  is constant except at very high power when the resonance becomes non linear.

resonators. Note that  $Q_c$  is of the orders of  $10^4$ , which is comparable with  $Q_i$  in the single photon regime and it corresponds to the good ratio between  $Q_c$  and  $Q_i$ . Indeed, to maximize the readout signal, we do not want to be in the under-coupled regime where  $Q_c \gg Q_i$  but in the over-coupled regime with  $Q_c < Q_i$  [117].

### 3.1.3 Magnetic fields resilience

We now turn to the behaviour of the resonators in a static magnetic field. The internal quality factor and the relative frequency shift as a function of the applied magnetic field have been measured with an average of  $\approx 100$  photons and the results can be seen in Fig. 3.6. For an out-of-plane magnetic field, see Fig. 3.6.(a) and (b), the internal quality factor drops to  $10^2$  at 100 mT with an abrupt jump in resonance frequency around 0 T for the 110  $\Omega$  and 890  $\Omega$  resonators. For the narrowest resonators (4.1 k $\Omega$ )  $Q_i$  stays well above  $10^4$  up to  $B_{\perp} = 300$  mT without any jump or hysteresis in the resonance frequency. We note a dip in  $Q_i$  around  $\sim 150$  mT, which can be associated with a coupling of the resonator to magnetic impurities. The quadratic shift of the resonance is explained by the superconducting depairing under magnetic field and can be fitted following the expression [123]  $\Delta f/f_0 = -(\pi/48)[De^2/(\hbar k_B T_c)]B_{\perp}^2 s^2$  with  $D$  the electronic diffusion constant. The extracted diffusion constant  $D \approx 0.58$  cm<sup>2</sup>/s is consistent with previous measurements [42, 75] on NbN thin films.

For the in-plane magnetic field resilience, see Fig. 3.6.(c) and (d), we find  $Q_i > 10^4$  for all resonators from 500 mT to 6 T. Finally, both out-of-plane and in-plane magnetic field studies show that the highest impedance resonators have also the highest magnetic field resilience. As the losses induced in a magnetic field are mainly attributed to the creation of magnetic-flux vortices in the supercon-

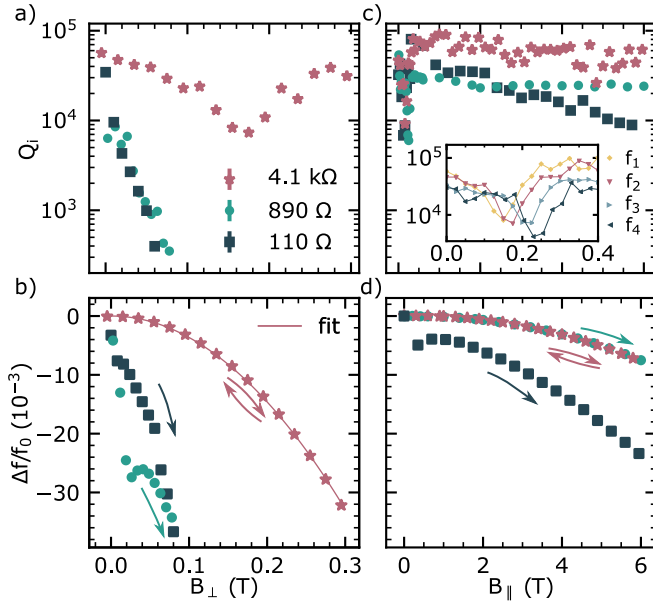


Figure 3.6 – Evolution of the resonators characteristics with a magnetic field. (a)  $Q_i$  as a function of  $B_{\perp}$ . (b) Normalized shift of the resonance frequencies with  $B_{\perp}$  where the lower impedance resonators show abrupt jumps around zero field while the highest impedance resonator shows no abrupt jumps and no hysteresis. (c)  $Q_i$  as a function of  $B_{\parallel}$  for different impedances. For the resonators at  $110 \Omega$  and  $4.1 \text{ k}\Omega$ , the measurement is performed from 0 to  $-6 \text{ T}$  and for practical reasons it is plotted as positive values. At low magnetic field, the dip in  $Q_i$  is due to coupling to magnetic impurities. Inset:  $Q_i$  as a function of  $B_{\parallel}$  around 200 mT for  $Z_c = 4.1 \text{ k}\Omega$  resonators resonating at different frequencies ( $f_1 = 3.8 \text{ GHz}$ ,  $f_2 = 4.4 \text{ GHz}$ ,  $f_3 = 5.6 \text{ GHz}$ ,  $f_4 = 6.2 \text{ GHz}$ ) all coupled to magnetic impurities of  $g = 2$ . (d) Normalized shift of the resonance frequencies with  $B_{\parallel}$ . Arrows in (b) and (d) indicate the sweep direction of the magnetic field.



ducting film, a smaller width of the central conductor minimizes vortices creation and dynamics, thus suppressing the quality factor degradation. For the 4.1 k $\Omega$  resonator for example, the central conductor width (200 nm) is shorter than the London penetration depth of thin NbN films [72]. Therefore, vortices are induced only in the ground plane[80], which explains its high  $Q_i$  in magnetic fields. The relative resonance shift in  $B_{\parallel}$  in Fig. 3.6.(d) shows that the 110  $\Omega$  resonances jump abruptly around 0 T, which is a signature of instable magnetic-flux vortices in the superconducting film, while the 890  $\Omega$  and the 4.1 k $\Omega$  resonators show smooth shift of the resonance frequency and no hysteretic behaviour.

Concerning the interaction between the resonator and magnetic impurities, the inset in Fig. 3.6.(c) shows the internal quality factors of four 4.1 k $\Omega$  resonators with different resonance frequencies. The observed dip in the internal quality factor is shifting to a higher magnetic field as the resonator frequency is increased as expected for the resonant condition  $g\mu_B B = \hbar\omega_0$  with  $g$  the Landé g-factor of the magnetic impurities. From all resonators measurements, we extract  $g = 1.97 \pm 0.29$ , which matches the g-factor of free electrons ( $g = 2$ ).

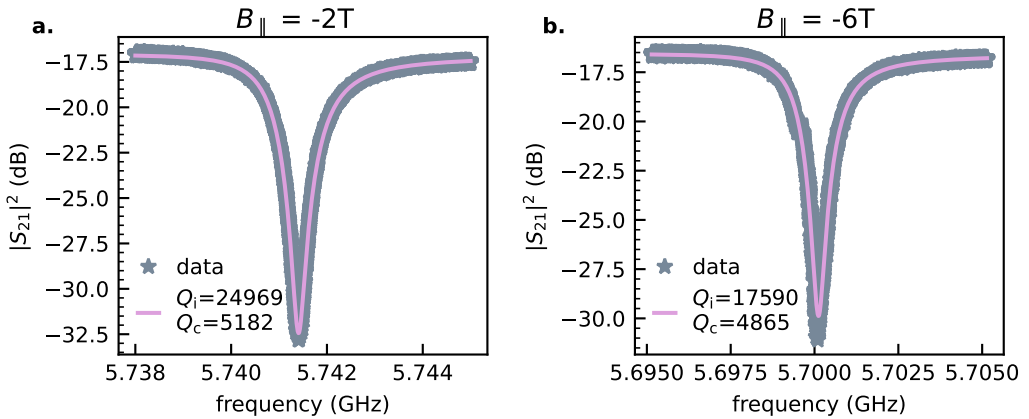


Figure 3.7 – Resonance of a 4.1 k $\Omega$  resonator in the single photon regime at finite in-plane magnetic field. (a) Resonance characterized with  $-2$  T in-plane magnetic field with  $Q_i = 24969$ . The input power at the resonator is  $-140$  dBm corresponding to 0.25 photon on average. (b) Resonance characterized with  $-6$  T in-plane magnetic field with  $Q_i = 17590$ . The input power at the resonator is  $-140$  dBm corresponding to 0.22 photon on average.

Thus, even without complex microwave engineering to minimize vortices dynamics, narrowing down the central conductor width of a CPW design from  $2 \mu\text{m}$  to 200 nm already improves the magnetic resilience by several orders of magnitude for both in-plane and out-of-plane magnetic field. In addition, we have verified that the excellent behaviour under a magnetic field of  $B_{\parallel} = 6$  T with  $Q_i > 10^4$  is preserved in the single photon regime for the 4.1 k $\Omega$  resonators, see Fig. 3.7. These results are very promising for the circuit QED experiments operating at

finite magnetic fields.

## 3.2 Extra microwave challenges in the cQED geometry

The high quality factors high-impedance resonators are the first step towards the hybrid Si QD-cavity system. However integrating the resonators on the Si QD wafer will undeniably degrade the quality of the resonators as the substrate is composed of several metallic layers buried under a SiO<sub>2</sub> layer grown by PECVD, which has a much higher surface roughness [5] and a larger loss tangent [109] than the thermally grown SiO<sub>2</sub>. To incorporate the nanowire transistor in the circuitry, extra bias lines have to be included on the chip as well as a DC tap in the resonator, which may become a source of photon loss and degrade the quality factors. In this section, we assess step by step the quality factors of the resonators in the circuit QED architecture and try to mitigate the microwave losses.

### 3.2.1 Influence of the substrate

First of all, the substrate on which the resonators will be fabricated is much more complex than the Si/SiO<sub>2</sub> wafers used in Sec. 3.1. Fig. 3.8.(a) shows the optical microscope image of a NbN resonator on a chip provided by LETI with the transistors. The resonator follows the same design and fabrication steps as the 110Ω resonators of Sec. 3.1 with  $w = 50\ \mu\text{m}$  and  $s = 2\ \mu\text{m}$ . On the microscope image, the transistors are too small to be seen but we can distinguish the dummy structures which are everywhere except the square bond pads regions, more details about the transistors chip can be found in Sec. 2.1.

Fig. 3.8.(b) shows the internal quality factor of such a resonator with a resonance frequency of 4.5 GHz as a function of the average photon number. The geometry of this resonator is exactly the same than the one resonating at 4.3 GHz on the silicon wafer. So the resonance frequency does not shift considerably but it surprisingly shifts towards higher frequencies. Indeed, we expect the resonance frequency to shift down due to additional capacitance brought by the metallic compounds in the wafer.

In contrast with the data from Sec. 3.1, here the internal quality factor clearly saturates at the single photon regime for  $Q_i \approx 1000$ . However even at high input powers, the quality factor  $Q_i$  never exceeds  $8 \cdot 10^3$ . Hence, the quality factors decrease from  $10^4$  to 1000 either due to the several metallic layers in the wafer interfering with the microwave behaviour of the resonator or due to the silicon oxide layer grown by PCVD rather than a thermal growth. Indeed the microwave dielectric loss is one order of magnitude higher for the deposited SiO<sub>2</sub> than thermal SiO<sub>2</sub> [109, 93]. Nevertheless,  $Q_i$  remains in the acceptable value range, with a photon loss rate of  $\kappa_{\text{int}}/2\pi = 4.5\ \text{MHz}$ , to proceed with the cQED architecture.

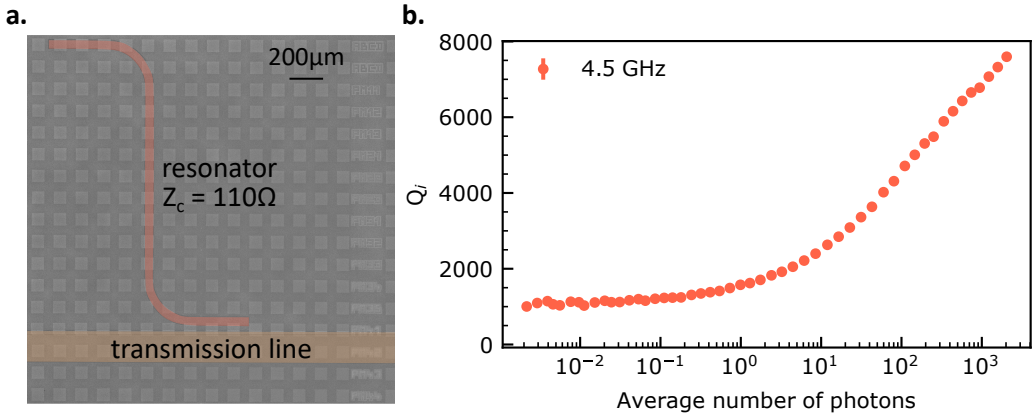


Figure 3.8 – Resonator characterization on a Si-MOS chip. (a) Colorized optical microscope image of a  $110\ \Omega$  NbN CPW resonator fabricated on the CMOS wafer with the transistors below. The geometry of the CPW is identical to the  $110\ \Omega$  resonators presented in Sec. 3.1. (b) Internal quality factor of the resonator as a function of the average number of photons. In the single photon regime,  $Q_i \approx 1000$  and  $Q_i < 8 \cdot 10^3$  at high powers while the same resonators on silicon wafers reach  $Q_i > 2 \cdot 10^4$ .

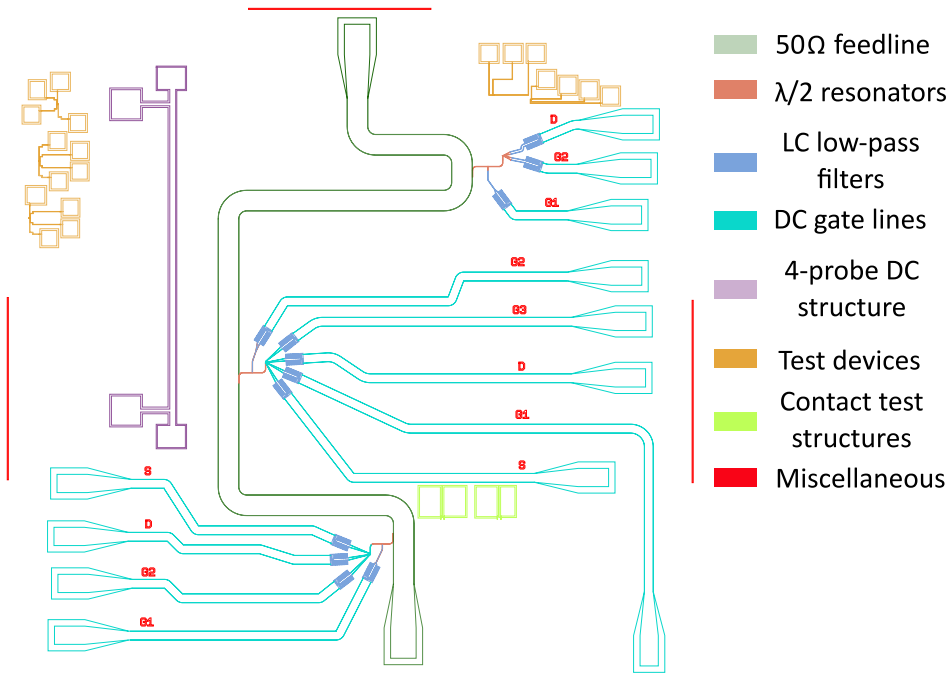


Figure 3.9 – Hybrid Si QD-cavity system design in the cQED architecture with three sets of resonator each connected to a quantum dot.

### 3.2.2 Microwave leakage due to additional gate lines

When the resonators are connected to the quantum dots, many DC bias lines come into play as each gate of the QD has to be voltage biased. A typical chip design for the coupled system is shown in Fig. 3.9. The hanger geometry of the resonators enables the simultaneous fabrication of several hybrid circuit QED devices per chip, thus usually three resonators are coupled to three different transistors. The resonator is usually connected to one of the gate of the transistor and a DC tap is placed at the middle of the resonator at the voltage node to bias the concerned gate. Each of the DC lines are filtered by a lumped LC low-pass circuit that we will describe in the next paragraph. At the early stages of the characterization, we insert on the  $1 \times 1 \text{ cm}^2$  chip different test structures such that four-probe DC structure for the resistivity measurement of the NbN film or structures to test the contact to the devices for instance.

#### On-chip LC filters

To minimize microwave leakages, we add an LC filter to each dc bias line. In contrast to the resonator, the LC filter is made of a lumped element inductance and capacitance. The design of the LC filters are very much inspired by the works of [97] and [62]. The capacitance is made from a long interdigitated capacitor with a capacitance to ground of  $0.134 \text{ pF}$  at  $1.5 \text{ GHz}$ . The inductance is a thin nanowire of  $123 \text{ nH}$ , which is  $320 \text{ }\mu\text{m}$  long and  $500 \text{ nm}$  wide. Fig. 3.10 shows the SEM image of such a filter with its dimensions. Both components are patterned at the same time than the superconducting resonator on the same NbN film.

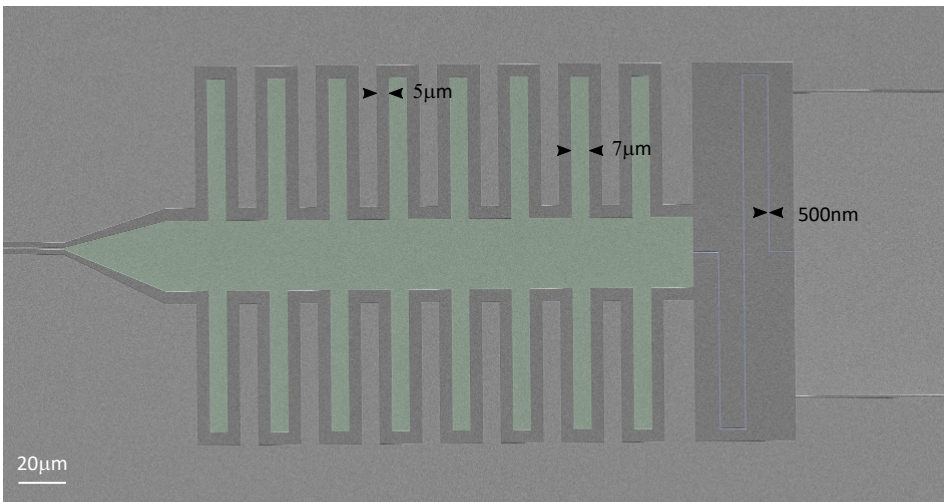


Figure 3.10 – Colourized SEM image of a LC low-pass filter with a cut-off frequency of  $1.2 \text{ GHz}$ . The interdigitated capacitance is colourized in green and the nanowire inductance is in blue.

The capacitance value has been calculated by Sonnet simulation. The cut-off

frequency of this LC filter is then  $f_{\text{cut-off}} = 1/2\pi\sqrt{LC} = 1.2 \text{ GHz}$ . The footprint of each filter is  $300 \times 400 \mu\text{m}^2$ , which is not negligible and it is difficult to place more than five filters around the same transistor as shown in Fig. 3.9. To overcome the size issue, in future designs we can consider a thin film capacitance on top of the NbN layer as demonstrated in [62], which needs more fabrication developments.

### Quarter-wave transformer

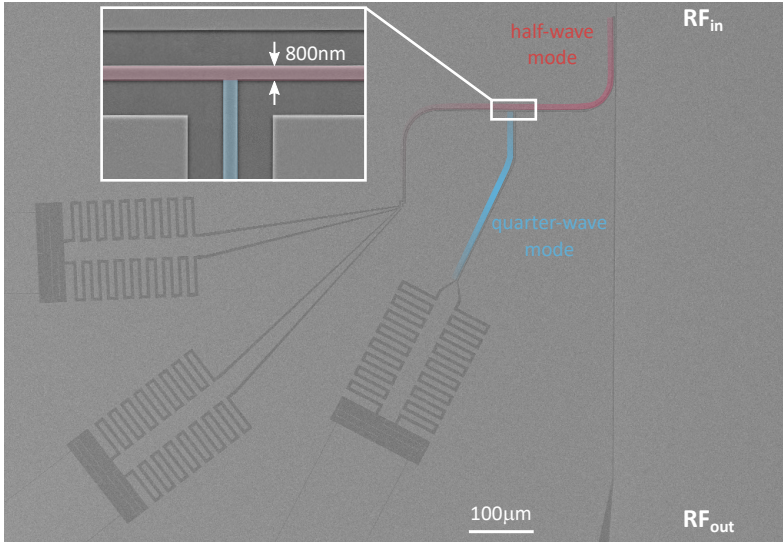


Figure 3.11 – Quarter-wave transformer at the resonator voltage node point in addition of the LC filter.

In order to mitigate the microwave losses, we also add a quarter-wave transformer at the DC tap of the cavity before the interdigitated capacitance [27], see Fig. 3.11, which forms a T-shape with the half-wavelength cavity. As the quarter-wave mode is terminated, by the capacitor, in an open circuit  $Z_L = \infty$ , then the input impedance is given by [117]

$$Z_{\text{in}} = \frac{Z_c^2}{Z_L}, \quad (3.3)$$

with  $Z_c$  the impedance of the coplanar waveguide, therefore  $Z_{\text{in}} = 0$ . Hence, when the microwave approaches the dc tap, at the voltage antinode, it will see a short ( $\lambda/4$  line) and a high-impedance line ( $\lambda/2$  line) and will go to the latter one. The quarter-wave transformer is then a second barrier to the microwave photons in addition of the LC low pass filter.

### Ground plane definition

The additional gate lines cut the ground planes around the resonators and perturb their microwave behaviour, which can be prevented by add wirebonds

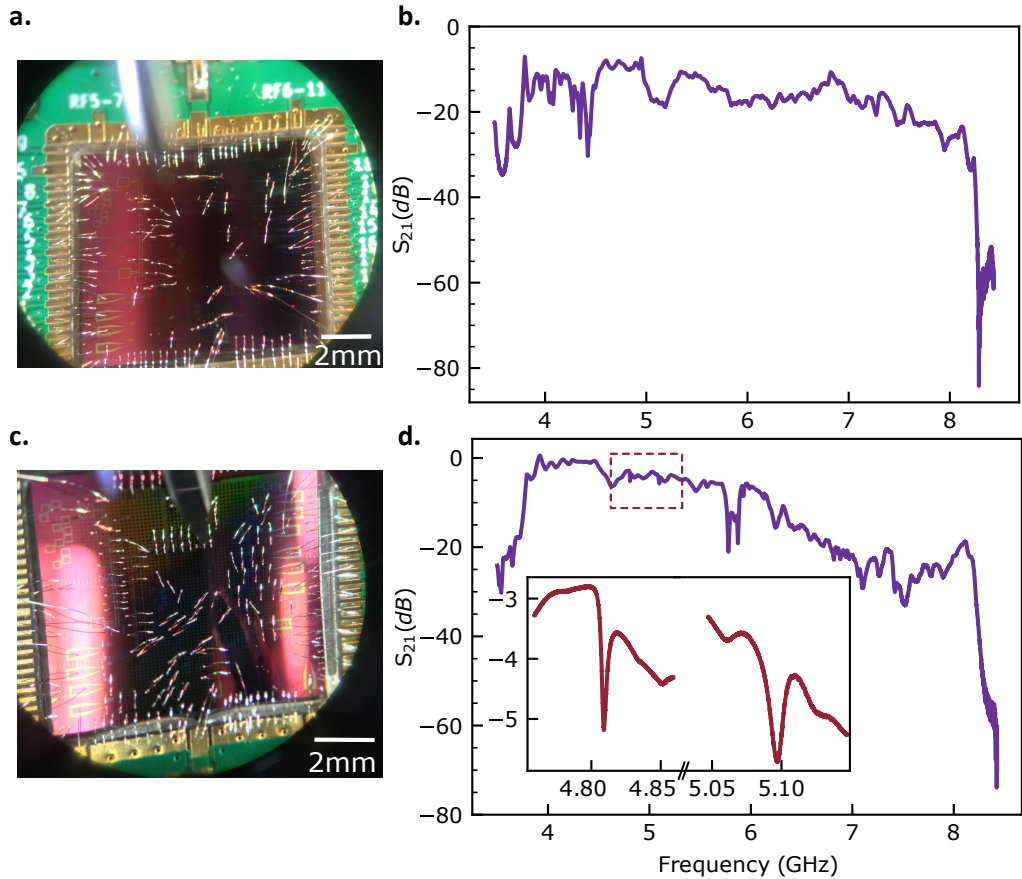


Figure 3.12 – Microwave resonances dependence on the ground plane definition. (a) A chip with few bonds connecting the ground plane around the resonators. (b) The transmission response of the chip shown in (a) at 8 mK with no apparent resonance. (c) A twin chip of the one shown in (a) with more bonds around the resonators. (d) The transmission response of the chip shown in (c) with two resonances spotted in the red dotted region. The inset shows the transmission response of the resonances.

connecting the ground planes. Indeed, due to the large kinetic inductance of the NbN film, the metallic planes near the resonators can behave as inductors if they are not well connected to the ground. Asymmetries in microwave circuitries can also lead to the excitation of parasitic slotline modes [116] which can be a source of loss for the microwave photon. Fig. 3.12 shows the transmission spectrum of two chip with the exact same design and fabrication of three resonators connected to a transistor but with a different number of wirebonds around the ground plane. In the case with a few wirebonds connecting the different ground planes, the transmission spectrum shows zero resonance. With a larger number of wirebonds, the resonances appear meaning that the photon loss has been reduced. To even further improve the quality of the resonances, we can switch from wirebonds to air-bridges [116, 2, 28], which would attenuate the slotline modes propagation two orders of magnitude more effective than wirebonds [28]. However it would add two more lithography steps, thus in this work we kept the wirebonding technique for simplicity.

Using the wirebonding surgery, in the complete circuit QED geometry, the quality factors of the resonators drop to a few hundreds with a photon loss rate of  $\kappa/2 \sim 10$  MHz. Even though a lot of photons have been lost from the bare CPW resonators on silicon wafers with  $Q_i \sim 10^4$  to the coupled resonator, the coupling rate should still be higher than the photon rate so coherent interactions are still possible.

**TAKEAWAY MESSAGES:**

- The characteristic impedance of a CPW resonator can be tuned by changing the ratio of center conductor and gap widths.
- On silicon/silicon oxide substrate, the internal quality factors are above  $10^4$  in the single photon regime at zero magnetic field.
- Narrowing the central conductor width helps to increase the magnetic resilience for both in-plane and out-of-plane magnetic fields.
- The high-impedance resonators feature  $Q_i > 10^4$  at finite in-plane magnetic field, in the single photon regime.
- The resonators quality factors are degraded by the substrate with the transistors but remain above  $10^3$  in the single photon regime.
- The additional lines to voltage bias the quantum dots need to be low-pass filtered to prevent from microwave leakage of the photons.
- Wirebonding surgery of the ground plane around the transmission lines is primordial for clean microwave properties.
- In the single photon regime, from the bare CPW resonators to the coupled resonators on the transistors wafer,  $Q_i$  drops from  $10^4$  to a few hundreds.





# Chapter 4

## DISPERSIVE COUPLING OF A SINGLE HOLE TO A SINGLE PHOTON

### Contents

<b>4.1</b>	<b>Characterisation of the hybrid system . . . . .</b>	<b>73</b>
4.1.1	Nanowire transistor characterization . . . . .	73
4.1.2	Superconducting resonator characterization . . . . .	74
<b>4.2</b>	<b>Charge-photon interaction . . . . .</b>	<b>76</b>
4.2.1	Characterisation of a double quantum dot . . . . .	76
4.2.2	Dispersive charge/photon strong coupling . . . . .	79

**N**ow that the preliminary study of superconducting resonators is done, we can start the circuit QED experiment with a nanowire transistor embedded in the NbN superconducting resonator. In what follows, the measurements are carried out with a high-impedance superconducting resonator galvanically connected to a 4-gate silicon nanowire transistor. The characteristic impedance of the resonator is  $2.5\text{ k}\Omega$  given by  $w = 800\text{ nm}$  and  $s = 2\text{ }\mu\text{m}$ . The dimensions of the transistor are summarized in [Table 4.1](#). The two outer gates (G1 and G4) of the transistor are shorted together in order to reduce the number of lines on the chip and the resonator is connected to the gate G2. SEM images of the hybrid device are shown in [Fig. 4.1](#).

In this chapter, we first show the transport measurement of the transistor at room temperature and at 8 mK, and the resonator's response when it is decoupled from the transistor. Then we report the microwave cavity read-out of the quantum dots formed in the nanowire channel. We conclude the chapter with the charge-photon interaction of a single hole with a microwave photon.



Table 4.1 – Device characteristics and dimensions

Contacts	p-doping
Number of gates	4
Channel width	40 nm
Channel height	13 nm
Gate length	40 nm
Gate spacing	40 nm

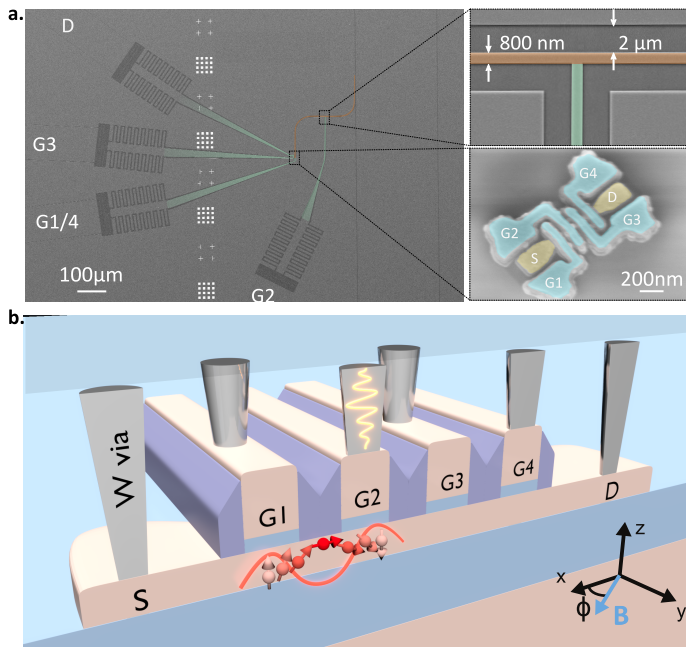


Figure 4.1 – Hybrid device with four-gate nanowire transistor embedded in a high-impedance NbN cavity. (a) False-colour SEM image of the high-impedance resonator (orange) with the DC fanout lines (green) with LC filters. The top left inset gives the dimensions of the resonator. The bottom left inset shows the false-colour SEM image of a four-gate nanowire transistor, the source and drain are in yellow while the gates are in blue. The resonator is galvanically connected to the gate electrode G2. (b) Artistic 3D representation of the four-gate nanowire transistor with tungsten vias ensuring the electrical connection between the gate electrodes and the cavity. The wavepacket in the via connected to G2 represents the link to the microwave cavity, while a double quantum dot potential is formed below G1 and G2.

## 4.1 Characterisation of the hybrid system

Before measuring the charge-photon interaction, we first perform the individual characterisation of the transistor and the superconducting resonator. We briefly report the hole transistor characteristics at room temperature and at 8 mK. We also characterise the photon loss of the cavity.

### 4.1.1 Nanowire transistor characterization

We start by the room temperature transport measurements of the transistor to check that we have electrical contact to all the gates and a current passes through the channel. The IV characteristics of the four-gate device is displayed in Fig. 4.2 with a bias voltage of  $V_{SD} = 50$  mV and the gates, which are not swept, are set at  $-2$  V to be fully open.

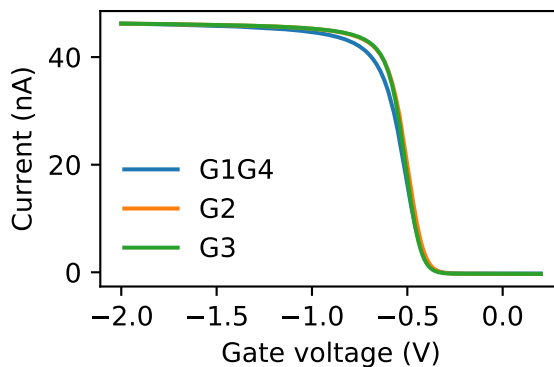


Figure 4.2 – Transport measurement of all the gates at room temperature. The bias voltage is set at 50 mV and we sweep gate per gate while applying  $-2$  V to the gates in series that are not swept. The gates G2 and G3 have exactly the same IV characteristics while G1/G4 shows a slightly different one due to the fact that two gates are swept simultaneously. The saturation of the current is due to the resistance of the RC filters on the PCB.

From the IV curve of the transistor, we can extract a threshold voltage of 320 mV for all the gates. This small spread of the threshold voltage indicates a good sample uniformity. Then we measure a subthreshold slope of  $\approx 150$  mV/dec. The theoretical ideal subthreshold slope is  $\ln(10)k_B T/e = 60$  mV/dec at 300 K known as the thermionic limit [134] such that the transistor has a fast on/off switch control on the current through the channel. Yet, we are not at the limit of the perfect transistor, however all the gate electrodes are acting on the channel and follow the same IV characteristics, so we can now cool it down to 7 mK.

The sample is now at 8 mK in the Bluefors dilution refrigerator with the measurement set-up described in Sec. 2.4. We measure again the current through the nanowire. At high bias voltage,  $V_{SD} = 50$  mV, the IV characteristics of the gates

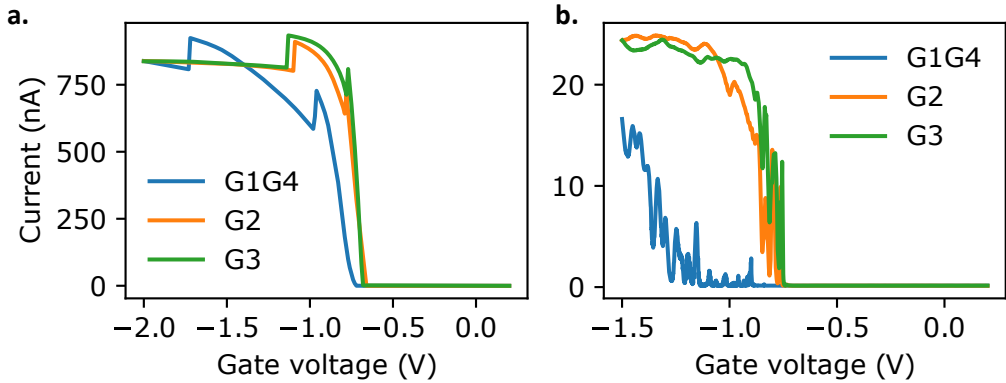


Figure 4.3 – Transport measurement of the 4-gates transistor at 8 mK. a) The bias voltage is set at 50 mV and we sweep gate per gate while applying  $-2$  V to the gates that are not swept. b) The bias voltage is lowered to 1 mV and the Coulomb peaks appear. The gates G2 and G3 have a similar behaviour as at room temperature while G1/G4 shows a different behaviour.

are similar to the one measured at 300 K with a shift from  $-320$  mV to  $-720$  mV in the threshold voltage. It gives an estimate of the voltage region corresponding to the filling of the first hole below each gate. There are two jumps in current for all the gates, which may come from the measurement apparatus. At low bias voltage,  $V_{SD} = 1$  mV, Coulomb peaks appear in the IV characteristics for the first hole tunneling events. The IV behavior of G1/G4 differs from G2 and G3 probably due to the fact that we sweep two gates simultaneously, and we hence probe two QDs in series at the same time.

### 4.1.2 Superconducting resonator characterization

The superconducting transition of the NbN film is at  $\sim 7$  K so we only characterise the resonators at low temperatures, 8 mK. We start with a broad band transmission measurement from 4 GHz to 8 GHz as shown in Fig. 4.4 in the many photons regime with  $P_{in} = -90$  dBm. There are four resonances in the spectrum at 4.8 GHz, 5.4 GHz, 5.9 GHz and 7.7 GHz. By design, there are three resonators capacitively coupled to the transmission line, which are the three first resonances. The resonance at 7.7 GHz may be an undesired slot-mode on the chip or a harmonic mode of the  $\lambda/4$  resonator associated with the  $\lambda/2$  resonator at 4.8 GHz. Unfortunately even if we probe three resonances, there is only one transistor that is working at base temperature, which is associated with the 5.4 GHz resonance.

We then lower the input power to  $P_{in} = -130$  dBm in order to reach the single photon limit and measure the transmission of the cavity of our interest, which is displayed in Fig. 4.5. Here the gate voltages are set such that no charges move in the DQD. From the resonance fit [51], we can extract the quality factors of the cavity  $Q_i = 529$ ,  $Q_c = 1550$  and the resonance frequency  $f_r = 5.428$  GHz. We

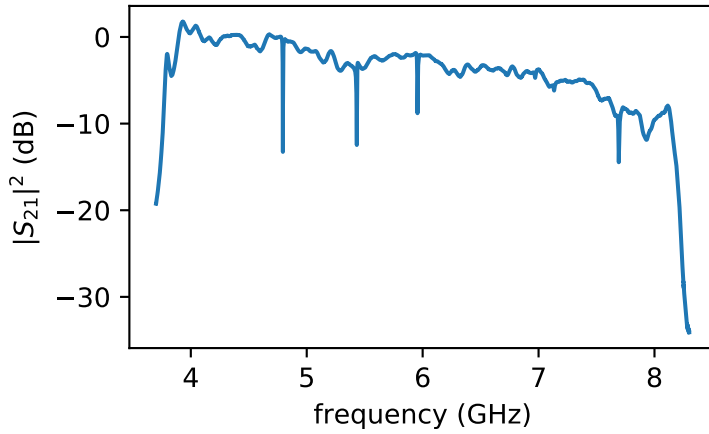


Figure 4.4 – Transmission spectrum of the resonator from 4 GHz to 8 GHz probed with  $P_{\text{in}} = -90$  dBm. Four resonances are visible at 4.8 GHz, 5.4 GHz, 5.9 GHz and 7.7 GHz.

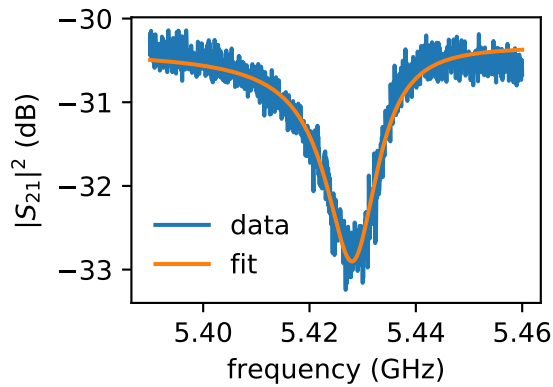


Figure 4.5 – Transmission spectrum of the resonator with less than one photon on average. We extract  $f_r = 5.428$  GHz,  $Q_i = 529$  and  $Q_c = 1550$ .

can then deduce the average number of photons in the cavity, using Eq. (3.2), which is 0.1 photon on average. We could have applied a higher power to the resonator for faster measurements, however 0.1 photon on average still works for the experiment, and we only realize it during the writing of this manuscript. For future experiments, the input power of the cavity can be increased such that the signal to noise ratio can be increased.

The loaded quality factor of the cavity is given by

$$\frac{1}{Q} = \frac{1}{Q_i} + \frac{1}{Q_c}, \quad (4.1)$$

with  $Q = 394$ . We can then calculate the photon loss rates of the cavity

$$(\kappa_i/2\pi, \kappa_c/2\pi, \kappa/2\pi) = (10 \text{ MHz}, 4 \text{ MHz}, 14 \text{ MHz}).$$

The figures of merit of our cavity are similar to the previous work of circuit QED with GaAs DQDs [132] but one order of magnitude larger than cavities used in the previous reports of spin-photon coupling in Si [95, 124]. However, to achieve the strong coupling regime, only one condition has to be fulfilled, namely  $g > \kappa, \gamma$  with  $g$  ( $\gamma$ ) the coupling (decoherence) for either the charge or spin degree of freedom of the single hole. Thus, as long as the coupling rate is greater than 13 MHz, the strong coupling regime is within reach.

## 4.2 Charge-photon interaction

We have assessed the characteristics of the resonator and the transistor separately in the previous section. Now we want to probe the charge tunnelling events in the nanowire with the resonator and demonstrate that we can couple a single hole with a single photonic mode. The measurements shown below are all performed with the source and drain hard grounded on the matrix box.

### 4.2.1 Characterisation of a double quantum dot

The charge-photon coupling experiment is based on the electric-dipole interaction between a single photon and a single hole delocalized in a DQD such that the dipole moment is larger than the one of a single QD. In order to demonstrate the charge-photon interaction, the cavity is driven with a microwave tone at a fixed frequency  $f = f_r$  and the transmitted signal is probed using the VNA as described in Sec. 2.4.

The initial idea about this device is to create a DQD below the gates G2 and G3. Fig. 4.6 shows the cavity transmission amplitude as a function of the plunger gate voltages G2 and G3, with the outer gates G1 and G4 at  $-1 \text{ V}$ . This measurement is performed with an input power of  $P_{\text{in}} = -100 \text{ dBm}$  which is not in the single photon limit to avoid too long measurement times. Each time a hole tunnelling event occurs, there is a shift of the resonance frequency of the cavity

resulting in a increased transmission amplitude, which is featured in yellow on the map. Such a map is called a stability diagram and is described in [Sec. 1.3](#) with the theoretical plots in [Fig. 1.11](#).

As the gate voltages are decreased, the number of holes in the double quantum dots is increased. The almost horizontal lines corresponds to a dot-lead transition with a hole tunnelling from the reservoir to the dot below G2. On the other hand, the vertical lines depict the dot-lead transition to the dot below G3. The 45° short lines are the interdot charge transitions with a hole moving in the double quantum dot, and we only probed a few of them forming a very irregular pattern. In addition, the resonator is hooked up to the gate electrode G2 and senses some additional features, especially in the lower right quarter of the map, which are very blurred and ill defined, these features are maybe due to some metallic dots nearby. We are then not satisfied with this stability diagram.

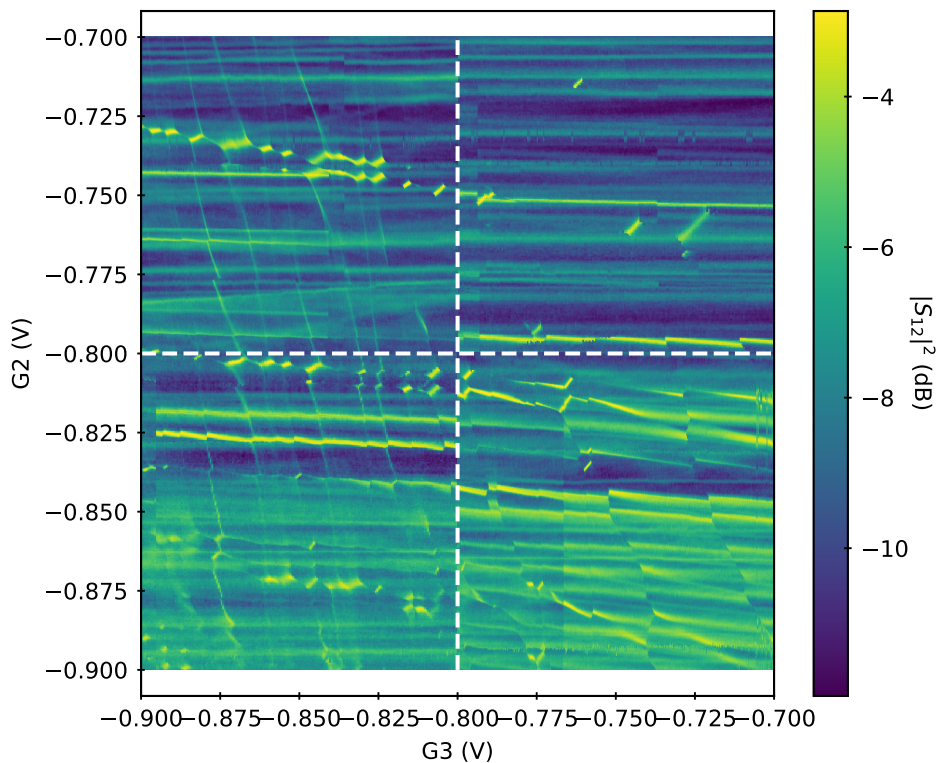


Figure 4.6 – Charge stability diagram as a function of  $V_{g2}$  and  $V_{g3}$  probed by the microwave cavity with  $V_{g1,g4} = -1$  V. The different regions delimited by the white dashed lines are from distinct measurements. The red box highlights the interdot charge transition under investigation in the following.

We then switch to the DQD below G1 and G2, hoping for a honeycomb like stability diagram. [Fig. 4.7](#) shows the transmitted signal as a function of voltages



on G1G4 and G2 while  $V_{g3} = 0$  mV. The background of the stability diagram is more homogeneous and we observe a regular array of interdot charge transitions in the few holes region. There are still lines on G2 which are not interacting with anything, which are probably attributed to metallic dots in the device. Here we observe very few dot-lead transition for two reasons: the dot below G2 is isolated from its reservoir as  $V_{g3} = 0$  mV and the cavity is less sensitive to the dot-lead transition below G1 as it is connected to the gate G2.

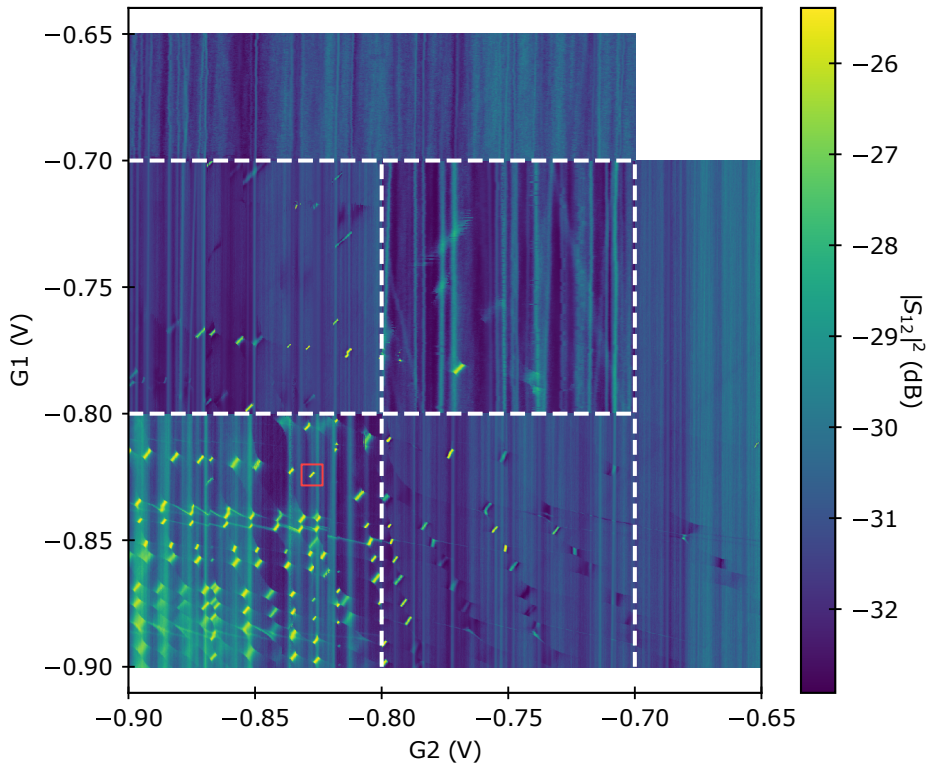


Figure 4.7 – Charge stability diagram as a function of  $V_{g1}$  and  $V_{g2}$  probed by the microwave cavity. The different regions delimited by the white dashed lines are from distinct measurements.

Even though the tunnelling event of the first hole is not probed or identified, we can still work in the few holes region with an odd number of holes accumulated in the DQD such that one hole oscillates between the two dots. The interdot transition focused in the following is highlighted with a red box in Fig. 4.7 with a with a low number of holes in the QD below G1 ( $\sim 4$ ) and G2 ( $\sim 7$ ). It is not the first hole accumulated in the DQD, however this does not affect the dephasing rates of the DQD [12] and it is not unusual to operate in the few charges regime.

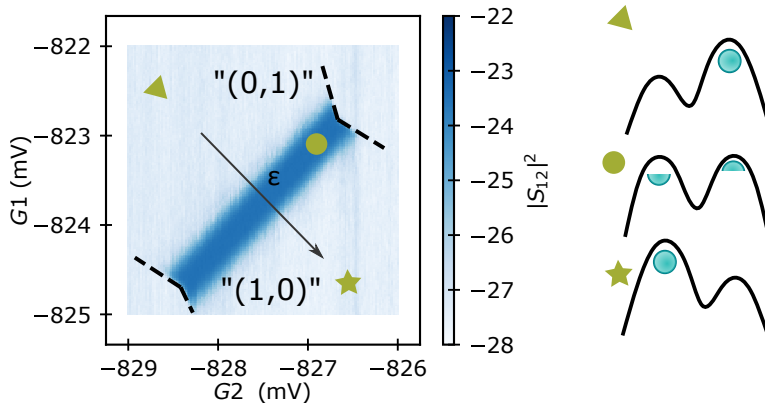


Figure 4.8 – Interdot charge transition with a single hole oscillating in the DQD. The microwave signal is maximum when the hole is delocalized between the two dots.  $\varepsilon$  defines the detuning axis along which the hole moves from the dot under  $G_2$  to the dot under  $G_1$ . At negative detuning, the hole is located below  $G_2$  and at positive detuning, it is below  $G_1$ .

## 4.2.2 Dispersive charge/photon strong coupling

Fig. 4.8 shows the zoom in on the odd number interdot charge transition identified in Fig. 4.7. The dark blue region corresponds to the bias voltages on  $G_1$  and  $G_2$  such that a single hole moves from one dot to the other, leading to a resonance shift of the cavity. We reduce the input power of the cavity to  $P_{\text{in}} = -130$  dBm, corresponding to 0.1 photons on average in the cavity, such that on average only one photon interacts with the hole. We define the detuning axis such that zero detuning between the two dots corresponds to the middle of the interdot charge transition as shown in Fig. 4.8.

To quantify the charge-photon coupling strength, we probe the transmission spectrum of the cavity as a function of the detuning energy of the DQD. We observe a dispersive shift of the resonance frequency of the cavity at  $\varepsilon = 0$  as shown in Fig. 4.9.(a), which depends on the charge-photon coupling  $g_c$  and the tunnelling rate of the DQD  $t_c$ . The down-shift of the resonance response is due to the electric-dipole interaction with the DQD charge qubit with  $\hbar\omega_c = \sqrt{\varepsilon^2 + 4t_c^2} > \hbar\omega_T$  as illustrated in Fig. 4.9.(b).

As we do not know the tunnelling rate of our DQD and there is no gate to tune it, we cannot achieve the resonance condition between the charge qubit and the photon. To overcome this issue, we vary the base temperature of our system. A single hole in a DQD is a charge qubit with a molecular bonding and an antibonding states formed by the hybridization of the left and right states, respectively under  $G_1$  and  $G_2$  as described in Sec. 1.3. The bonding state being the ground state of the qubit, when the temperature increases, the antibonding state gets thermally populated. The dispersive shift of the cavity is then reduced

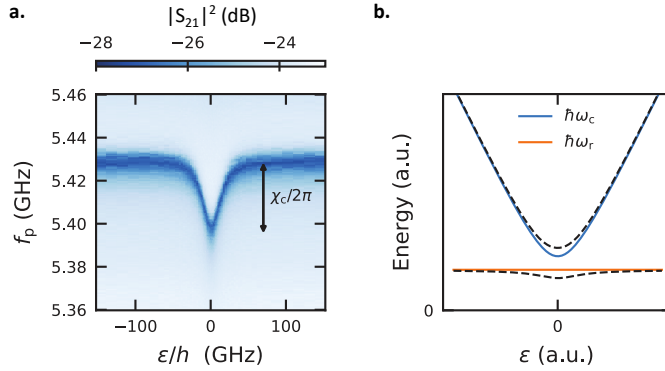


Figure 4.9 – Charge-photon interaction. (a) Transmission through the feed-line as a function of probe frequency and detuning  $\varepsilon$ . At large detuning the bare resonator is probed, whereas near zero detuning the DQD charge qubit interacts dispersively with the resonator leading to a frequency shift  $\chi_c/2\pi$ . (b) Schematic energy diagram of the charge qubit energy and the cavity energy as a function of the DQD detuning for  $\omega_c > \omega_r$ . The coloured solid lines correspond to the non-interacting case while the dashed lines sketch the dispersive repulsion experienced by the cavity and the charge qubit in the presence of a finite charge-photon coupling.

and its variation as a function of temperature follows a Boltzmann distribution for a two-level system. We can therefore extract the charge-photon coupling strength and the tunnelling rate.

Indeed, from the Boltzmann distribution, the probability of the hole being in the excited state is given by

$$p_e = \frac{\exp(-2ht_c/k_B T)}{1 + \exp(-2ht_c/k_B T)}, \quad (4.2)$$

and the probability of being in the ground state is

$$p_g = 1 - p_e, \quad (4.3)$$

with  $h$  the Planck constant and  $k_B$  the Boltzmann constant.

Then the dispersive shift of the resonance frequency of the cavity as a function of temperature and detuning can be written as

$$\chi(T) = g_c^2 d_{01}^2 \left( \frac{1}{2t_c - f_r} + \frac{1}{2t_c + f_r} \right) (p_g - p_e), \quad (4.4)$$

with the bare resonance frequency  $f_r = 5.428$  GHz and  $d_{01}^2 = 2t_c/\sqrt{\varepsilon^2 + 4t_c^2}$  the dipole moment associated with the transition from the ground to excited state. Note that the counter rotating term  $g_c^2/(2t_c + f_r)$  is important as we approach the strong-dispersive regime in this experiment. This term is known as the Bloch-Siegert shift while  $g_c^2/(2t_c - f_r)$  is called the Lamb shift.

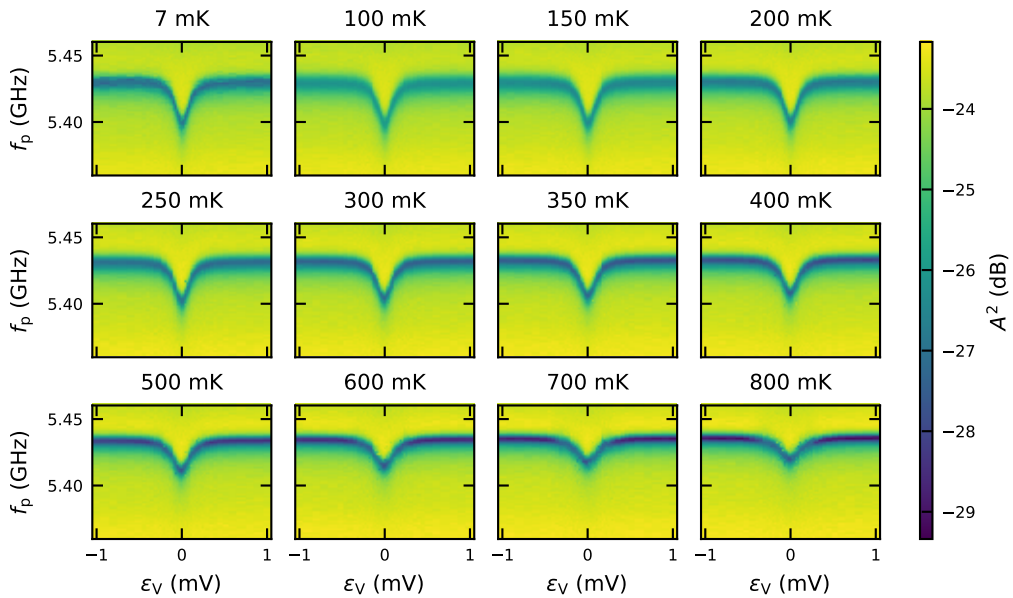


Figure 4.10 – Temperature dependence of the resonance frequency dispersive shift. Transmission as a function of probe frequency  $f_p$  and  $\epsilon$  for various temperatures. At large  $|\epsilon|$  the bare resonator is probed, whereas near  $\epsilon = 0$  the charge qubit interacts dispersively with the resonator, which results in a frequency shift. This shift reduces with increasing temperature due to the larger thermal occupation of the excited state of the charge qubit.

Fig. 4.10 shows the transmission amplitude of the cavity as a function of detuning and probe frequency  $f_p$  at zero magnetic field and at different temperatures. From these measurements, we extract the dispersive shift  $\chi$  at zero detuning, the data are plotted in Fig. 4.11.(a). Fitting the temperature dependence of  $\chi_c/2\pi$  with Eq. (4.4) yields  $g_c/2\pi = 513 \pm 2$  MHz,  $t_c/h = 9.57 \pm 0.61$  GHz and  $\omega_r/2\pi = 5.42835 \pm 0.00006$  GHz. The model matches the data very well.

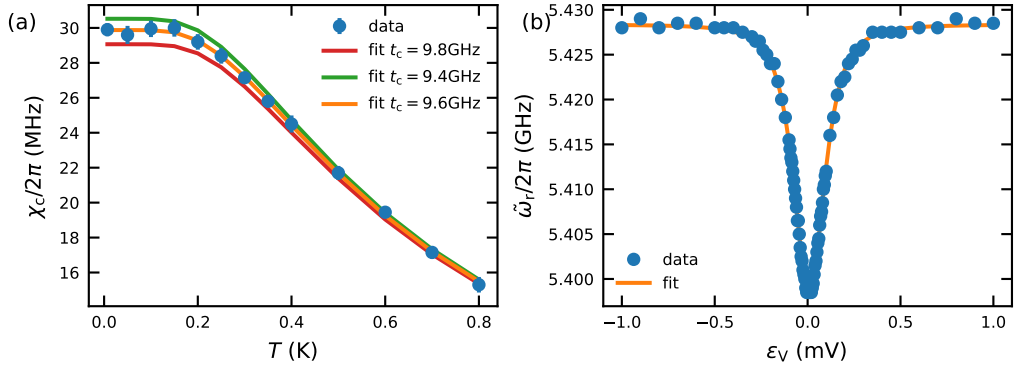


Figure 4.11 – Charge-photon coupling strength and lever arm. (a) Temperature dependence of the resonance frequency dispersive shift. The dispersive shift at  $\varepsilon = 0$  follows a Boltzmann distribution from which we extract  $g_c = 513 \pm 2$  MHz and  $t_c = 9.57 \pm 0.61$  GHz (orange curve). The red and green curves highlight the behaviour difference of the dispersive shift for a 200 MHz change in  $t_c$ . (b) Resonance frequency at base temperature as a function of the detuning. Knowing  $g_c$  and  $t_c$  from (a), we can extract the lever arm  $\alpha$ .

From the detuning dependence of the resonance frequency we can extract the lever-arm,  $\alpha$ , of our device, which is the parameter relating the detuning to the energy difference between the electrochemical potentials of the two dots. To do so, we fit the resonance shift of the cavity as a function of the detuning as follows

$$\chi(\varepsilon) = g_{\text{eff}}^2 \left( \frac{1}{f_q(\varepsilon) - f_r} + \frac{1}{f_q(\varepsilon) + f_r} \right), \quad (4.5)$$

with

$$f_q = \sqrt{(2t_c)^2 + \left( \alpha(\varepsilon - V_0) \frac{e}{h} \right)^2}, \quad (4.6)$$

the charge qubit energy with  $V_0$  the offset in gate voltage and

$$g_{\text{eff}} = g_c \frac{2t_c}{f_q}, \quad (4.7)$$

the effective charge-photon coupling from the Jaynes-Cummings Hamiltonian with  $g_{\text{eff}} = g_c$  at zero detuning.

Fig. 4.11.(b) shows the resonance frequency of the cavity as a function of detuning at 7 mK with the fit from Eq. (4.5) to extract the alpha factor by fixing  $t_c =$

9.6 GHz and  $g_c = 513$  MHz. We obtain a lever-arm of  $\alpha = 0.607 \pm 0.004$  eV V<sup>-1</sup>, which is consistent with previous measurement on similar Si transistors [3, 37]. Such a high value of  $\alpha$  results from the tight electrostatic control by the  $\Omega$ -shaped gates [11] and the thin gate oxide (5 nm). Here  $\alpha$  is the detuning lever-arm which takes into account the action of G1 and G2 defined as  $\alpha = (1/e)\partial\epsilon/\partial\epsilon_V$  where  $\epsilon_V = \beta_1 V_{g1} + \beta_2 V_{g2}$  with  $\beta_1 = 0.68$  and  $\beta_2 = 0.73$  is the detuning axis in gate voltages as drawn in Fig. 4.8. However for the charge-photon coupling, the lever arm involved is the one from G2 on the detuning, then  $\alpha_{g2} = \beta_2\alpha = 0.438$  eV V<sup>-1</sup>.

We can give an alternative estimate of  $g_c$  from the lever arm and zero point voltage fluctuation  $V_{ZPF}$  of the resonator. From the design of the bare resonator, we evaluate its impedance  $Z_c \approx 2.5$  k $\Omega$ , which results in  $V_{ZPF} = \omega_r \sqrt{\hbar Z_r / \pi} \approx 10$   $\mu$ V, and in  $g_c/2\pi = \alpha_{g2} e V_{zpf} / (2\hbar) \approx 540$  MHz. This rough estimate agrees pretty well with the measured value  $g_c/2\pi = 513$  MHz.

As a comparison with previous charge-photon coupling rates in semiconductor QD devices, our coupling is one or two order of magnitudes higher than electrons in silicon ( $g_c/2\pi = 23$  MHz) [96], GaAs ( $g_c/2\pi = 119$  MHz) [132] or carbon nanotube ( $g_c/2\pi = 3.3$  MHz) [146] based DQDs. This can be explained by two reasons. First, the voltage fluctuation of our cavity is increased due to its high characteristic impedance. Indeed, by increasing the impedance of the cavity from 50  $\Omega$  to 2.5 k $\Omega$ , we improve the coupling by  $\sim 6$ . Second, the lever arm of the nanowire transistor  $\alpha = 0.6$  is higher than SiGe heterostructure devices (typically  $\alpha = 0.12$  [101]) or any other planar QDs.

In addition, if we compare the coupling strength  $g_c$  with the bare resonance frequency of the cavity  $f_r = 5.428$  GHz of our hybrid system,

$$\frac{g_c/2\pi}{f_r} \approx 10\%, \quad (4.8)$$

which means that we are at the limit of the ultra-strong coupling between light and matter [48]. It is comparable with the recent demonstration of ultra-strong coupling for electrons hosted in GaAs QDs, where the coupling strength reaches  $g_c/2\pi \approx 630$  MHz [126]. Finally, as  $g_s \propto g_c$ , this strong charge-photon coupling promises a strong spin-photon coupling, which we demonstrate in the next chapter.

**TAKEAWAY MESSAGES:**

- The hybrid circuit QED experiment is performed with a four-gate nanowire transistor connected to a  $2.5 \text{ k}\Omega$  microwave cavity.
- The resonance frequency of the cavity is  $f_r = 5.428 \text{ GHz}$ .
- The photon losses of the cavity in the single photons regime are  $(\kappa_i/2\pi, \kappa_c/2\pi, \kappa/2\pi) = (10 \text{ MHz}, 4 \text{ MHz}, 14 \text{ MHz})$ .
- The combined detuning lever-arm of G1 and G2 is  $\alpha = 0.607 \pm 0.004 \text{ eV V}^{-1}$  and the detuning lever-arm of G2 is  $\alpha_{g2} = 0.438 \text{ eV V}^{-1}$ .
- Ultra-strong charge-photon coupling with  $g_c/2\pi = 513 \pm 2 \text{ MHz}$ .
- The tunnel coupling of the charge qubit is  $t_c/h = 9.57 \pm 0.61 \text{ GHz}$ .

# STRONG HOLE SPIN-PHOTON COUPLING

## Contents

<b>5.1</b>	<b>Strong single spin-photon coupling</b> . . . . .	<b>86</b>
<b>5.2</b>	<b>Anisotropic Zeeman response of the hole spin</b> . . . . .	<b>89</b>
5.2.1	Detuning-magnetic field maps . . . . .	89
5.2.2	In-plane g-factors of the dots . . . . .	91
<b>5.3</b>	<b>Modulation of the spin-photon coupling strength</b> . . . . .	<b>92</b>
5.3.1	Magnetic field angular dependence of $g_s$ . . . . .	92
5.3.2	Spin-photon coupling model . . . . .	96
5.3.3	Single quantum dot regime . . . . .	97
<b>5.4</b>	<b>Spin decoherence</b> . . . . .	<b>100</b>
5.4.1	Two-tone spectroscopy . . . . .	100
5.4.2	Noise estimation . . . . .	102

**W**e have successfully hybridized the charge dipole with a single photon in the cavity, we can turn on the magnetic field to lift the spin degeneracy and proceed with the spin-photon interaction. Thanks to the spin-orbit interaction in the valence band of silicon, the spin hybridizes with the motion of the hole, combined with the charge-photon coupling, the spin-photon coupling is expected. In order to preserve the quality factors of the cavity, we only apply an in-plane magnetic field.

In this chapter, we first demonstrate the strong spin-photon coupling. Then we study the anisotropic Zeeman response of the hole at different magnetic field orientation. We also map the spin-photon coupling strength  $g_s$  as a function of magnetic field orientation and model its modulation with an interplay of the



anisotropic Zeeman response and the spin-orbit coupling. We also report a sizable spin-photon interaction when the hole is fully confined in a single quantum dot despite the reduction of its dipole moment. Finally we characterise the spin decoherence of the hybrid system.

## 5.1 Strong single spin-photon coupling

In what follows, the detuning of the DQD is set at  $\varepsilon = 0$  mV, where the electric dipole of the DQD is maximized. We apply an in-plane magnetic field  $\mathbf{B}$  which controls the Zeeman energy between the spin states given by  $E_Z = \mu_B |\mathbf{g}\mathbf{B}|$ . The magnetic field orientation is given by the angle  $\phi$  such that  $\phi = 0^\circ$  corresponds to an external magnetic field aligned with the axis of the nanowire. We probe in transmission the fingerprint of strong spin-photon coupling. A reminder of the device schematic is shown in Fig. 5.1 as well as the transmission as a response of the charge-photon interaction.

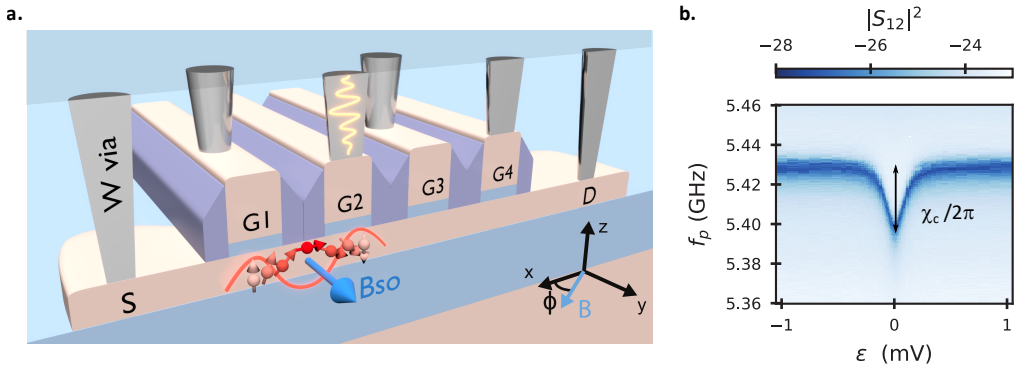


Figure 5.1 – (a) Schematic 3-dimensional cross section through the nanowire transistor with a DQD located under the gates G1 and G2. The effect of SOC is illustrated by a hole spin flipping during its tunneling between the two dots in the presence of a spin-orbit field  $\mathbf{B}_{so}$  (Blue arrow). The orange wave-packet on the via connecting G2 pictures the incoming photon from the microwave cavity. The external magnetic field  $\mathbf{B}$  is applied in-plane with an angle  $\phi$  to the nanowire axis. (b) Transmission amplitude of the feed-line as a function of the probe frequency  $f_p$  and detuning between the two dots  $\varepsilon$ . The DQD charge qubit interacts dispersively with the resonator leading to a frequency shift  $\chi_c/2\pi$  near  $\varepsilon = 0$ .

Due to the spin-orbit interaction present in the valence band of silicon, the spin-photon hybridization can be naturally achieved in two steps. First, the electric dipole produced by the single hole trapped in the DQD, around  $\varepsilon \sim 0$ , is hybridized with the single photon thanks to the electric-dipole interaction. Second, the spin-orbit interaction hybridizes the charge and spin degrees of freedom. If the spin coherently interacts with the microwave photon, then at the resonant magnetic field  $B_{res}$ , with  $\hat{g}\mu_B B_{res} = hf_r$ , an avoided crossing should be detected, signature

of the vacuum Rabi mode splitting described in Sec. 1.4.  $\hat{g}$  is the average g-factors between the left and right dot.

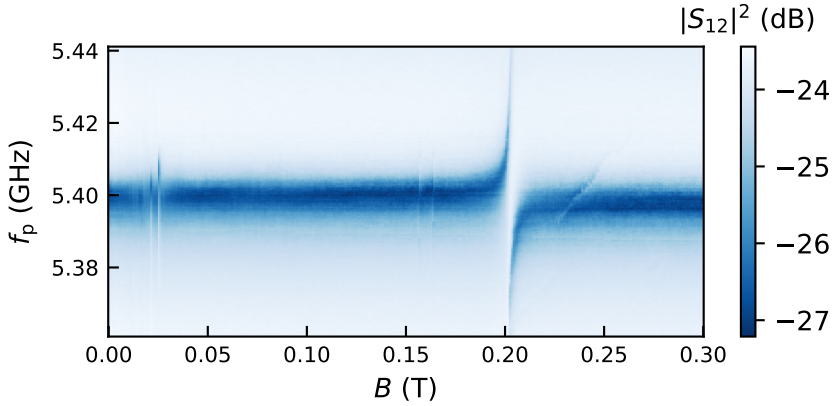


Figure 5.2 – The cavity transmission spectrum as a function of an in-plane magnetic fields for  $\phi = 90^\circ$ . There is a clear avoided crossing at 203 mT. There are also other states interacting with the cavity around 20 mT, 160 mT and 230 mT which are not coherent interactions.

Fig. 5.2 shows the transmission spectrum of the feedline as a function of an in-plane magnetic field perpendicular to the nanowire axis ( $\phi = 90^\circ$ ). We observe a very clear avoided crossing at 203 mT. To further investigate the spin-photon coupling we zoom in the resonance region, see Fig. 5.3 for the normalized transmission spectrum as function of magnetic field around  $B_{\text{res}} = 203$  mT. The normalization is done by subtracting the transmission spectrum out of the cavity resonance. The two vacuum Rabi normal modes are separated by the vacuum Rabi frequency  $2g_s/2\pi = 58$  MHz, giving an effective spin-photon coupling rate of  $g_s/2\pi = 29$  MHz. The half width at half maximum (HWHM) of the Rabi peaks corresponds to the combined spin and photon linewidths  $\frac{1}{2}(\gamma_s + \kappa/2) = 2\pi \times 6.8$  MHz. The vacuum Rabi mode splitting exceeds the combined linewidths by a factor four at this magnetic field angle.

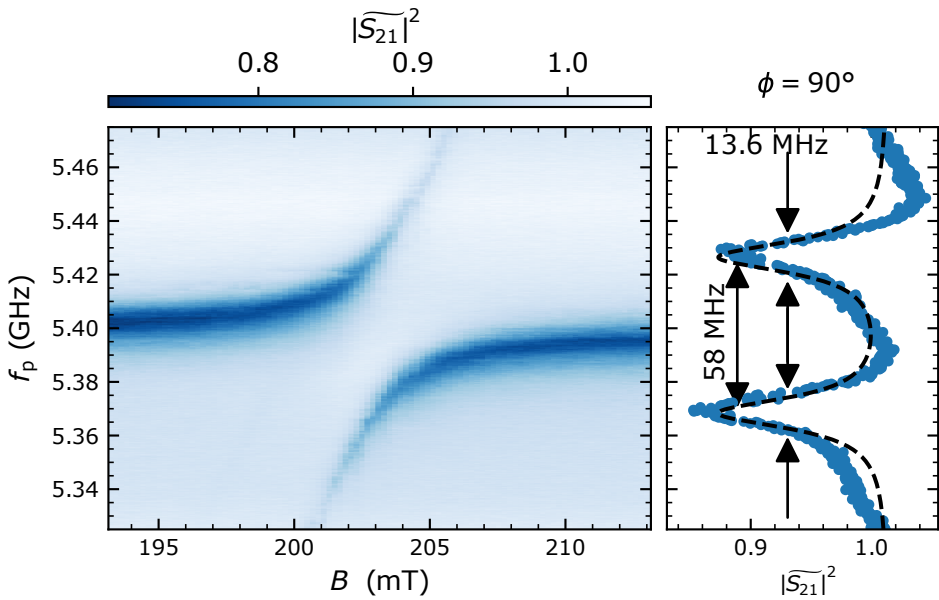


Figure 5.3 – Normalized transmission spectrum of the cavity as a function of in-plane magnetic field and the vacuum Rabi splitting at the position indicated by the arrows. The vacuum Rabi mode splitting exceeds the combined spin and photon linewidths by a factor four. The black dashed line is a fit with a superposition of two Lorentzian functions.

## 5.2 Anisotropic Zeeman response of the hole spin

Until now we have demonstrated the spin-photon strong coupling for a specific magnetic field orientation ( $\phi = 90^\circ$ ), however from previous hole spin qubits manipulations, we know that it has an anisotropic response with respect to the magnetic field orientation [38, 114]. Here we probe the spin-photon interaction with an in-plane magnetic field angle from  $0^\circ$  to  $180^\circ$  with magnetic spectroscopy. From these measurements, we give an estimate of the g-factors of the dot below G1 and G2 as a function of magnetic field angle  $\phi$ .

### 5.2.1 Detuning-magnetic field maps

As a way to characterise the coupled hole-cavity system, it is very useful to map the resonator response as a function of  $\varepsilon$  and  $B$  [14] for different magnetic field angles  $\phi$ . This magnetic spectroscopy measurement is performed with a microwave probe at  $f_p$ . For each magnetic field angle, at a given detuning value,  $f_p = f_r - \chi_c(\varepsilon)/2\pi$  which corresponds to the resonance frequency of the cavity adjusted with the charge qubit interaction (see Fig. 5.1.(b)). If the cavity does not interact then the transmitted amplitude corresponds to the dip of the resonance. If the photon interacts with the single spin or some systems in the environment then the resonance frequency shifts or splits for a coherent interaction and the probed transmitted signal increases.

Fig. 5.4 summarizes a selection of detuning vs magnetic fields maps probed with a microwave tone at  $f_p$  from  $0^\circ$  to  $180^\circ$  with respect to the Si nanowire axis. From these maps we can obtain different information as follows

- $\phi = 90^\circ$ : Around zero detuning the hole spin interacts with the photon between 200 mT and 220 mT as highlighted by the increased transmission signal, this is consistent with Fig. 5.3. When the detuning increases, the resonant magnetic field shifts to smaller values as the hole moves towards dot G1 or G2. The spin-photon interaction is asymmetric for positive or negative detuning due to the different g-factors in each dot. At large detuning, there is no interaction between the spin and the photon any more as the hole is located in a single quantum dot or at least not visible with the resolution of this map. For positive detuning, the interaction feature is doubled which may be due to the spins 1/2 of the environment which interact with the cavity ( $f_r = 5.43$  GHz) or the hole spin around 193 mT.
- $\phi = 0^\circ$ : Around zero detuning the hole spin interacts with the photon starting with an magnetic field of 400 mT and the interaction is never switched off until 800 mT. This predicts a very strong spin-photon interaction.
- $\phi = 11^\circ$ : Around zero detuning the hole spin does not strongly interact with the microwave photon until 800 mT, the resonance condition between the spin and the photon probably occurs at higher magnetic fields. We only probe the interaction for  $|\varepsilon| > 100 \mu\text{V}$ .

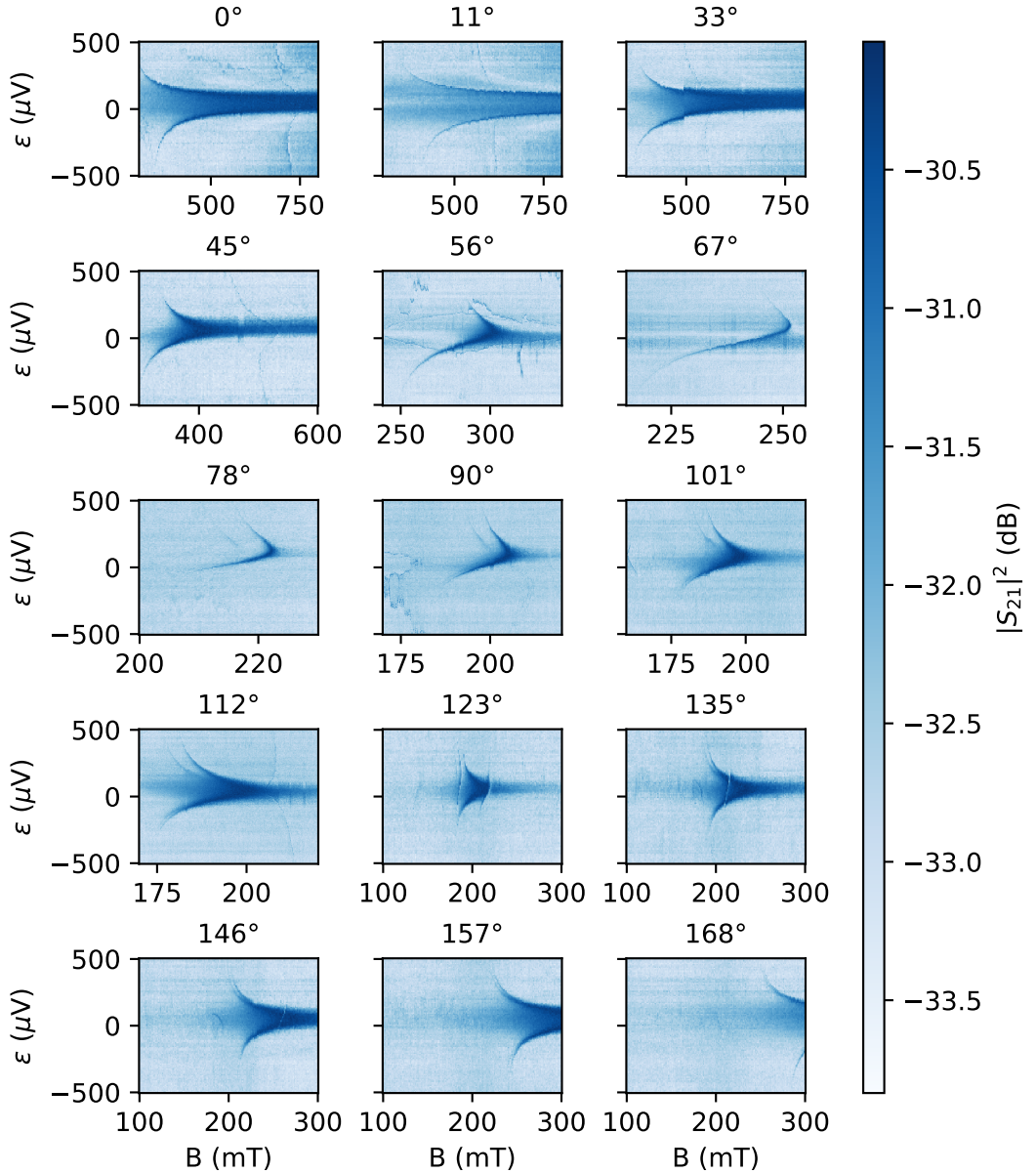


Figure 5.4 – Cavity transmission as a function of  $B$  and  $\varepsilon$  for different magnetic field angles. For a given detuning, the transmission response is probed at  $f_r - \chi_c(\varepsilon)/2\pi$ , which takes into account the dispersive shift of the resonance frequency due to the charge qubit.

- $\phi = 123^\circ$ : The hole spin interacts with the photon at zero detuning from 200 mT to 230 mT and the increased transmitted amplitude follows a V-shape as a function of detuning. However the photon also interacts with other systems as highlighted by the vertical lines at 185 mT and 215 mT which origin is unclear.

These detuning-magnetic field maps highlight the strong anisotropy of the hole spin in magnetic fields. At zero detuning, the spin-photon interaction occurs from 200 mT to above 800 mT and the interaction range in magnetic field is also magnetic field angle dependent. Thanks to these maps, we can estimate the magnetic field strength at which the vacuum Rabi splitting can be probed for each angle as shown in [Sec. 5.3](#).

## 5.2.2 In-plane g-factors of the dots

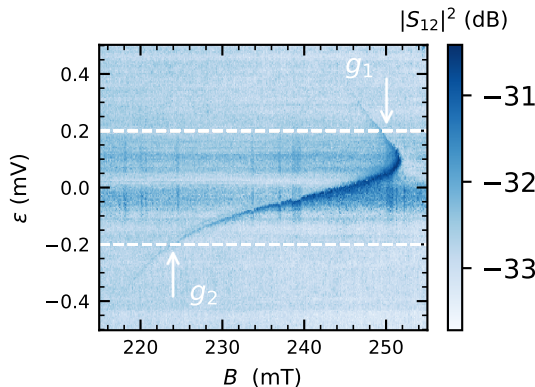


Figure 5.5 – Measurement of the g-factor for the left and right dot using the detuning-magnetic field map for  $\phi = 67^\circ$ .

From detuning-magnetic field maps presented [Fig. 5.4](#), we can map the effective in-plane g-factor for the dots below G1 and G2 and quantify the anisotropy of the hole in magnetic fields. The detuning axis is defined, see [Fig. 4.8](#), such that a positive detuning corresponds to the hole located below G1 while a negative number corresponds to a hole located below G2. For all magnetic field angles, we extract the resonance field condition at  $\varepsilon = \pm 200 \mu\text{V}$ , as  $\varepsilon > t_c$  we can suppose that the hole is localized either below G1 or G2. The value of the large detuning is chosen such that we can read the resonance condition for all magnetic field orientations as shown in [Fig. 5.5](#). We then estimate the g-factor of each dot using the resonant magnetic field condition  $\hat{g}\mu_B B = hf_r$  with  $f_r = 5.43 \text{ GHz}$ .

[Fig. 5.6](#) shows the g-factors of the dots below G1 and G2 as a function of the in-plane magnetic field angle  $\phi$ . We pinpoint that the two dots are relatively similar in terms of in-plane g-tensors. We observe an anisotropy of the Zeeman splitting

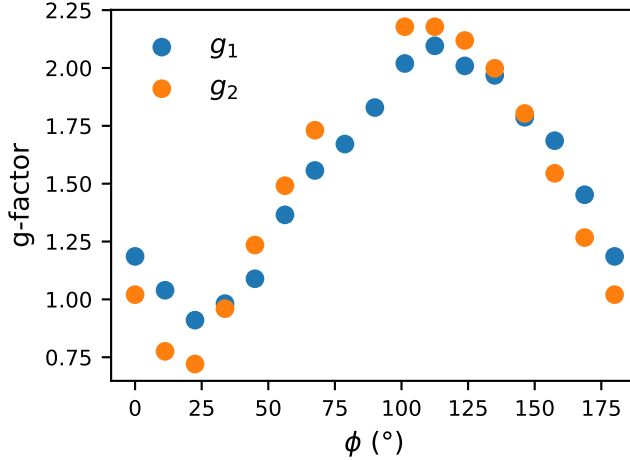


Figure 5.6 – g-factors of the dots below G1 (blue) and G2 (orange) as a function of the in-plane magnetic field angle  $\phi$  extracted at  $\varepsilon = \pm 200 \mu\text{V}$  from the resonance condition with the resonator.

with the g-factor ranging from 0.7 at  $\phi = 25^\circ$  to 2.2 at  $\phi = 110^\circ$ . The hole g-tensor anisotropy can be explained by the heavy-hole and light-hole mixing as the g-tensor translates the relative weight of the heavy-hole and light-hole components in the wave function [7, 114].

To preserve the quality factors of the resonator, we only apply in-plane magnetic fields. For a complete characterization of the g-tensor, readers may refer to [114] where the experiment is carried out with the first hole accumulated under the gate with a similar 4-gate transistor. In addition, we do not work in the single hole regime, even though our in-plane g-factors are consistent with the figures of the first hole in an 1D geometry.

## 5.3 Modulation of the spin-photon coupling strength

Due to the strong anisotropy of the hole spin in magnetic fields, we also expect a strong dependence of the spin-photon coupling on the magnetic field orientation, which is investigated in detail in this section. We have also measured a modulation of  $g_s$  of two orders of magnitude in detuning and probe a spin-photon coupling when the hole is localized in a single QD.

### 5.3.1 Magnetic field angular dependence of $g_s$

We now want to measure the vacuum Rabi mode splitting for all the magnetic field angles using the detuning-magnetic field maps. Indeed, from these maps we can estimate the resonant magnetic field and a spin sweet spot where the coupled hole-cavity systems is least sensitive to detuning noise. We then select

in these maps the detuning energy  $\varepsilon(\phi)$  at which the spin transition frequency  $\omega_s/2\pi$  satisfies the sweet spot condition  $\partial\omega_s/\partial\varepsilon = 0$  at resonance as indicated by the horizontal white dashed line in Fig. 5.7 for  $\phi = 101^\circ$ . In the following, all measurements of the spin-photon coupling have been performed close these sweet spots.

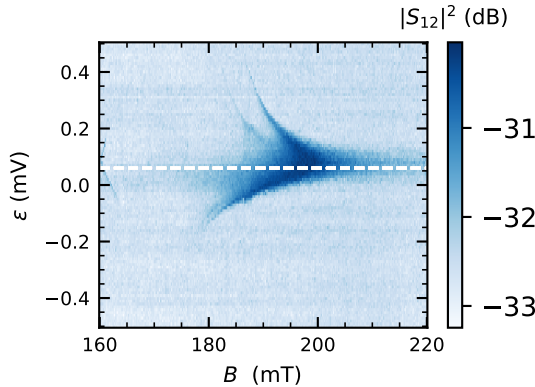


Figure 5.7 – Spin sweet spot for the spin-photon coupling at  $\phi = 101^\circ$ .

From the detuning-magnetic field maps shown in Fig. 5.4 we can estimate the resonance condition given by  $\hat{g}\mu_B B_{\text{res}} = \hbar f_r$  close to the spin sweet spot. We then measure the transmission through the feed line as a function of magnetic field for all angles to map the vacuum Rabi splitting and extract the spin-photon coupling strength, see Fig. 5.8. We observe a very clear avoided crossing for  $\phi$  from  $33^\circ$  to  $180^\circ$ . For  $\phi = 3^\circ$  and  $\phi = 28^\circ$ , the vacuum Rabi splitting pattern is not complete due to the limit of the magnetic field in our set-up which is 1 T.

From these measurements, we then fit the dressed states energies using Eq. (1.46) and Eq. (1.47) to extract the spin-photon coupling strength  $g_s$ . We plot in Fig. 5.9.(a) the vacuum Rabi mode splittings for all measured angles. A large modulation of  $g_s/2\pi$  from 10 MHz to 290 MHz is observed when rotating the magnetic field by  $180^\circ$  in-plane, see Fig. 5.9.(b). At the same time,  $B_{\text{res}}$  is also greatly modulated due to an interplay of the g-factor anisotropy and spin-orbit interaction strength, see Fig. 5.9.(c). A higher coupling strength can be achieved between  $0^\circ$  to  $33^\circ$  but with a resonant condition higher than 1 T which is the limit of our in-plane magnetic field. The theoretical fit of  $g_s$  and  $B_{\text{res}}$  is discussed later in Sec. 5.3.2.

A clear vacuum Rabi mode splitting and hence a strong spin-photon coupling has been observed for all field orientations. The quality of the strong coupling is generally characterised by the ratio between the coupling strength and the decoherence rate  $2g_s/(\gamma_s + \kappa/2)$ , see Fig. 5.10. It gives the number of vacuum Rabi oscillations that are possible before the combined system decoheres and reaches 27 for  $\phi = 0^\circ$ . For the same magnetic field orientation, we also achieve a cooperativity,  $C = 4g_s^2/(\gamma_s\kappa)$  [33], of 1600 demonstrating a very strong light-matter



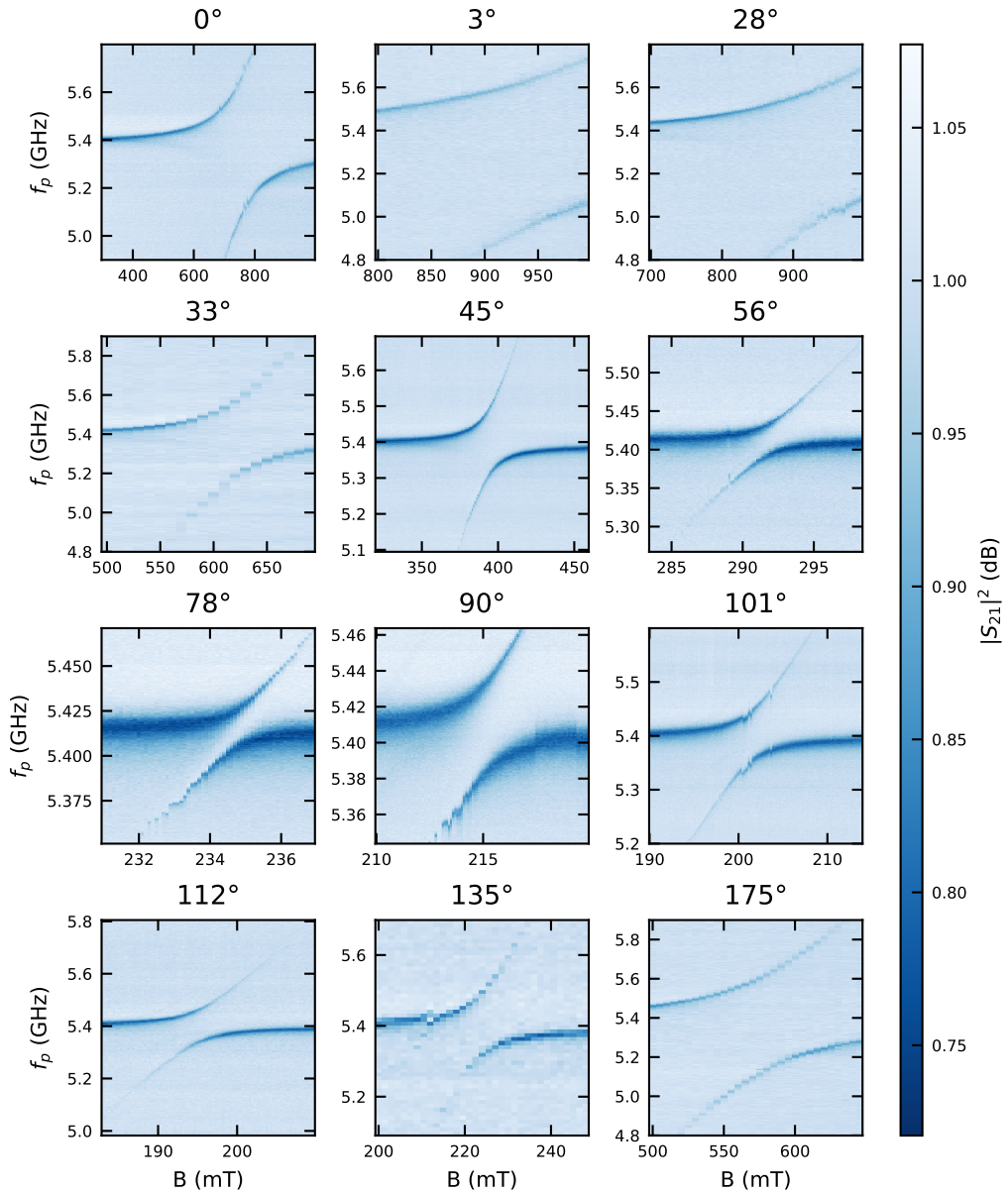


Figure 5.8 – Cavity transmission as a function of  $B$  and  $f_p$  for different magnetic field angles showing vacuum Rabi splittings.

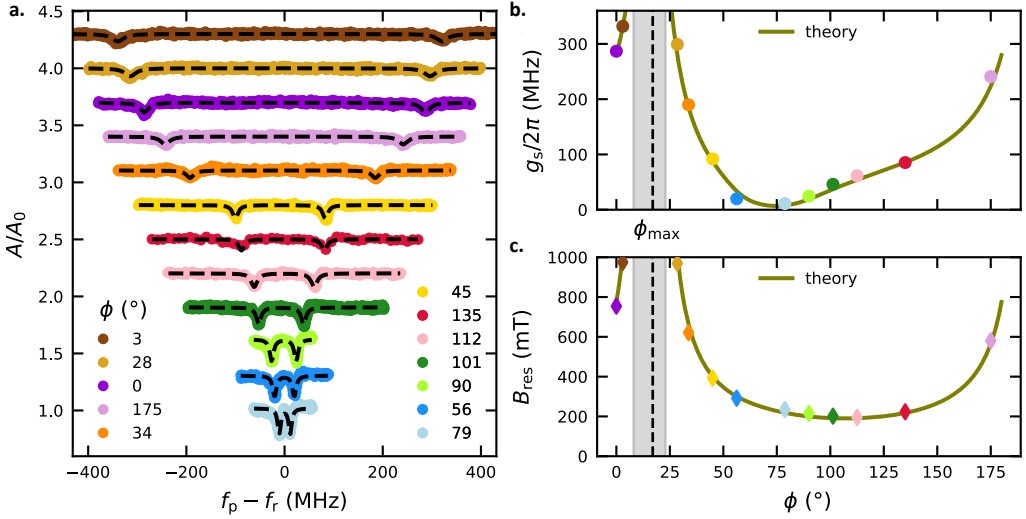


Figure 5.9 – Magnetic field angular dependence of the spin-photon interaction. (a) Normalized transmission curves as a function of  $f_p$  for various  $\phi$ , all showing clear vacuum Rabi mode splittings from 20 MHz to 660 MHz. The curves are shifted from each others for reading clarity. The black dashed lines corresponds to a fit with a superposition of two Lorentzian functions. (b) Spin-photon coupling as a function of magnetic field angles with the theory fit. The grey shaded region in (b) and (c) corresponds the magnetic field orientation where the spin-photon resonance is achieved for magnetic fields larger than 1 T, which are inaccessible in our experiment. (c) Resonance field as a function of magnetic field angles with the theory fit.

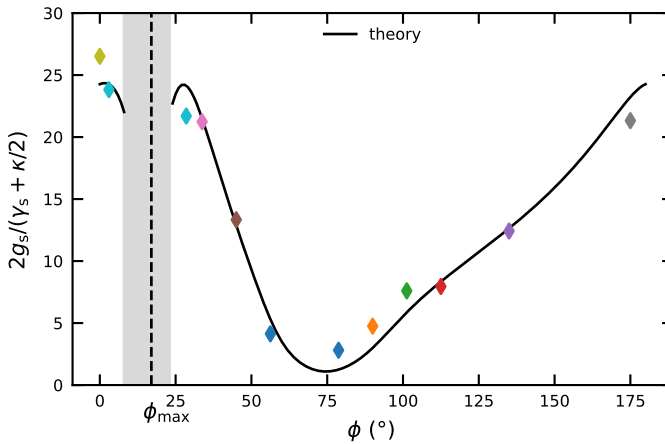


Figure 5.10 – Spin-photon interface quantified with the ratio between the coupling strength and the decoherent rate of the hybrid state.

interaction. We can stress that the relatively large cavity decay rate  $\kappa/2\pi = 14$  MHz is the main factor that leads to small values of  $2g_s/(\gamma_s + \kappa/2)$  and  $C$ , especially around  $70^\circ$ , where  $g_s$  and  $\gamma_s$  are minimal. The theory fit is given by a noise estimation on the spin decoherence which is detailed in [Sec. 5.4.2](#).

### 5.3.2 Spin-photon coupling model

To pinpoint the exact nature of the spin-photon coupling, we model our system as a single hole spin in a DQD as described in [Sec. 1.4](#) and derive an analytical calculation of the spin-photon coupling  $g_s$ .

For a given magnetic field orientation  $\phi$ , we introduce the average Zeeman energy of the two dots,  $\bar{E}_Z = \frac{1}{2}(g_L^* + g_R^*)\mu_B B$ , and the Zeeman energy difference,  $\Delta E_Z = (g_L^* - g_R^*)\mu_B B$ . We assume  $\Delta E_Z \ll \bar{E}_Z$ . We can then rewrite the total Hamiltonian of the hybrid system in the eigenbasis at  $t_{sf} = 0$  as

$$\mathcal{H} = \begin{pmatrix} -\frac{1}{2}(E_0 + \bar{E}_Z) & 0 & 0 & -t_{sf} \\ 0 & \frac{1}{2}(E_0 - \bar{E}_Z) & t_{sf} & 0 \\ 0 & t_{sf} & -\frac{1}{2}(E_0 - \bar{E}_Z) & 0 \\ -t_{sf} & 0 & 0 & \frac{1}{2}(E_0 + \bar{E}_Z) \end{pmatrix}, \quad (5.1)$$

where  $E_0 = \sqrt{\varepsilon^2 + 4t_{sc}^2}$  is the spin-conserving band gap.  $\mathcal{H}$  can be diagonalised with the resulting eigenenergies

$$\left\{ -\frac{E_+}{2}, -\frac{E_-}{2}, \frac{E_-}{2}, \frac{E_+}{2} \right\}, \quad (5.2)$$

with  $E_+ = \sqrt{(E_0 + \bar{E}_Z)^2 + 4t_{sf}^2}$ , and  $E_- = \text{sign}(E_0 - \bar{E}_Z)\sqrt{(E_0 - \bar{E}_Z)^2 + 4t_{sf}^2}$ .

Depending on the sign of  $E_0 - \bar{E}_Z$ , the lowest-lying excitation is either the first one with energy  $-E_-/2$ , or the second one with energy  $+E_-/2$ . Hence the spin-photon coupling can be written as

$$\begin{aligned} g_s &= g_c \left| \theta(E_0 - \bar{E}_Z)d_{01} + \theta(\bar{E}_Z - E_0)d_{02} \right|, \\ &= g_c \left| \cos \varphi_0 \left| \theta(E_0 - \bar{E}_Z) \sin \left( \frac{\varphi_+ - \varphi_-}{2} \right) + \theta(\bar{E}_Z - E_0) \cos \left( \frac{\varphi_+ - \varphi_-}{2} \right) \right| \right|, \end{aligned} \quad (5.3)$$

where  $\theta(x)$  is the Heavyside step function and  $d_{01}$  and  $d_{02}$  are the dipolar matrix elements between the ground state and the two first excited states which are dependent of the left/right spin-charge mixing angle  $\varphi_0$  such that  $E_0 \cos \varphi_0 = 2t_{sc}$  and  $E_0 \sin \varphi_0 = \varepsilon$ .  $\varphi_-$  and  $\varphi_+$  are defined such as  $E_+ \cos \varphi_+ = E_0 + \bar{E}_Z$ ,  $E_+ \sin \varphi_+ = 2t_{sf}$ ,  $E_- \cos \varphi_- = E_0 - \bar{E}_Z$ , and  $E_- \sin \varphi_- = 2t_{sf}$ , which are convenient parameters for the calculation.

Eq. (5.3) reproduces very well the results of Fig. 5.9.(b). Note that this expression neglects the Zeeman energy differences in the magnetic Hamiltonian of the two QDs but it still takes into account the effect of the g-matrix differences on  $t_{sf}$ , which is relevant for our experiment as the principal g-factors of the dots are close to each other, see Fig. 5.6.

We can derive a simpler expression of  $g_s$  at zero detuning when  $\bar{E}_Z < 2t_{sc}$  and  $\bar{E}_Z \ll 2t_c$ . In this case, the spin-charge hybridization is relatively small and we can introduce an effective spin-orbit field,  $\mathbf{B}_{so}$  such that  $\mu_B \mathbf{B}_{so} = t_c \sin \eta \mathbf{n}_{so}$  where  $2\eta = 2d/\ell_{so}$  with  $d$  the interdot distance and the spin-orbit length  $\ell$  introduced in Sec. 1.4.2. Eq. (5.3) can then read as

$$g_s = g_c \frac{\mu_B^2}{2t_c^2} |(\mathbf{g}\mathbf{B}) \times (\mathbf{g}\mathbf{B}_{so})| = g_c \frac{\mu_B^2}{2t_c^2} |\text{cof}(\mathbf{g})(\mathbf{B} \times \mathbf{B}_{so})|, \quad (5.4)$$

where  $\text{cof}(\mathbf{g}) = \det(\mathbf{g}^t)\mathbf{g}^{-1}$  is the cofactor matrix of  $\mathbf{g}$ . Here the g-matrix are taken as equal in the left and right dot, which is verified at a given magnetic field angle ( $\mathbf{g}_L(\phi) = \mathbf{g}_R(\phi)$  whatever  $\phi$ ). The spin-photon coupling is therefore zero when  $\mathbf{B}$  is parallel to  $\mathbf{B}_{so}$ . Also note that  $g_s \propto \mathbf{B}$ , as expected for a spin-like transition.

By experiment, we can access to the principal g-factors of the two dots and  $t_c$ , therefore the only unknown is  $\mathbf{B}_{so}$  which consists of three fit parameters. With this model, we are able to predict not only  $g_s$  accurately, but also the resonance field precisely, see Fig. 5.9.(b) and (c).  $g_s$  is minimal around  $\phi = 70^\circ$  suggesting that  $\mathbf{B}_{so}$  is about  $20^\circ$  off the  $y$ -axis. Moreover,  $\mathbf{B}_{so}$  must have a small out-of-plane component as  $g_s$  never vanishes for in-plane magnetic fields.

We can also derive the energy spectra of the spin states as a function of DQD detuning for a given magnetic field orientation, as shown in Fig. 5.11. For  $\phi \sim 70^\circ$ , the spin-charge mixing induced by the SOC is minimal whereas it is much stronger around  $\phi \sim 0^\circ$ , in agreement with the evolution of  $g_s$ .

### 5.3.3 Single quantum dot regime

For quantum state transfer protocols, it is important to turn qubit-cavity coupling on for quantum state transfer, and off for qubit state preparation. In the previous reports electrons spins in Si entangled with a photon, it is achieved by electrically tuning  $t_c$  and  $\varepsilon$  [95, 124]. In the following, we also explore the voltage tuneability of  $g_s$  at  $\phi = 11.25^\circ$ . To do so, we use once again the detuning-magnetic field maps shown in Fig. 5.4 and follow the resonance condition for different DQD detunings.

Surprisingly, at very large detuning,  $\varepsilon/h > 100$  GHz, two dips are still visible in the transmission signal through the cavity as a function of  $B$ , see Fig. 5.12.(a). Their separation reveals a spin-photon coupling  $g_s/2\pi \sim 1$  MHz. In this case  $\gamma_s < g_s < \kappa$ , so that a clear vacuum Rabi mode splitting cannot be resolved (bad cavity limit [102]). To further support the existence of a single QD spin-photon interaction, we measure  $g_s$  as a function of detuning, see Fig. 5.12.(b). We find

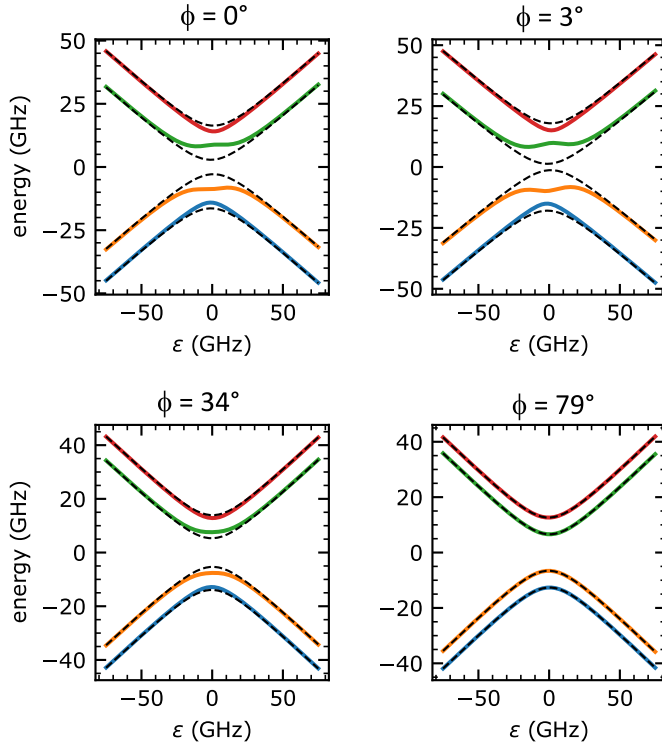


Figure 5.11 – Energy diagrams of the four spin states for different magnetic field angles. The black dashed lines depict the spin states in the absence of SOC, where the spin-splitting energies are independent of the DQD detuning. The SOC primarily couples the  $|-, \uparrow\rangle$  and  $|+, \downarrow\rangle$  states. This leads to spin-charge mixing with spin-splitting energies dependent on the DQD detuning. Notice that the SOC-induced mixing is much weaker for  $\phi = 79^\circ$  than for  $\phi = 3^\circ$ , which explains the different magnitude of the spin-photon couplings  $g_s$  observed in Fig. 5.9. Even at very large mixing at  $\phi = 3^\circ$ , the probed spin transition is a well defined two level system where the third level is separated from it by a few tens of GHz.

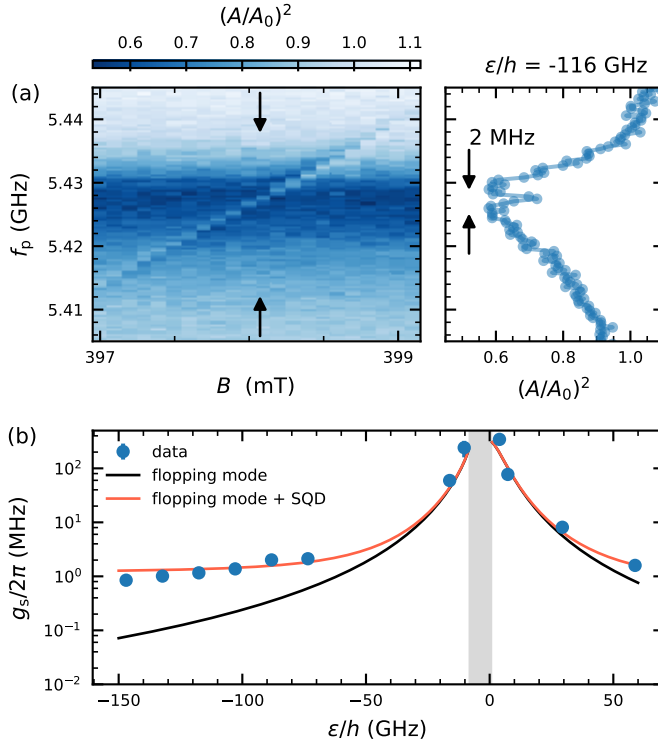


Figure 5.12 – Spin-photon interaction in the single quantum dot limit for  $\phi = 11.25^\circ$ . (a) Normalized transmission as a function of  $f_p$  and  $B$  at  $\varepsilon = 0.5 \text{ meV} = -116 \text{ GHz}$  with a line cut in frequency (indicated by arrows) on the right. The spin transition is clearly visible and a double-dip structures at resonance of  $\sim 2 \text{ MHz}$  is observed. (b)  $g_s$  as a function of  $\varepsilon$ . The large spin-photon coupling around  $\varepsilon \sim 0$  is very well captured by the DQD flopping mode whereas it underestimates  $g_s$  by more than one order of magnitude at large  $\varepsilon$ , where the hole is confined in a single dot (SQD) below either G1 ( $\varepsilon > 0$ ) or G2 ( $\varepsilon < 0$ ). By adding an  $\varepsilon$  independent single dot coupling strength to  $g_s$  in the numerical model, we can very well reproduce the experimental data.

that  $g_s$  is modulated by more than two orders of magnitude when increasing  $|\varepsilon|$ , but tends to saturate once the hole is fully localized in the right dot.

In the single dot regime, the electric-dipole interaction is greatly reduced as the detuning dependence of the charge-photon coupling is  $g_c^{\text{eff}} = 2g_c t_c / \sqrt{4t_c^2 + \varepsilon^2}$ . To characterize the value of this single dot coupling, we fit  $g_s$  as a function of detuning with

$$g_s(\varepsilon) = g_s^{(\text{DD})}(\varepsilon) + p_L(\varepsilon)g_s^{(L)} + p_R(\varepsilon)g_s^{(R)}, \quad (5.5)$$

where  $p_{L,R}$  are the ground state probabilities of being in left or right dot,  $g_s^{(\text{DD})}$  is the spin-photon coupling from the flopping mode DQD model, and  $g_s^{(L,R)}$  are the asymptotic spin-photon couplings in the left and right dots. By taking into account the single dot coupling strength, we accurately reproduce the experimental values shown in Fig. 5.12.(b) with  $g_s^{(R)}/2\pi = 1.16$  MHz, and  $g_s^{(L)}/2\pi = 0.66$  MHz. This is the first report of a single dot spin-photon interaction with MHz coupling strengths as predicted by recent theoretical studies of circuit QED in a minimal architecture [98, 21].

## 5.4 Spin decoherence

Due to the very large spin-charge mixing induced by the SOC, the spin decoherence time may be reduced by the charge noise. In this section, we therefore assess the spin decoherence rates by two-tone spectroscopy and by a noise estimation model.

### 5.4.1 Two-tone spectroscopy

After the quantification of the spin-photon coupling, we are also interested in the spin decoherence  $\gamma_s$ . From the Rabi normal mode fitting, we extract the FWHM which corresponds to  $2(\gamma_s + \kappa/2)$ , and as we know that  $\kappa/2\pi = 14$  MHz we can deduce the spin linewidth. However, for angles where the combined width is fully dominated by  $\kappa$ ,  $\gamma_s$  cannot be extracted like this. Therefore, two-tone spectroscopy can be used to extract the linewidth of the spin transition.

To do so, we apply a second microwave tone in addition of the probe tone. The power applied on both sources has to be low enough that the spin transition is not power broaden. Fig. 5.13 shows the two-tone spectroscopy of the spin state at  $\phi = 101.25^\circ$  as a function of the spectroscopy power and frequency  $f_s$ . The fixed tone is applied by the VNA with an output power of  $-40$  dBm. We probe the spin state above the resonance in a region where the detuning  $\Delta_{\text{2tone}} = f_r - f_q$  is of the order of  $10g_s/2\pi$ . For  $\phi = 101.25^\circ$ ,  $g_s/2\pi = 50$  MHz, so we are in this far detuned region with  $f_q = 5.87$  GHz. As a function of spectroscopy power, the spin transition narrows down until  $-40$  dBm and then the signal vanishes, probably due to the very low signal-to-noise ratio. From the Lorentzian fit of the transmission phase at  $-40$  dBm, we extract the spin decoherence  $\gamma_s = 4$  MHz. We repeat the

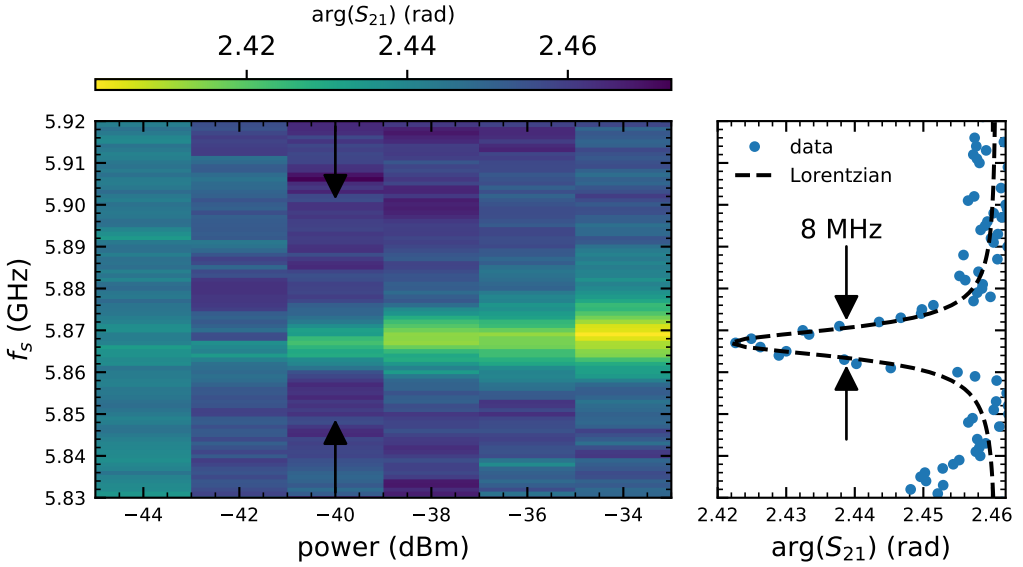


Figure 5.13 – Two tone spectroscopy of the spin transition as a function of applied spectroscopy power for  $\phi = 101.25^\circ$ . The phase response of the transmission is probed by at  $f_p = 5.401$  GHz. When the spectroscopy frequency is in resonance with the spin qubit, the occupation of the qubit state changes due to the spin-photon interaction, which leads to an modified cavity response. The line cut of the spin transition in the region indicated by the arrows gives a spin decoherence rate of  $g_s/2\pi = 4$  MHz.



same procedure for other angles from  $33^\circ$  to  $101^\circ$  where the photon loss dominates the combined linewidth.

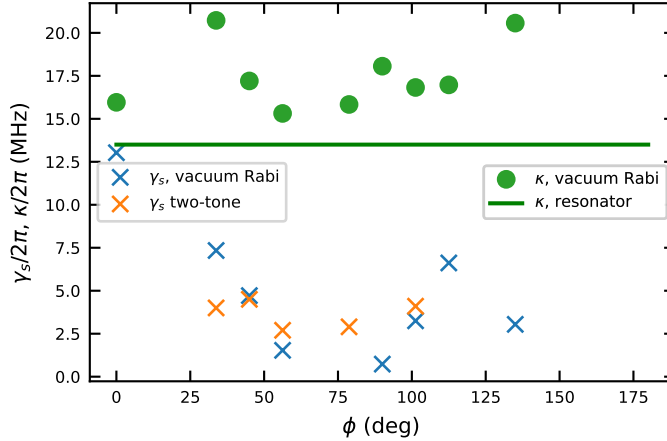


Figure 5.14 – Angular dependence of the spin and photon decoherences.

Fig. 5.14 shows  $\kappa$  and  $\gamma_s$  as a function of  $\phi$  from  $0^\circ$  to  $180^\circ$ .  $\kappa$  is extracted when the spin qubit is largely detuned from the resonator such that the resonance is only dispersively shifted.  $\gamma_s$  is extracted from the avoided crossing (blue crosses) or two-tone spectroscopy (orange crosses). There is a good agreement between both techniques for the spin decoherence and the lifetime of the hybrid system is limited by the photon decay at all magnetic field orientations.

## 5.4.2 Noise estimation

We also extract the spin decoherence by fitting the decoherence evolution depending on the magnetic field orientation, shown in Fig. 5.10. We assume that  $\gamma_s = \gamma_0 + \gamma_\epsilon$  with  $\gamma_\epsilon$  the decoherence rate originating from fluctuations on the detuning energy due to charge noise and  $\gamma_0$  accounts for any other decoherence mechanism.  $\gamma_\epsilon$  can be written as [119, 77]

$$\frac{\gamma_\epsilon}{2\pi} = \frac{1}{4\pi^2\hbar} \sqrt{\frac{1}{2} \left( \frac{\partial\omega_s}{\partial\epsilon} \right)^2 \sigma_\epsilon^2 + \frac{1}{4} \left( \frac{\partial^2\omega_s}{\partial\epsilon^2} \right)^2 \sigma_\epsilon^4}. \quad (5.6)$$

As we work at the detuning sweet spot  $\partial\omega_s/\partial\epsilon = 0$ , Eq. (5.6) becomes

$$\frac{\gamma_\epsilon}{2\pi} = \frac{1}{8\pi^2\hbar} \left| \frac{\partial^2\omega_s}{\partial\epsilon^2} \right| \sigma_\epsilon^2. \quad (5.7)$$

Only  $\gamma_0$  and  $\sigma_\epsilon$  in the spin decoherence rate are unknown, and we extract them from fitting Fig. 5.10, with  $\partial^2\omega_s/\partial\epsilon^2$  calculated by single hole spin total Hamiltonian. We assume that  $\gamma_0$  is independent on  $\phi$ , and  $\kappa/2 \approx 2\pi \times 9$  MHz taken as an

average (see Fig. 5.14). We obtain that way  $\sigma_\varepsilon = 6.4 \mu\text{eV}$  and  $\gamma_0/2\pi = 3.4 \text{ MHz}$ . We note that  $\gamma_0$  agrees qualitatively with the data of Fig. 5.14.

Finally, we can use this fit to estimate the dephasing rate of the charge qubit at the sweet spot  $\varepsilon = 0$ . Assuming  $\gamma_0$  only applies to the spin degree of freedom and that detuning noise is again the main decoherence mechanism, we find  $\gamma_c/2\pi = \sigma_\varepsilon^2(\partial^2\omega_c/\partial\varepsilon^2)/(8\pi^2\hbar) = 8.2 \text{ MHz}$  for  $2t_c/\hbar = 19.2 \text{ GHz}$ . Note that  $\partial^2\omega_c/\partial\varepsilon^2 \propto 1/t_c$ , so that a large tunneling gap reduces dephasing. This leads to low dephasing with respect to previous charge-photon coupling experiments [132, 77], comparable to noise-mitigated charge qubits [126].

To conclude this chapter, our spin-photon coupling strength can be as large as 330 MHz and it clearly outperforms previous reports with electron spins in silicon with  $g_s$  ranging from 10 MHz to 40 MHz [95, 124, 20, 61]. Furthermore, the strong SOC enhanced by the 1D geometry [73, 98, 21], enables unprecedented spin-charge mixing, characterised a ratio  $g_s/g_c$  up to 60%, while keeping a spin decoherence rate lower than 20 MHz. As the spin coherence is mostly limited by spin-charge mixing at strong spin-photon interaction, it is of great interest to reduce the charge qubit dephasing rate  $\gamma_c$ . Therefore, to improve even more this spin-photon interface, future works should explore strategies to maximize the ratio  $g_c/\gamma_c$  as already demonstrated for GaAs/AlGaAs DQDs [126] and reduce the photon loss rate to reach  $\kappa \lesssim 1 \text{ MHz}$  as demonstrated in [97, 62].

**TAKEAWAY MESSAGES:**

- The vacuum Rabi mode splitting can be tuned from 20 MHz to 660 MHz with the in-plane magnetic field orientation.
- Both dots show similar g-matrix anisotropies, with  $E_Z \simeq 1.3\mu_B B$  when  $\mathbf{B}$  is along  $x$ -axis, and  $E_Z \simeq 2\mu_B B$  when  $\mathbf{B}$  is along  $y$ -axis.
- The spin-photon coupling is mediated by an interplay of SOC and the g-tensor modulation in the valence band of silicon leading to  $g_s \propto g_c |(\mathbf{g}\mathbf{B}) \times \mathbf{g}\mathbf{B}_{\text{so}}|$  with  $\mathbf{g}$  the average g-matrix of the two dots.
- The spin-photon coupling can be electrically tuned from the DQD to the single QD regime with a modulation of  $g_s$  by two orders of magnitude.
- The spin-charge mixing reaches up to 60 %.
- The spin decoherence rates do not exceed 20 MHz even for a very strong spin-charge mixing.
- The spin-photon interface is mostly limited by the photon decay rate  $\kappa/2\pi = 14$  MHz.

# CONCLUSIONS AND PERSPECTIVES



circuit QED has proven to be a very powerful tool for superconducting qubits [17]. In this work, we have extended the circuit QED to a novel hybrid platform using hole spins localised in a Si-MOS device coupled to microwave photons in a superconducting resonator.

In [Chap. 3](#), we explore the ability of NbN superconducting resonators to operate in the single photon regime in a finite magnetic field. The superconducting resonators are made from thin films of NbN (thickness of 10 nm) with a high kinetic inductance of 192 pH/□ such that we can design high-impedance resonators to maximize the voltage fluctuations, hence the charge-photon coupling. We demonstrate photon loss rates below 1 MHz in the single photon regime and at finite magnetic fields for resonators up to 4.1 kΩ on a silicon wafer with a thermal grown oxide layer. We then integrate the resonators with the Si-MOS devices, which increases the photon loss of the resonator to a few MHz, and present our strategies to mitigate the microwave losses.

[Chap. 4](#) presents the charge-photon coupling of a single hole in a double quantum dot with a microwave photon. We achieve a coupling strength of 513 MHz, bordering the ultra strong coupling regime, enabled by the large voltage fluctuation of a 2.5 kΩ resonator accompanied by a large gate lever arm offered by the MOS nanowire devices.

In [Chap. 5](#) we finally harness the spin-photon coupling mediated by the intrinsic SOC present in the valence band of silicon. The ultra strong charge-photon coupling and the strong SOC results in a spin-photon coupling up to 330 MHz, exceeding previous demonstrations with electron spins in silicon by one order of magnitude [95, 124, 20, 61]. We achieve a spin-charge mixing with  $g_s/g_c$  greater than 60%, while keeping the spin decoherence rates similar to electron spins. The cooperativity of our hybrid system reaches 1600 and compares favorably with early reports on superconducting circuits [148]. In addition, we also probe a spin-photon coupling in the single QD regime where the charge dipole moment extinguishes, offering the possibility of circuit QED experiment with a reduced footprint.

Even though the spin-photon interaction is remarkably strong, this interface can still be further improved. For instance, the impedance of the resonator can be increased even more by adjusting the CPW dimensions to achieve an even higher charge-photon coupling. The quality factors of the cavity can also be improved with air-bridges connecting the ground planes around. We could also switch from the interdigitated fingers capacitors of the low pass filters to a plane capacitor with a thin metallic film parallel to the NbN layers [62] such that more fanout lines would fit on the chip with a good ground plane definition. A careful engineering of the microwave cavity and the on-chip low-filters can reduce the photon loss to around 1 MHz [97, 62], then we can achieve cooperativities above 10 000 as for superconducting circuits [127]. In addition, the integration of a quantum limited amplifier would also be a great asset to the set-up to improve the signal-to-noise ratio and fasten the measurements time.

As perspectives, the most natural future work based on this hybrid system is the long-range spin-spin interaction and demonstration of two qubits gate operations [15] by placing a second device at the other end of the resonator. With the figures of merit of the present device, we expect to achieve a two-qubit gate with a fidelity up 90% [15]. Furthermore, there are many other experiments that can be carried out with a single spin. So far, we are restricted to the transverse spin-photon coupling, we could harness the longitudinal coupling [26] opening a new scheme of circuit QED with spins. Or we could also explore an even number of charges transitions and work with a singlet-triplet spin qubit composed of two spins  $1/2$  [84] instead of the flopping mode qubit [104]. The experimental demonstration of a single-shot high fidelity dispersive spin readout by the cavity [39] would also be a new breakthrough in the semiconductor qubits field, which could be possible if the relaxation time of the flopping mode spin qubit studied here is long enough (to be measured). With an improved microwave cavity, we can also further explore circuit QED with a single dot [98, 21]. Therefore, this hole spin-photon interface should enable to tap all the potentials of circuit QED with hole spins in semiconductor quantum dots.

## INPUT-OUTPUT THEORY

The Jaynes-Cummings model of the interaction only takes into account photons inside the cavity, however measuring the cavity means that it is an open quantum system. A more sophisticated model would be the input-output formalism which is the quantum version of the scattering theory[44], where the input and output coefficients are replaced by creation and annihilation operators of the bosonic modes.

The open system can be described by the following Hamiltonian

$$H = H_{sys} + H_{bath} + H_{int}, \quad (\text{A.1})$$

where  $H_{sys}$  describes the DQD and a single mode of the cavity,  $H_{bath}$  the field outside the cavity with  $n$  bosonic modes and  $H_{int}$  the coupling between the internal and external field of the cavity. We note  $\hat{a}$  ( $\hat{a}^\dagger$ ) and  $\hat{b}$  ( $\hat{b}^\dagger$ ) the bosonic creation (annihilation) operators respectively to the cavity mode and the environment bath.

The system Hamiltonian is given by the Jaynes-Cummings Hamiltonian:

$$H_{sys} = \hbar\Delta a^\dagger a + \hbar\frac{\Omega}{2}\sigma_z + \hbar\tilde{g}_c(a\sigma_+ + a^\dagger\sigma_-), \quad (\text{A.2})$$

where  $\Delta = \omega - \omega_p$  with  $\omega$  the cavity resonance frequency and  $\omega_p$  the probe frequency.

The bath Hamiltonian is given by

$$H_{bath} = \sum_q \hbar\omega_q b_q^\dagger b_q, \quad (\text{A.3})$$

where  $q$  labels the quantum numbers of the independent harmonic oscillator bath modes obeying

$$[b_p, b_q^\dagger] = \delta_{pq}. \quad (\text{A.4})$$

The interaction Hamiltonian, in the rotating wave approximation, is

$$H_{int} = i\hbar \left( \sum_q \lambda_q [b_q^\dagger a - a^\dagger b_q] \right), \quad (\text{A.5})$$

The Heisenberg equation of motion for the bath variables is given by

$$\dot{b}_q = \frac{i}{\hbar} [H, b_q] = -i\omega_q b_q + \lambda_q a, \quad (\text{A.6})$$

while the cavity mode is governed by the following equation of motion

$$\dot{a} = \frac{i}{\hbar} [H_{sys}, a] - \sum_q \lambda_q b_q. \quad (\text{A.7})$$

From Eq. (A.6), the bath variable can be written as the differential equation's solution

$$b_q = e^{-i\omega_q(t-t_0)} b_q(t_0) + \int_{t_0}^t d\tau e^{-i\omega_q(t-\tau)} \lambda_q a(\tau) \quad (\text{A.8})$$

with  $t_0 < t$  the initial time and  $b_q(t_0)$  the initial value.

Substituting Eq. (A.8) into Eq. (A.7):

$$\dot{a} = \frac{i}{\hbar} [H_{sys}, a] - \sum_q \lambda_q e^{-i\omega_q(t-t_0)} b_q(t_0) - \sum_q \lambda_q \int_{t_0}^t d\tau e^{-i\omega_q(t-\tau)} \lambda_q a(\tau) \quad (\text{A.9})$$

To simplify the second sum, we define the loss rate  $\kappa$  as

$$\kappa(\omega) = 2\pi \sum_q \lambda_q^2 \delta(\omega - \omega_q). \quad (\text{A.10})$$

Thus, the second sum of Eq. (A.9) can be written as

$$\sum_q \lambda_q^2 \int_{t_0}^t d\tau e^{-i\omega_q(t-\tau)} a(\tau) = \int_{t_0}^t d\tau \int_{-\infty}^{+\infty} \frac{\kappa(\omega) d\omega}{2\pi} e^{-i\omega(t-\tau)} a(\tau). \quad (\text{A.11})$$

Using the Markov approximation that  $\kappa(\omega) = \kappa$

$$\sum_q \lambda_q^2 \int_{t_0}^t d\tau e^{-i\omega_q(t-\tau)} a(\tau) = \int_{t_0}^t d\tau \frac{\kappa}{2\pi} \int_{-\infty}^{+\infty} d\omega e^{-i\omega(t-\tau)} a(\tau). \quad (\text{A.12})$$

Knowing that

$$\int_{-\infty}^{+\infty} d\omega e^{-i\omega(t-\tau)} = 2\pi \delta(t-\tau), \quad (\text{A.13})$$

then,

$$\sum_q \lambda_q^2 \int_{t_0}^t d\tau e^{-i\omega_q(t-\tau)} a(\tau) = \kappa \int_{t_0}^t d\tau \delta(t-\tau) a(\tau). \quad (\text{A.14})$$

One can convince itself that for our particular case

$$\int_{t_0}^t d\tau \delta(t - \tau) a(\tau) = \frac{1}{2} a(t). \quad (\text{A.15})$$

Then,

$$\dot{a} = \frac{i}{\hbar} [H_{sys}, a] - \sum_q \lambda_q e^{-i\omega_q(t-t_0)} b_q(t_0) - \frac{\kappa}{2} a. \quad (\text{A.16})$$

Still in the Markov approximation, we can simplify the equation by assuming that the density of states can be written as a constant:

$$\rho = \sum_q \delta(\omega - \omega_q), \quad (\text{A.17})$$

and the coupling is also a constant:  $\lambda = \sqrt{\lambda_p^2}$ . Then, the loss rate becomes:

$$\kappa = 2\pi\lambda\rho. \quad (\text{A.18})$$

Finally, we can then write the equation of motion on  $a$  as:

$$\dot{a} = \frac{i}{\hbar} [H_{sys}, a] - \frac{\kappa}{2} a - \sqrt{\kappa} b_{\text{in}}(t), \quad (\text{A.19})$$

with

$$b_{\text{in}}(t) = \frac{1}{\sqrt{2\pi\rho}} \sum_q e^{-i\omega_q(t-t_0)} b_q(t_0). \quad (\text{A.20})$$

We can write a different solution for Eq. (A.6) with the final condition  $t_1 > t$  and rewrite the equation of motion of  $a$  as:

$$\dot{a} = \frac{i}{\hbar} [H_{sys}, a] + \frac{\kappa}{2} a - \sqrt{\kappa} b_{\text{out}}(t), \quad (\text{A.21})$$

with

$$b_{\text{out}}(t) = \frac{1}{\sqrt{2\pi\rho}} \sum_q e^{-i\omega_q(t-t_1)} b_q(t_1). \quad (\text{A.22})$$

Thus we can deduce a simple relation between the input and output fields

$$\boxed{b_{\text{out}}(t) = \sqrt{\kappa} a(t) + b_{\text{in}}(t)}, \quad (\text{A.23})$$

which is very useful to fit the transmission spectrum of the microwave cavity.





# FABRICATION RECIPES

In this Appendix, we give the complete fabrication recipes used in this work.

## B.1 Alignment crossees

- O<sub>2</sub> plasma etching with 500 W ICP and 20 W RF power during 10 s at 20 °C and  $P = 2$  Pa using the ICP from Sentech
- Evaporation of 5 nm Cr and 50 nm of Au or Pt at respectively 0.1 nm s<sup>-1</sup> and 0.25 nm s<sup>-1</sup> using a MEB550 from Plassys
- Lift-off:
  - 10 min ultrasonic bath of ethyl lactate
  - 10 min of ethyl lactate bath at 40 °C
  - 10 min ultrasonic bath of ethyl lactate again
  - 5 min ultrasonic bath of IPA
  - rinse with IPA and then blow dry with N<sub>2</sub>
- O<sub>2</sub> plasma etching to remove the BARC layer with 500 W ICP and 20 W RF power during 12 s at 20 °C and  $P = 2$  Pa using ICP from Sentech

*N.B.:* Cracks may appear in the photoresist after cleaving or the initial ICP etching probably due to mechanical or thermal constrains. A resist reflowing step is then needed before depositing any metal at 210° on a hot plate for 2 min to 5 min depending on the size of the cracks.

## B.2 Resonators fabrication

### B.2.1 NbN depostion

- Substrate temperature : 180 °C kept for one night (~ 16 h)

- Chamber pressure : 0.1 mbar
- Target current : 2 A
- Ar flow : 35 sccm
- N<sub>2</sub> flow : 40%
- Sputtering time : 11 s for 10 nm

### B.2.2 E-beam Lithography

#### Cleaning

- 5 min in acetone in a ultrasonic bath
- 5 min in a new acetone bath with ultrasounds
- 5 min in IPA in a ultrasonic bath
- Rinse with IPA and blow dry

#### Resist coating

- Resist: ZEP 520A diluted with IPA with a one-to-one ratio
- Spin coating parameters: 2000 turn/s with an acceleration of 4000 turns/s<sup>2</sup> for 30 s
- Spin baking: 180° for 5 min

#### E-beam lithography

- Acceleration voltage : 100 kV
- Aperture : 62.5 μm
- Current: 1 nA
- Exposure dose : 280-480 μC/cm<sup>2</sup>

#### Resist development

- 60 s in a MIBK:IPA [1:1] solution
- 20 s in a MIBK:IPA [89:11] solution
- blow dry with N<sub>2</sub>

### B.2.3 Plasma etching

#### Chamber conditioning

The following steps are performed with a clean unpolished Si wafer in the chamber.

**O<sub>2</sub> cleaning (10 min)**

- Pressure: 10 mTorr
- Temperature: 20 °C
- ICP power: 1500 W
- RF power: 100 W
- O<sub>2</sub> rate: 50 sccm

**SF<sub>6</sub> and O<sub>2</sub> purge (2 s):**

- Pressure: 5 mTorr
- Temperature: 20 °C
- ICP power: 0 W
- RF power: 0 W
- O<sub>2</sub> rate: 5 sccm
- SF<sub>6</sub> rate: 10 sccm

**SF<sub>6</sub> and O<sub>2</sub> etch (8 min):**

- Pressure: 5 mTorr
- Temperature: 20 °C
- ICP power: 0 W
- RF power: 50 W
- O<sub>2</sub> rate: 5 sccm
- SF<sub>6</sub> rate: 10 sccm

**Etching****SF<sub>6</sub> and O<sub>2</sub> purge (2 min):**

- Pressure: 5 mTorr
- Temperature: 20 °C
- ICP power: 0 W
- RF power: 0 W
- O<sub>2</sub> rate: 5 sccm
- SF<sub>6</sub> rate: 10 sccm

**SF<sub>6</sub> and O<sub>2</sub> etch (125 s):**

- Pressure: 5 mTorr
- Temperature: 20 °C
- ICP power: 0 W
- RF power: 50 W
- O<sub>2</sub> rate: 5 sccm
- SF<sub>6</sub> rate: 10 sccm

*N.B.:* These parameters correspond to a etch rate of 18 nm/min on NbN and we over-etch on purpose the 10 nm thick NbN layer.

**Chamber Cleaning (10 min)**

- Pressure: 10 mTorr
- Temperature: 20 °C
- ICP power: 1500 W
- RF power: 100 W
- O<sub>2</sub> rate: 50 sccm

**B.2.4 Resist removal**

- 4 min DUV exposure using the UV-Ocleaner from Jelight
- 60 s in MIBK:IPA[1:1]
- 20 s in MIBK:IPA[89:11]
- rinse with IPA and blow dry with nitrogen

**B.2.5 Dicing**

- Protective resist: AZ1512HS (1.2 μm thick)
  - Acceleration: 4000 turns/s<sup>2</sup>
  - Speed: 2000 turns/s
  - Duration: 60 s
  - Baking at 100 ° for 90 s
- Dicing using a diamond saw (DISCO DAD 321)
- Resist removal:
  - 5 min in acetone in a ultrasonic bath
  - 5 min in a new acetone bath with ultrasounds
  - 5 min in IPA in a ultrasonic bath
  - Rinse with IPA and blow dry



### B.2.6 Annealing

- Temperature: 400 °C
- Gas: N<sub>2</sub>/H<sub>2</sub> (4%) with continuous gas circulation
- Duration: 1 h



# KINETIC INDUCTANCE EXTRACTION BY TWO-TONE SPECTROSCOPY

In this Appendix, we will present a two-tone spectroscopy on a low-resonance frequency resonator to extract the kinetic inductance of the NbN film. This method relies on measuring the dispersion relation of a resonator whose resonance frequency is set intentionally low, here  $f_0 = 750$  MHz. This allows to probe a large number of its harmonics. An optical microscope image of the resonator is shown in Fig. 3.1.(b). The geometry of the resonator differs from the ones from Chap. 3 because its length is much longer with  $\ell = 22$  mm and only a single resonator is measured to avoid cross-talks between the harmonics with another resonator. The dimension of the CPW is  $w = 50$   $\mu\text{m}$  and  $s = 2$   $\mu\text{m}$ . The central conductor is coupled via gap-capacitors to the input and output transmission lines with a gap width of 10  $\mu\text{m}$  [57].

To map the dispersion relation, a VNA is set to measure the transmission at a resonant frequency of the resonator  $f_{\text{VNA}}$  within the 4-8 GHz band of our measurement setup. We then sweep a second tone at a frequency  $f_{\text{MW}}$  and whenever that second tone matches a harmonic of the resonator, at a frequency  $f_n$ , the measured resonance at  $f_{\text{VNA}}$  is dispersively shifted by the cross-Kerr effect[133] and the transmission readout by the VNA is modified. By identifying all  $f_n$ , the dispersion relation can be reconstructed. In Fig. 3.1.(b) we show the dispersion relation for a probe frequency  $f_{\text{VNA}} = 5.22$  GHz, the seventh harmonic of the resonator. Since the angular wavenumber of each resonance is given by  $k_n = \pi n/\ell$  where  $\ell$  is the length of the  $\lambda/2$  resonator and  $n$  is the mode index, we can extract the kinetic inductance as follows:



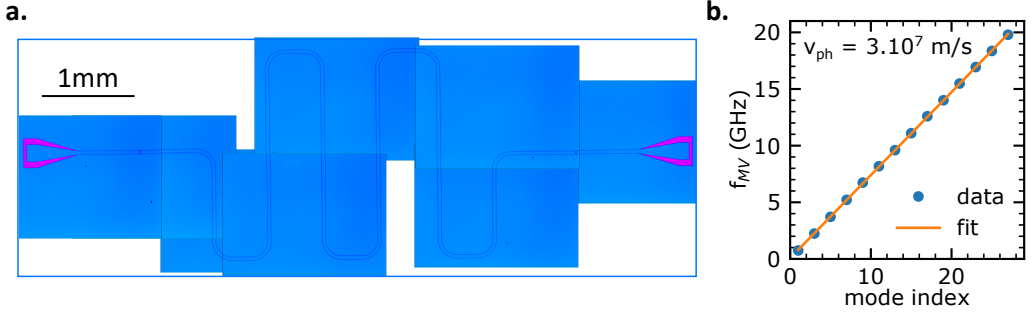


Figure 3.1 – Two-tone measurement to extract the kinetic inductance of the NbN film. (a) Optical microscope image of a resonator capacitively connected to the RF ports with a resonance frequency of 570 MHz. (b) Dispersion relation of the resonator shown in (a) probed by two-tone spectroscopy. Only half of the data points used to extract the phase velocity are plotted.

$$v_{\text{ph}} = \frac{\omega_n}{k_n} = \frac{1}{\sqrt{C_\ell(L_\ell^m + L_\ell^{\text{kin}})}}, \quad (\text{C.1})$$

where  $\omega_n = 2\pi f_n$  is the angular resonance frequency,  $C_\ell$  is the capacitance per unit length and  $L_\ell^m$ ,  $L_\ell^{\text{kin}}$  are the geometric and the kinetic inductance per unit length respectively.  $L_\ell^m$  and  $C_\ell$  are purely geometrical quantities and can be estimated using a microwave simulation software like Sonnet ( $L_\ell^m = 2.13 \times 10^{-7} \text{ H m}^{-1}$  and  $C_\ell = 2.82 \times 10^{-10} \text{ F m}^{-1}$ ) or conformal mapping calculations[131] ( $L_\ell^m = 2.13 \times 10^{-7} \text{ H m}^{-1}$  and  $C_\ell = 3.13 \times 10^{-10} \text{ F m}^{-1}$ ).

From this RF measurement and Sonnet simulations data we obtained a kinetic inductance value  $L_\ell^{\text{kin}} = 3.84 \times 10^{-6} \text{ H m}^{-1}$  corresponding to  $L_{\text{kin}} = 192 \pm 3 \text{ pH } \square^{-1}$ , which is in excellent agreement with the DC measurement extraction.

# Appendix D

## AVERAGE NUMBER OF PHOTONS IN A $\lambda/2$ RESONATOR

In this appendix, we derive the internal average photon number of a resonator driven by an external drive as stated in Eq. 4 of the main paper.

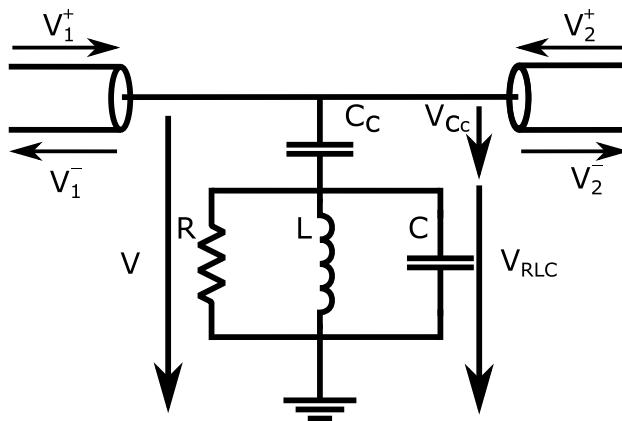


Figure 4.1 – Electrical circuit model of a parallel resonator, as a RLC circuit, coupled to a feedline via a coupling capacitor  $C_c$ .

As shown in Ref [117] section 6.2, a low loss  $\lambda/2$  resonator may be described as a parallel RLC resonator at frequencies close to its resonance frequency. From there we also assume a purely capacitive coupling between the resonator and its feedline, an assumption justified by the electro-magnetic field distribution along the resonator and the position of the resonator in respect to the feedline. The resulting circuit model is shown in Fig. 4.1.

From Ref. [117], Eq. 6.14.b, the average electric energy stored in the capacitor

$C$  is

$$W_e = \frac{1}{4}C|V_{\text{RLC}}|^2. \quad (\text{D.1})$$

The aim of this section is to derive an expression of  $W_e$  as a function of the resonator resonance frequency  $\omega_r$ , its internal quality factor  $Q_i$  and its coupling quality factor  $Q_c$ , all of them being accessible through fitting of the resonance spectrum.

## D.1 Derivation of $V_{\text{RLC}}$

From Ohm's law we have

$$V_{\text{RLC}} = Z_{\text{RLC}}I. \quad (\text{D.2})$$

Using the Kirchhoff's second law, we can calculate the applied current as

$$V = V_{C_c} + V_{\text{RLC}}, \quad (\text{D.3})$$

$$V = I(Z_{C_c} + Z_{\text{RLC}}), \quad (\text{D.4})$$

$$I = \frac{V}{Z_{C_c} + Z_{\text{RLC}}}. \quad (\text{D.5})$$

From which the voltage reads

$$V_{\text{RLC}} = \frac{Z_{\text{RLC}}}{Z_{C_c} + Z_{\text{RLC}}}V. \quad (\text{D.6})$$

From Ref. [117] Eq. 4.41, we know that:

$$V_2^- = S_{21}V_1^+, \quad (\text{D.7})$$

$$V = S_{21}V_1^+. \quad (\text{D.8})$$

By injecting Eq. D.8 to Eq. D.6, we obtain

$$V_{\text{RLC}} = \frac{Z_{\text{RLC}}}{Z_{C_c} + Z_{\text{RLC}}}S_{21}V_1^+. \quad (\text{D.9})$$

Finally, the average energy can be written as

$$W_e = \frac{1}{4}C \left| \frac{Z_{\text{RLC}}}{Z_{C_c} + Z_{\text{RLC}}} \right|^2 |S_{21}|^2 |V_1^+|^2. \quad (\text{D.10})$$

The input power of the system is, from Ref. [117] Eq. 6.13,

$$P_{\text{in}} = \frac{1}{2} \frac{|V_1^+|^2}{Z_0}. \quad (\text{D.11})$$

By using Eq. D.11 in Eq. D.10, we obtain

$$W_e = \frac{Z_0}{2}C \left| \frac{Z_{\text{RLC}}}{Z_{C_c} + Z_{\text{RLC}}} \right|^2 |S_{21}|^2 P_{\text{in}}. \quad (\text{D.12})$$

## D.2 Derivation of resonator impedance

The impedance of an open-circuited  $\lambda/2$  resonator is given by Ref. [117] Eq. 6.33 and we will express it through its internal quality factor, see Ref. [117], Eq. 6.35, as

$$Z_{\text{RLC}} = \frac{Z_r}{\frac{\pi}{2} \frac{1}{Q_i} + i\pi \frac{\Delta\omega_r}{\omega_r}}, \quad (\text{D.13})$$

with  $Z_r$ , the resonator characteristic impedance and  $\Delta\omega_r = \omega - \omega_r$ , the drive frequency relative to the resonance frequency. We rewrite the previous equation by separating the real and imaginary part

$$Z_{\text{RLC}} = Z_r \frac{2Q_i}{\pi} \frac{1 - i2Q_i \Delta\omega_r/\omega_r}{1 + 4Q_i^2 \left(\frac{\Delta\omega_r}{\omega_r}\right)^2}. \quad (\text{D.14})$$

## D.3 The resonance shift

While the bare resonator resonates at a frequency  $\omega_r$  the resonator coupled to a feedline does so at a frequency  $\omega_0$ , lower than  $\omega_r$ . In this section we derive  $\Delta\omega_0/\omega_0$  the drive frequency relative to the resonance of the resonator coupled to the feedline. The total impedance is

$$Z_{\text{tot}} = Z_r \frac{2Q_i}{\pi} \frac{1 - i2Q_i \Delta\omega_r/\omega_r}{1 + 4Q_i^2 \left(\frac{\Delta\omega_r}{\omega_r}\right)^2} - \frac{i}{\omega C_c}, \quad (\text{D.15})$$

$$Z_{\text{tot}} = Z_r \frac{\frac{2Q_i}{\pi} - i \left( \frac{4Q_i^2}{\pi} \frac{\Delta\omega_r}{\omega_r} + \frac{1}{\omega Z_r C_c} \left[ 1 + 4Q_i^2 \left(\frac{\Delta\omega_r}{\omega_r}\right)^2 \right] \right)}{1 + 4Q_i^2 \left(\frac{\Delta\omega_r}{\omega_r}\right)^2}. \quad (\text{D.16})$$

At resonance, the imaginary part of the impedance is equal to zero which leads to

$$\frac{4Q_i^2}{\omega_0 Z_r C_c} \left(\frac{\Delta\omega_r}{\omega_r}\right)^2 + \frac{4Q_i^2}{\pi} \frac{\Delta\omega_r}{\omega_r} + \frac{1}{\omega_0 Z_r C_c} = 0. \quad (\text{D.17})$$

Assuming<sup>1</sup> that  $Q_i^2/\pi^2 \gg 1/\omega^2 Z_r^2 C_c^2$ , the roots of the equation are

$$\left(\frac{\Delta\omega_r}{\omega_r}\right)_{\pm} = \frac{\omega_0 Z_r C_c}{2Q_i} \left(-\frac{Q_i}{\pi} \pm \frac{Q_i}{\pi}\right). \quad (\text{D.18})$$

The only physical solution is the one lowering the resonance frequency which is consistent with adding the coupling capacitor in series with the resonator. From this we define the drive frequency relative to the resonance of the coupled resonator as

$$\frac{\Delta\omega_0}{\omega_0} = \frac{\Delta\omega_r}{\omega_r} + \frac{\omega_0 Z_r C_c}{\pi}. \quad (\text{D.19})$$

1. By substituting  $C_c$  using Eq. D.26, this assumption is equivalent to  $Q_i^2/Q_c^2 \gg \pi^2 Z_0/Z_r$  which is often the case in cQED experiment with under-coupled resonators.

## D.4 Coupling quality factor

At resonance, the total impedance is, from Eq. D.16,

$$Z_{\text{tot}} = Z_r \frac{2Q_i}{\pi} \frac{1}{1 + 4Q_i^2 \left(\frac{\Delta\omega_r}{\omega_r}\right)^2}. \quad (\text{D.20})$$

To which we substitute Eq. D.19, leading to

$$Z_{\text{tot}} = Z_r \frac{2Q_i}{\pi} \frac{\pi^2}{\pi^2 + 4Q_i^2 \omega^2 Z_r^2 C_c^2}. \quad (\text{D.21})$$

Assuming  $\pi \ll 4Q_i^2 \omega^2 Z_r^2 C_c^2$  :

$$Z_{\text{tot}} \approx \frac{\pi}{2Q_i \omega^2 Z_r C_c^2}, \quad (\text{D.22})$$

This assumption require a quality factor  $\gg 10^3$  for giga-hertz  $50 \Omega$  resonators and a lower quality factor for higher impedances. In practice, for superconducting resonators used in typical cQED experiments this assumption is often verified.

From Ref. [117], Table 4.2, we write the transmission coefficient as

$$S_{21} = \frac{2}{2 + \frac{Z_0}{Z_{\text{tot}}}} \quad (\text{D.23})$$

$$S_{21} = \frac{2\pi}{2\pi + 2Q_i \omega^2 Z_r C_c^2 Z_0}. \quad (\text{D.24})$$

At resonance, the transmission reaches a minimum

$$S_{21}^{\text{res}} = \frac{Q_c}{Q_c + Q_i}, \quad (\text{D.25})$$

which allows us to derive the coupling quality factor by identification as

$$Q_c = \frac{\pi}{\omega^2 Z_r C_c^2 Z_0}. \quad (\text{D.26})$$

## D.5 Average number of photons in a $\lambda/2$ resonator

Substituting Eq. D.26 in Eq. D.19 and in Eq. D.14, we can write the resonator impedance at resonance frequency as

$$Z_{\text{RLC}} = Z_r \frac{2Q_i}{\pi} \frac{1}{1 - 2Q_i \sqrt{\frac{Z_r}{\pi Z_0 Q_c}}}. \quad (\text{D.27})$$

Assuming  $1 \ll 2Q_i \sqrt{\frac{Z_r}{\pi Z_0 Q_c}}$  which is often true in cQED experiments where the resonator is under-coupled with  $Q_i \gg Q_c$  :

$$Z_{\text{RLC}} \approx -\sqrt{\frac{Z_r Z_0 Q_c}{\pi}}. \quad (\text{D.28})$$

Rearranging Eq. D.23 we obtain

$$\frac{1}{Z_{C_c} + Z_{RLC}} = \frac{2}{Z_0} \left( \frac{1}{S_{21}} - 1 \right). \quad (\text{D.29})$$

The capacitance of the  $\lambda/2$  resonator is, see Ref. [117] Eq.6.34.b,

$$C = \frac{\pi}{2Z_r\omega_r}. \quad (\text{D.30})$$

Substituting Eq. D.25, Eq. D.28, Eq. D.29, Eq. D.30, and in Eq. D.12 we finally obtain

$$W_e = \frac{Q_c}{\omega_0} \left( \frac{Q_i}{Q_i + Q_c} \right)^2 P_{in}. \quad (\text{D.31})$$

From which we deduce the average internal photon number in the resonator as

$$\langle n_{\text{photons}} \rangle = \frac{Q_c}{\omega_0} \left( \frac{Q_i}{Q_i + Q_c} \right)^2 \frac{P_{in}}{\hbar\omega_0}, \quad (\text{D.32})$$

with  $P$  the input power in Watt, the quality factors  $Q_c$ ,  $Q_i$ , the resonance frequency  $\omega_0$  and the reduced Planck constant  $\hbar$ .



# PUBLICATIONS

1. YU, C. X., ZIHLMANN, S., ABADILLO-URIEL, J. C., MICHAL, V. P., RAMBAL, N., NIEBOJEWSKI, H., BEDECARRATS, T., VINET, M., DUMUR, E., FILIPPONE, M., ET AL. Strong coupling between a photon and a hole spin in silicon. *arXiv preprint arXiv:2206.14082* (2022)
2. YU, C., ZIHLMANN, S., BERTRAND, B., AND MAURAND, R. Si hole qubits in a cqcd architecture. *Bulletin of the American Physical Society* 67 (2022)
3. YU, C. X., ZIHLMANN, S., TRONCOSO FERNÁNDEZ-BADA, G., THOMASSIN, J.-L., DUMUR, É., MAURAND, R., AND TRONCOSO, G. Magnetic field resilient high kinetic inductance superconducting niobium nitride coplanar waveguide resonators. *Applied Physics Letters* 118, 054001 (2021)
4. NIQUET, Y. M., HUTIN, L., DIAZ, B. M., VENITUCCI, B., LI, J., MICHAL, V., FERNÁNDEZ-BADA, G. T., JACQUINOT, H., AMISSE, A., APRA, A., EZZOUCH, R., PIOT, N., VINCENT, E., YU, C., ZIHLMANN, S., BRUNBARRIÈRE, B., SCHMITT, V., DUMUR, E., MAURAND, R., JEHL, X., SANQUER, M., BERTRAND, B., RAMBAL, N., NIEBOJEWSKI, H., BEDECARRATS, T., CASSÉ, M., CATAPANO, E., MORTEMOUSQUE, P. A., THOMAS, C., THONNART, Y., BILLIOT, G., MOREL, A., CHARBONNIER, J., PALLEGOIX, L., NIEGEMANN, D., KLEMT, B., URDAMPILLETA, M., EL HOMSY, V., NURIZZO, M., CHANRION, E., JADOT, B., SPENCE, C., THINEY, V., PAZ, B., DE FRANCESCHI, S., VINET, M., AND MEUNIER, T. Challenges and perspectives in the modeling of spin qubits. In *2020 IEEE International Electron Devices Meeting (IEDM)* (2020), pp. 30.1.1–30.1.4





# BIBLIOGRAPHY

- [1] ABDO, B., SEGEV, E., SHTEMPLUCK, O., AND BUKS, E. Nonlinear dynamics in the resonance line shape of NbN superconducting resonators. *Phys. Rev. B* 73 (Apr 2006), 134513. 59
- [2] ABUWASIB, M., KRANTZ, P., AND DELSING, P. Fabrication of large dimension aluminum air-bridges for superconducting quantum circuits. *Journal of Vacuum Science & Technology B* 31, 3 (2013), 031601. 68
- [3] AHMED, I., HAIGH, J. A., SCHAAL, S., BARRAUD, S., ZHU, Y., LEE, C.-M., AMADO, M., ROBINSON, J. W. A., ROSSI, A., MORTON, J. J. L., AND GONZALEZ-ZALBA, M. F. Radio-frequency capacitive gate-based sensing. *Phys. Rev. Applied* 10 (Jul 2018), 014018. 83
- [4] AMIN, K. R., LADNER, C., JOURDAN, G., HENTZ, S., ROCH, N., AND RENARD, J. Loss mechanisms in tin high impedance superconducting microwave circuits. *Applied Physics Letters* 120, 16 (2022), 164001. 9
- [5] AMIRZADA, M. R., TATZEL, A., VIERECK, V., AND HILLMER, H. Surface roughness analysis of sio2 for pecvd, pvd and ibd on different substrates. *Applied Nanoscience* 6 (2016), 215–222. 63
- [6] ANTONOVA, E. A., DZHURAEV, D. R., MOTULEVICH, G. P., AND SUKHOV, V. A. Superconducting energy gap of niobium nitride. *Soviet Physics - JETP* 53, 6 (1981), 1270–1271. 42
- [7] ARES, N., GOLOVACH, V. N., KATSAROS, G., STOFFEL, M., FOURNEL, F., GLAZMAN, L. I., SCHMIDT, O. G., AND DE FRANCESCHI, S. Nature of tunable hole  $g$  factors in quantum dots. *Phys. Rev. Lett.* 110 (Jan 2013), 046602. 92
- [8] ARUTE, F., ARYA, K., BABBUSH, R., BACON, D., BARDIN, J. C., BARENDS, R., BISWAS, R., BOIXO, S., BRANDAO, F. G., BUELL, D. A., ET AL. Quantum supremacy using a programmable superconducting processor. *Nature* 574, 7779 (2019), 505–510. 1, 2
- [9] ASTAFIEV, O., IOFFE, L., KAFANOV, S., PASHKIN, Y. A., ARUTYUNOV, K. Y., SHAHAR, D., COHEN, O., AND TSAI, J. S. Coherent quantum phase slip. *Nature* 484, 7394 (2012), 355–358. 9

- [10] BANERJEE, A. *Optimisation of superconducting thin film growth for next generation superconducting detector applications*. PhD thesis, University of Glasgow, 2017. [40](#)
- [11] BARRAUD, S., COQUAND, R., CASSE, M., KOYAMA, M., HARTMANN, J.-M., MAFFINI-ALVARO, V., COMBOROURE, C., VIZIOZ, C., AUSSENAC, F., FAYNOT, O., AND POIROUX, T. Performance of omega-shaped-gate silicon nanowire mosfet with diameter down to 8 nm. *IEEE Electron Device Letters* *33*, 11 (2012), 1526–1528. [34](#), [83](#)
- [12] BASSET, J., JARAUSCH, D.-D., STOCKKLAUSER, A., FREY, T., REICHL, C., WEGSCHEIDER, W., IHN, T. M., ENSSLIN, K., AND WALLRAFF, A. Single-electron double quantum dot dipole-coupled to a single photonic mode. *Phys. Rev. B* *88* (Sep 2013), 125312. [78](#)
- [13] BEAUDOIN, F., LACHANCE-QUIRION, D., COISH, W., AND PIORO-LADRIÈRE, M. Coupling a single electron spin to a microwave resonator: controlling transverse and longitudinal couplings. *Nanotechnology* *27*, 46 (2016), 464003. [28](#)
- [14] BENITO, M., MI, X., TAYLOR, J. M., PETTA, J. R., AND BURKARD, G. Input-output theory for spin-photon coupling in si double quantum dots. *Phys. Rev. B* *96* (Dec 2017), 235434. [29](#), [89](#)
- [15] BENITO, M., PETTA, J. R., AND BURKARD, G. Optimized cavity-mediated dispersive two-qubit gates between spin qubits. *Phys. Rev. B* *100* (Aug 2019), 081412. [4](#), [106](#)
- [16] BIENFAIT, A., PLA, J., KUBO, Y., ZHOU, X., STERN, M., LO, C., WEIS, C., SCHENKEL, T., VION, D., ESTEVE, D., ET AL. Controlling spin relaxation with a cavity. *Nature* *531*, 7592 (2016), 74–77. [4](#)
- [17] BLAIS, A., GRIMSMO, A. L., GIRVIN, S. M., AND WALLRAFF, A. Circuit quantum electrodynamics. *Rev. Mod. Phys.* *93* (May 2021), 025005. [2](#), [3](#), [12](#), [17](#), [105](#)
- [18] BLAIS, A., HUANG, R.-S., WALLRAFF, A., GIRVIN, S. M., AND SCHOELKOPF, R. J. Cavity quantum electrodynamics for superconducting electrical circuits: An architecture for quantum computation. *Phys. Rev. A* *69* (Jun 2004), 062320. [2](#)
- [19] BOISSONNEAULT, M., GAMBETTA, J. M., AND BLAIS, A. Dispersive regime of circuit qed: Photon-dependent qubit dephasing and relaxation rates. *Phys. Rev. A* *79* (Jan 2009), 013819. [15](#)
- [20] BORJANS, F., CROOT, X. G., MI, X., GULLANS, M. J., AND PETTA, J. R. Long-Range Microwave Mediated Interactions Between Electron Spins. *Nature* *577* (2020), 195–198. [30](#), [103](#), [105](#)
- [21] BOSCO, S., SCARLINO, P., KLINOVAJA, J., AND LOSS, D. Fully tunable longitudinal spin-photon interactions in si and ge quantum dots. *arXiv 2203.17163* (2022). [28](#), [100](#), [103](#), [106](#)

- [22] BULAEV, D. V., AND LOSS, D. Spin relaxation and decoherence of holes in quantum dots. *Phys. Rev. Lett.* *95* (Aug 2005), 076805. [30](#)
- [23] BULAEV, D. V., AND LOSS, D. Electric dipole spin resonance for heavy holes in quantum dots. *Phys. Rev. Lett.* *98* (Feb 2007), 097202. [3, 30](#)
- [24] BURKARD, G., AND IMAMOGLU, A. Ultra-long-distance interaction between spin qubits. *Phys. Rev. B* *74* (Jul 2006), 041307. [29](#)
- [25] BURNETT, J., SAGAR, J., KENNEDY, O. W., WARBURTON, P. A., AND FENTON, J. C. Low-loss superconducting nanowire circuits using a neon focused ion beam. *Phys. Rev. Applied* *8* (Jul 2017), 014039. [59](#)
- [26] BØTTCHER, C. G. L., HARVEY, S. P., FALLAHI, S., GARDNER, G. C., MANFRA, M. J., VOOL, U., BARTLETT, S. D., AND YACOBY, A. Parametric longitudinal coupling between a high-impedance superconducting resonator and a semiconductor quantum dot singlet-triplet spin qubit, 2021. [106](#)
- [27] CHEN, F., SIROIS, A., SIMMONDS, R., AND RIMBERG, A. Introduction of a dc bias into a high-q superconducting microwave cavity. *Applied Physics Letters* *98*, 13 (2011), 132509. [66](#)
- [28] CHEN, Z., MEGRANT, A., KELLY, J., BARENDTS, R., BOCHMANN, J., CHEN, Y., CHIARO, B., DUNSWORTH, A., JEFFREY, E., MUTUS, J. Y., O'MALLEY, P. J. J., NEILL, C., ROUSHAN, P., SANK, D., VAINSENER, A., WENNER, J., WHITE, T. C., CLELAND, A. N., AND MARTINIS, J. M. Fabrication and characterization of aluminum airbridges for superconducting microwave circuits. *Applied Physics Letters* *104*, 5 (2014), 052602. [68](#)
- [29] CHILDRESS, L., SØRENSEN, A. S., AND LUKIN, M. D. Mesoscopic cavity quantum electrodynamics with quantum dots. *Phys. Rev. A* *69* (Apr 2004), 042302. [9, 23](#)
- [30] CHOCKALINGAM, S. P., CHAND, M., JESUDASAN, J., TRIPATHI, V., AND RAYCHAUDHURI, P. Superconducting properties and hall effect of epitaxial nbn thin films. *Phys. Rev. B* *77* (Jun 2008), 214503. [44](#)
- [31] CHOW, J., DIAL, O., AND GAMBETTA, J. Ibm quantum breaks the 100-qubit processor barrier. *IBM Research Blog* (2021). [2](#)
- [32] CLARKE, J., AND WILHELM, F. K. Superconducting quantum bits. *Nature* *453*, 7198 (2008), 1031–1042. [2](#)
- [33] CLERK, A. A., LEHNERT, K. W., BERTET, P., PETTA, J. R., AND NAKAMURA, Y. Hybrid quantum systems with circuit quantum electrodynamics. *Nature Physics* *16*, 3 (2020), 257–267. [12, 93](#)
- [34] COHEN-TANNOUJDI, C., DIU, B., AND LALOË, F. *Quantum mechanics; 1st ed.* Wiley, New York, NY, 1977. Trans. of : Mécanique quantique. Paris : Hermann, 1973. [14](#)
- [35] CORNA, A. *Single spin control and readout in silicon coupled quantum dots.* PhD thesis, Université Grenoble Alpes, 2017. [36](#)

- [36] COTTET, A., AND KONTOS, T. Spin quantum bit with ferromagnetic contacts for circuit qed. *Phys. Rev. Lett.* *105* (Oct 2010), 160502. [29](#)
- [37] CRIPPA, A., EZZOUCH, R., APRÁ, A., AMISSE, A., LAVIÉVILLE, R., HUTIN, L., BERTRAND, B., VINET, M., URDAMPILLETA, M., MEUNIER, T., SANQUER, M., JELH, X., MAURAND, R., AND DE FRANCESCHI, S. Gate-reflectometry dispersive readout and coherent control of a spin qubit in silicon. *Nature Communications* *8*, 10 (2019). [83](#)
- [38] CRIPPA, A., MAURAND, R., BOURDET, L., KOTEKAR-PATIL, D., AMISSE, A., JEHL, X., SANQUER, M., LAVIÉVILLE, R., BOHUSLAVSKYI, H., HUTIN, L., BARRAUD, S., VINET, M., NIQUET, Y.-M., AND DE FRANCESCHI, S. Electrical spin driving by  $g$ -matrix modulation in spin-orbit qubits. *Phys. Rev. Lett.* *120* (Mar 2018), 137702. [25](#), [29](#), [89](#)
- [39] D'ANJOU, B., AND BURKARD, G. Optimal dispersive readout of a spin qubit with a microwave resonator. *Phys. Rev. B* *100* (Dec 2019), 245427. [4](#), [106](#)
- [40] DELBECQ, M. *Coupling quantum dot circuits to microwave cavities*. PhD thesis, Université Paris VI, 2012. [23](#)
- [41] DUPRÉ, O., BENOÎT, A., CALVO, M., CATALANO, A., GOUPY, J., HOARRAU, C., KLEIN, T., LE CALVEZ, K., SACÉPÉ, B., MONFARDINI, A., ET AL. Tunable sub-gap radiation detection with superconducting resonators. *Superconductor Science and Technology* *30*, 4 (2017), 045007. [9](#)
- [42] ENGEL, A., INDERBITZIN, K., SCHILLING, A., LUSCHE, R., SEMENOV, A., HÜBERS, H., HENRICH, D., HOFHERR, M., IL'IN, K., AND SIEGEL, M. Temperature-dependence of detection efficiency in nbn and tan snspd. *IEEE Transactions on Applied Superconductivity* *23*, 3 (2013), 2300505–2300505. [60](#)
- [43] EZZOUCH, R. *Gate reflectometry as readout and spectroscopy tool for silicon spin qubits*. PhD thesis, Université Grenoble Alpes, 2021. [19](#)
- [44] FAN, S., KOCABAŞ, I. M. C. E., AND SHEN, J.-T. Input-output formalism for few-photon transport in one-dimensional nanophotonic waveguides coupled to a qubit. *Phys. Rev. A* *82* (Dec 2010), 063821. [107](#)
- [45] FEYNMAN, R. P. Simulating physics with computers. *International journal of theoretical physics* *21* (1982), 467–488. [1](#)
- [46] FOWLER, A. G., MARIANTONI, M., MARTINIS, J. M., AND CLELAND, A. N. Surface codes: Towards practical large-scale quantum computation. *Phys. Rev. A* *86* (Sep 2012), 032324. [2](#), [34](#)
- [47] FREY, T., LEEK, P. J., BECK, M., BLAIS, A., IHN, T., ENSSLIN, K., AND WALLRAFF, A. Dipole coupling of a double quantum dot to a microwave resonator. *Phys. Rev. Lett.* *108* (Jan 2012), 046807. [3](#), [23](#)
- [48] FRISK KOCKUM, A., MIRANOWICZ, A., DE LIBERATO, S., SAVASTA, S., AND NORI, F. Ultrastrong coupling between light and matter. *Nature Reviews Physics* *1*, 1 (2019), 19–40. [15](#), [83](#)

- [49] FRONING, F. N., CAMENZIND, L. C., VAN DER MOLEN, O. A., LI, A., BAKKERS, E. P., ZUMBÜHL, D. M., AND BRAAKMAN, F. R. Ultrafast hole spin qubit with gate-tunable spin-orbit switch functionality. *Nature Nanotechnology* 16, 3 (2021), 308–312. [28](#)
- [50] GAO, J. *The physics of superconducting microwave resonators*. PhD thesis, California Institute of Technology, 2008. [8](#), [9](#)
- [51] GEERLINGS, K. L. *Improving Coherence of Superconducting qubits and Resonators*. PhD thesis, Yale University, 2013. [74](#)
- [52] GEYER, S., CAMENZIND, L. C., CZORNOMAZ, L., DESHPANDE, V., FUHRER, A., WARBURTON, R. J., ZUMBÜHL, D. M., AND KUHLMANN, A. V. Self-aligned gates for scalable silicon quantum computing. *Applied Physics Letters* 118, 10 (2021). [35](#)
- [53] GLOWACKA, D. M., GOLDIE, D. J., WITHINGTON, S., MUHAMMAD, H., AND YASSIN, G. Development of a nbn deposition process for superconducting quantum sensors. [40](#)
- [54] GOLOVACH, V. N., BORHANI, M., AND LOSS, D. Electric-dipole-induced spin resonance in quantum dots. *Phys. Rev. B* 74 (Oct 2006), 165319. [3](#), [23](#)
- [55] GRIMM, A., JEBARI, S., HAZRA, D., BLANCHET, F., GUSTAVO, F., THOMASSIN, J.-L., AND HOFHEINZ, M. A self-aligned nano-fabrication process for vertical NbN–MgO–NbN josephson junctions. *Superconductor Science and Technology* 30, 10 (aug 2017), 105002. [40](#)
- [56] GRÜNHAUPT, L., SPIECKER, M., GUSENKOVA, D., MALEEVA, N., SKACEL, S. T., TAKMAKOV, I., VALENTI, F., WINKEL, P., ROTZINGER, H., WERNSDORFER, W., USTINOV, A. V., AND POP, I. M. Granular aluminium as a superconducting material for high-impedance quantum circuits. *Nature Materials* 18, August (2019), 816–819. [9](#)
- [57] GÖPPL, M., FRAGNER, A., BAUR, M., BIANCHETTI, R., FILIPP, S., FINK, J. M., LEEK, P. J., PUEBLA, G., STEFFEN, L., AND WALLRAFF, A. Coplanar waveguide resonators for circuit quantum electrodynamics. *Journal of Applied Physics* 104, 11 (2008), 113904. [9](#), [117](#)
- [58] HA, W., HA, S. D., CHOI, M. D., TANG, Y., SCHMITZ, A. E., LEVENDORF, M. P., LEE, K., CHAPPELL, J. M., ADAMS, T. S., HULBERT, D. R., ACUNA, E., NOAH, R. S., MATTEN, J. W., JURA, M. P., WRIGHT, J. A., RAKHER, M. T., AND BORSELLI, M. G. A flexible design platform for si/sige exchange-only qubits with low disorder. *Nano Letters* 22, 3 (2022), 1443–1448. PMID: 34806894. [34](#)
- [59] HANSON, R., KOUWENHOVEN, L. P., PETTA, J. R., TARUCHA, S., AND VANDERSYPEN, L. M. Spins in few-electron quantum dots. *Reviews of Modern Physics* 79, 4 (2007), 1217–1265. [17](#), [22](#)
- [60] HAROCHE, S., AND RAIMOND, J.-M. *Exploring the quantum: atoms, cavities, and photons*. Oxford university press, 2006. [2](#)

- [61] HARVEY-COLLARD, P., DIJKEMA, J., ZHENG, G., SAMMAK, A., SCAPPUCCI, G., AND VANDERSYPEN, L. M. K. Circuit quantum electrodynamics with two remote electron spins, 2021. [30](#), [103](#), [105](#)
- [62] HARVEY-COLLARD, P., ZHENG, G., DIJKEMA, J., SAMKHARADZE, N., SAMMAK, A., SCAPPUCCI, G., AND VANDERSYPEN, L. M. K. On-chip microwave filters for high-impedance resonators with gate-defined quantum dots. *Phys. Rev. Applied* *14* (Sep 2020), 034025. [65](#), [66](#), [103](#), [106](#)
- [63] HENDRICKX, N. W., LAWRIE, W. I., RUSS, M., VAN RIGGELEN, F., DE SNOO, S. L., SCHOUTEN, R. N., SAMMAK, A., SCAPPUCCI, G., AND VELDHORST, M. A four-qubit germanium quantum processor. *Nature* *591*, 7851 (2021), 580–585. [3](#)
- [64] HUANG, W., YANG, C., CHAN, K., TANTTU, T., HENSEN, B., LEON, R., FOGARTY, M., HWANG, J., HUDSON, F., ITOH, K. M., ET AL. Fidelity benchmarks for two-qubit gates in silicon. *Nature* *569*, 7757 (2019), 532–536. [3](#)
- [65] HUTIN, L., BERTRAND, B., MAURAND, R., CRIPPA, A., URDAMPILLETA, M., KIM, Y., AMISSE, A., BOHUSLAVSKYI, H., BOURDET, L., BARRAUD, S., JEH, X., NIQUET, Y.-M., SANQUER, M., BÄUERLE, C., MEUNIER, T., DE FRANCESCHI, S., AND VINET, M. Si mos technology for spin-based quantum computing. In *2018 48th European Solid-State Device Research Conference (ESSDERC)* (2018), pp. 12–17. [34](#)
- [66] IMAMOG̃LU, A., AWSCHALOM, D. D., BURKARD, G., DIVINCENZO, D. P., LOSS, D., SHERWIN, M., AND SMALL, A. Quantum information processing using quantum dot spins and cavity qed. *Phys. Rev. Lett.* *83* (Nov 1999), 4204–4207. [4](#)
- [67] JAYNES, E. T., AND CUMMINGS, F. W. Comparison of Quantum and Semi-classical Radiation theories with Application to the beam maser. *Proceedings of the IEEE* *51*, 1 (1963), 89–109. [12](#)
- [68] JENNEWEIN, T., SIMON, C., WEIHS, G., WEINFURTER, H., AND ZEILINGER, A. Quantum cryptography with entangled photons. *Phys. Rev. Lett.* *84* (May 2000), 4729–4732. [1](#)
- [69] JOHANSSON, J., NATION, P., AND NORI, F. Qutip 2: A python framework for the dynamics of open quantum systems. *Computer Physics Communications* *184*, 4 (2013), 1234–1240. [16](#)
- [70] JOHN, V. Circuit quantum electrodynamics with silicon hole spin qubits. Master thesis, University Grenoble Alpes, 2021. [50](#)
- [71] JUANG, J.-Y., RUDMAN, D., VAN DOVER, R., SINCLAIR, W., AND BACON, D. Dependence of the upper critical field and critical current on resistivity in nbn thin films. 651–658. [44](#)
- [72] KAMLAPURE, A., MONDAL, M., CHAND, M., MISHRA, A., JESUDASAN, J., BAGWE, V., BENFATTO, L., TRIPATHI, V., AND RAYCHAUDHURI, P.

- Measurement of magnetic penetration depth and superconducting energy gap in very thin epitaxial nbn films. *Applied Physics Letters* 96, 7 (2010), 072509. [44](#), [62](#)
- [73] KLOEFFEL, C., RANČIĆ, M. J., AND LOSS, D. Direct rashba spin-orbit interaction in si and ge nanowires with different growth directions. *Phys. Rev. B* 97 (Jun 2018), 235422. [28](#), [29](#), [103](#)
- [74] KLOEFFEL, C., TRIF, M., STANO, P., AND LOSS, D. Circuit qed with hole-spin qubits in ge/si nanowire quantum dots. *Phys. Rev. B* 88 (Dec 2013), 241405. [4](#)
- [75] KNEHR, E., KUZMIN, A., VODOLAZOV, D. Y., ZIEGLER, M., DOERNER, S., ILIN, K., SIEGEL, M., STOLZ, R., AND SCHMIDT, H. Nanowire single-photon detectors made of atomic layer-deposited niobium nitride. *Superconductor Science and Technology* 32, 12 (oct 2019), 125007. [60](#)
- [76] KOCH, J., YU, T. M., GAMBETTA, J., HOUCK, A. A., SCHUSTER, D. I., MAJER, J., BLAIS, A., DEVORET, M. H., GIRVIN, S. M., AND SCHOELKOPF, R. J. Charge-insensitive qubit design derived from the cooper pair box. *Phys. Rev. A* 76 (Oct 2007), 042319. [2](#)
- [77] KOSKI, J. V., LANDIG, A. J., RUSS, M., ABADILLO-URIEL, J. C., SCARLINO, P., KRATOCHWIL, B., REICHL, C., WEGSCHEIDER, W., BURKARD, G., FRIESEN, M., ET AL. Strong photon coupling to the quadrupole moment of an electron in a solid-state qubit. *Nature Physics* 16, 6 (2020), 642–646. [102](#), [103](#)
- [78] KOUWENHOVEN, L. P., AUSTING, D. G., AND TARUCHA, S. Few-electron quantum dots. *Reports on Progress in Physics* 64, 6 (may 2001), 701–736. [17](#)
- [79] KOUWENHOVEN, L. P., VAN DER VAART, N. C., JOHNSON, A., KOOL, W., HARMANS, C., WILLIAMSON, J., STARING, A., AND FOXON, C. Single electron charging effects in semiconductor quantum dots. *Zeitschrift für Physik B Condensed Matter* 85, 3 (1991), 367–373. [17](#)
- [80] KROLL, J., BORSOI, F., VAN DER ENDEN, K., UILHOORN, W., DE JONG, D., QUINTERO-PÉREZ, M., VAN WOERKOM, D., BRUNO, A., PLISSARD, S., CAR, D., BAKKERS, E., CASSIDY, M., AND KOUWENHOVEN, L. Magnetic-field-resilient superconducting coplanar-waveguide resonators for hybrid circuit quantum electrodynamics experiments. *Phys. Rev. Applied* 11 (Jun 2019), 064053. [62](#)
- [81] KRUPKO, Y., NGUYEN, V. D., WEISSL, T., DUMUR, É., PUERTAS, J., DASSONNEVILLE, R., NAUD, C., HEKKING, F. W. J., BASKO, D. M., BUISSON, O., AND ROCH, N. Kerr nonlinearity in a superconducting Josephson metamaterial. *Physical Review Applied* 094516, 98 (2018), 1–12. [42](#)
- [82] LANDIG, A. J., KOSKI, J., SCARLINO, P., MENDES, U., BLAIS, A., REICHL, C., WEGSCHEIDER, W., WALLRAFF, A., ENSSLIN, K., AND IHN,



- T. Coherent spin-photon coupling using a resonant exchange qubit. *Nature* 560 (2018), 156–158. 4, 29
- [83] LEDUC, H. G., BUMBLE, B., DAY, P. K., EOM, B. H., GAO, J., GOLWALA, S., MAZIN, B. A., MCHUGH, S., MERRILL, A., MOORE, D. C., ET AL. Titanium nitride films for ultrasensitive microresonator detectors. *Applied Physics Letters* 97, 10 (2010), 102509. 9
- [84] LEVY, J. Universal quantum computation with spin-1/2 pairs and heisenberg exchange. *Phys. Rev. Lett.* 89 (Sep 2002), 147902. 106
- [85] LILES, S. D., MARTINS, F., MISEREV, D. S., KISELEV, A. A., THORVALDSON, I. D., RENDELL, M. J., JIN, I. K., HUDSON, F. E., VELDHORST, M., ITOH, K. M., SUSHKOV, O. P., LADD, T. D., DZURAK, A. S., AND HAMILTON, A. R. Electrical control of the  $g$  tensor of the first hole in a silicon mos quantum dot. *Phys. Rev. B* 104 (Dec 2021), 235303. 25, 35
- [86] LOSS, D., AND DIVINCENZO, D. P. Quantum computation with quantum dots. *Phys. Rev. A* 57 (Jan 1998), 120–126. 3
- [87] LUPAȘCU, A., SAITO, S., PICOT, T., DE GROOT, P., HARMANS, C., AND MOOIJ, J. Quantum non-demolition measurement of a superconducting two-level system. *nature physics* 3, 2 (2007), 119–123. 2
- [88] LUTTINGER, J. M., AND KOHN, W. Motion of electrons and holes in perturbed periodic fields. *Phys. Rev.* 97 (Feb 1955), 869–883. 25
- [89] MAJER, J., CHOW, J., GAMBETTA, J., KOCH, J., JOHNSON, B., SCHREIER, J., FRUNZIO, L., SCHUSTER, D., HOUCK, A. A., WALLRAFF, A., ET AL. Coupling superconducting qubits via a cavity bus. *Nature* 449, 7161 (2007), 443–447. 2
- [90] MARCELLINA, E., HAMILTON, A. R., WINKLER, R., AND CULCER, D. Spin-orbit interactions in inversion-asymmetric two-dimensional hole systems: A variational analysis. *Phys. Rev. B* 95 (Feb 2017), 075305. 28
- [91] MAURAND, R., JEHL, X., KOTEKAR-PATIL, D., CORNA, A., BOHUSLAVSKYI, H., LAVIÉVILLE, R., HUTIN, L., BARRAUD, S., VINET, M., SANQUER, M., AND DE FRANCESCHI, S. A CMOS silicon spin qubit. *Nature Communications* 7 (2016), 3–8. 3, 35
- [92] MCARDLE, S., ENDO, S., ASPURU-GUZIK, A., BENJAMIN, S. C., AND YUAN, X. Quantum computational chemistry. *Rev. Mod. Phys.* 92 (Mar 2020), 015003. 1
- [93] MCRÆ, C. R. H., WANG, H., GAO, J., VISSERS, M. R., BRECHT, T., DUNSWORTH, A., PAPPAS, D. P., AND MUTUS, J. Materials loss measurements using superconducting microwave resonators. *Review of Scientific Instruments* 91, 9 (2020), 091101. 63
- [94] MEGRANT, A., NEILL, C., BARENDS, R., CHIARO, B., CHEN, Y., FEIGL, L., KELLY, J., LUCERO, E., MARIANTONI, M., O’MALLEY, P. J. J., SANK, D., VAINSENER, A., WENNER, J., WHITE, T. C., YIN, Y.,

- ZHAO, J., PALMSTRØM, C. J., MARTINIS, J. M., AND CLELAND, A. N. Planar superconducting resonators with internal quality factors above one million. *Applied Physics Letters* 100, 11 (2012). 58
- [95] MI, X., BENITO, M., PUTZ, S., ZAJAC, D. M., TAYLOR, J. M., BURKARD, G., AND PETTA, J. R. A coherent spin-photon interface in silicon. *Nature* 555, 7698 (2018), 599–603. 4, 30, 76, 97, 103, 105
- [96] MI, X., CADY, J. V., ZAJAC, D. M., DEELMAN, P. W., AND PETTA, J. R. Strong coupling of a single electron in silicon to a microwave photon. *Science* 355, 6321 (2017), 156–158. 4, 24, 83
- [97] MI, X., CADY, J. V., ZAJAC, D. M., STEHLIK, J., EDGE, L. F., AND PETTA, J. R. Circuit quantum electrodynamics architecture for gate-defined quantum dots in silicon. *Applied Physics Letters* 110, 4 (2017), 18–21. 9, 65, 103, 106
- [98] MICHAL, V. P., ABADILLO-URIEL, J. C., ZIHLMANN, S., MAURAND, R., NIQUET, Y. M., AND FILIPPONE, M. Tunable hole spin-photon interaction based on g-matrix modulation. *arXiv 2204.00404* (2022). 9, 23, 28, 29, 100, 103, 106
- [99] MICHAL, V. P., VENITUCCI, B., AND NIQUET, Y.-M. Longitudinal and transverse electric field manipulation of hole spin-orbit qubits in one-dimensional channels. *Phys. Rev. B* 103 (Jan 2021), 045305. 28
- [100] MILLS, A., GUINN, C., GULLANS, M., SIGILLITO, A., FELDMAN, M., NIELSEN, E., AND PETTA, J. Two-qubit silicon quantum processor with operation fidelity exceeding 99%. *Science Advances* 8, 14 (2022). 1, 3
- [101] MILLS, A. R., ZAJAC, D. M., GULLANS, M. J., SCHUPP, F. J., HAZARD, T. M., AND PETTA, J. R. Shuttling a single charge across a one-dimensional array of silicon quantum dots. *Nature Communications* 10, 1 (2019). 34, 83
- [102] MLYNEK, J. A., ABDUMALIKOV, A. A., EICHLER, C., AND WALLRAFF, A. Observation of dicke superradiance for two artificial atoms in a cavity with high decay rate. *Nature communications* 5, 1 (2014), 1–6. 97
- [103] MUTTER, P. M., AND BURKARD, G. Cavity control over heavy-hole spin qubits in inversion-symmetric crystals. *Phys. Rev. B* 102 (Nov 2020), 205412. 29
- [104] MUTTER, P. M., AND BURKARD, G. Natural heavy-hole flopping mode qubit in germanium. *Phys. Rev. Research* 3 (Feb 2021), 013194. 4, 29, 106
- [105] NIEPCE, D., BURNETT, J., AND BYLANDER, J. High kinetic inductance NbN nanowire superinductors. *Phys. Rev. Applied* 11 (Apr 2019), 044014. 9
- [106] NIGG, S. E., FUHRER, A., AND LOSS, D. Superconducting grid-bus surface code architecture for hole-spin qubits. *Phys. Rev. Lett.* 118 (Apr 2017), 147701. 4

- [107] NIQUET, Y. M., HUTIN, L., DIAZ, B. M., VENITUCCI, B., LI, J., MICHAL, V., FERNÁNDEZ-BADA, G. T., JACQUINOT, H., AMISSE, A., APRA, A., EZZOUCH, R., PIOT, N., VINCENT, E., YU, C., ZIHLMANN, S., BRUN-BARRIÈRE, B., SCHMITT, V., DUMUR, E., MAURAND, R., JEHL, X., SANQUER, M., BERTRAND, B., RAMBAL, N., NIEBOJEWSKI, H., BEDECARRATS, T., CASSÉ, M., CATAPANO, E., MORTEMOUSQUE, P. A., THOMAS, C., THONNART, Y., BILLIOT, G., MOREL, A., CHARBONNIER, J., PALLEGOIX, L., NIEGEMANN, D., KLEMT, B., URDAMPILLETA, M., EL HOMS Y, V., NURIZZO, M., CHANRION, E., JADOT, B., SPENCE, C., THINEY, V., PAZ, B., DE FRANCESCHI, S., VINET, M., AND MEUNIER, T. Challenges and perspectives in the modeling of spin qubits. In *2020 IEEE International Electron Devices Meeting (IEDM)* (2020), pp. 30.1.1–30.1.4.
- [108] NOIRI, A., TAKEDA, K., NAKAJIMA, T., KOBAYASHI, T., SAMMAK, A., SCAPPUCCI, G., AND TARUCHA, S. Fast universal quantum gate above the fault-tolerance threshold in silicon. *Nature* *601*, 7893 (2022), 338–342. [1](#), [3](#)
- [109] O’CONNELL, A. D., ANSMANN, M., BIALCZAK, R. C., HOFHEINZ, M., KATZ, N., LUCERO, E., MCKENNEY, C., NEELEY, M., WANG, H., WEIG, E. M., ET AL. Microwave dielectric loss at single photon energies and millikelvin temperatures. *Applied Physics Letters* *92*, 11 (2008), 112903. [63](#)
- [110] PETERSSON, K. D., McFAUL, L. W., SCHROER, M. D., JUNG, M., TAYLOR, J. M., HOUCK, A. A., AND PETTA, J. R. Circuit quantum electrodynamics with a spin qubit. *Nature* *490*, 7420 (2012), 380–383. [3](#), [23](#)
- [111] PETTA, J. R., JOHNSON, A. C., TAYLOR, J. M., LAIRD, E. A., YACOBY, A., LUKIN, M. D., MARCUS, C. M., HANSON, M. P., AND GOSSARD, A. C. Coherent manipulation of coupled electron spins in semiconductor quantum dots. *Science* *309*, 5744 (2005), 2180–2184. [3](#)
- [112] PHILIPS, S. G., MAȢZIK, M. T., AMITONOV, S. V., DE SNOO, S. L., RUSS, M., KALHOR, N., VOLK, C., LAWRIE, W. I., BROUSSE, D., TRYPUTEN, L., ET AL. Universal control of a six-qubit quantum processor in silicon. *arXiv 2202.09252* (2022). [3](#)
- [113] PIORO-LADRIERE, M., OBATA, T., TOKURA, Y., SHIN, Y.-S., KUBO, T., YOSHIDA, K., TANIYAMA, T., AND TARUCHA, S. Electrically driven single-electron spin resonance in a slanting zeeman field. *Nature Physics* *4*, 10 (2008), 776–779. [28](#)
- [114] PIOT, N., BRUN, B., SCHMITT, V., ZIHLMANN, S., MICHAL, V. P., APRA, A., ABADILLO-URIEL, J. C., JEHL, X., BERTRAND, B., NIEBOJEWSKI, H., HUTIN, L., VINET, M., URDAMPILLETA, M., MEUNIER, T., NIQUET, Y. M., MAURAND, R., AND DE FRANCESCHI, S. A single hole spin with enhanced coherence in natural silicon. *arXiv 2201.08637* (2022). [24](#), [25](#), [89](#), [92](#)
- [115] PIRANDOLA, S., ANDERSEN, U. L., BANCHI, L., BERTA, M., BUNANDAR, D., COLBECK, R., ENGLUND, D., GEHRING, T., LUPO, C., OTTAVIANI, C., PEREIRA, J. L., RAZAVI, M., SHAARI, J. S., TOMAMICHEL,

- M., USENKO, V. C., VALLONE, G., VILLORESI, P., AND WALLDEN, P. Advances in quantum cryptography. *Adv. Opt. Photon.* *12*, 4 (Dec 2020), 1012–1236. [1](#)
- [116] PONCHAK, G., PAPAPOLYMEROU, J., AND TENTZERIS, M. Excitation of coupled slotline mode in finite-ground cpw with unequal ground-plane widths. *IEEE Transactions on Microwave Theory and Techniques* *53*, 2 (2005), 713–717. [68](#)
- [117] POZAR, D. M. *Microwave Engineering*. Wiley, 2011. [6](#), [7](#), [11](#), [60](#), [66](#), [119](#), [120](#), [121](#), [122](#), [123](#)
- [118] RABI, I. I. On the process of space quantization. *Phys. Rev.* *49* (Feb 1936), 324–328. [14](#)
- [119] RUSS, M., GINZEL, F., AND BURKARD, G. Coupling of three-spin qubits to their electric environment. *Phys. Rev. B* *94* (Oct 2016), 165411. [102](#)
- [120] SACÉPÉ, B. *Spectroscopie tunnel dans des films minces proche de la transition supraconducteur-isolant*. PhD thesis, University Grenoble Alpes, 2007. [42](#)
- [121] SAGE, J. M., BOLKHOVSKY, V., OLIVER, W. D., TUREK, B., AND WELANDER, P. B. Study of loss in superconducting coplanar waveguide resonators. *Journal of Applied Physics* *109*, 6 (2011), 063915. [9](#)
- [122] SAM-GIAO, D., POUGET, S., BOUGEROL, C., MONROY, E., GRIMM, A., JEBARI, S., HOFHEINZ, M., GÉRARD, J.-M., AND ZWILLER, V. High-quality nbn nanofilms on a gan/aln heterostructure. *AIP Advances* *4*, 10 (2014), 107123. [40](#)
- [123] SAMKHARADZE, N., BRUNO, A., SCARLINO, P., ZHENG, G., DIVINCENZO, D. P., DICARLO, L., AND VANDERSYPEN, L. M. K. High-kinetic-inductance superconducting nanowire resonators for circuit qed in a magnetic field. *Phys. Rev. Applied* *5* (Apr 2016), 044004. [9](#), [60](#)
- [124] SAMKHARADZE, N., ZHENG, G., KALHOR, N., BROUSSE, D., SAMMAK, A., MENDES, U. C., BLAIS, A., SCAPPUCCI, G., AND VANDERSYPEN, L. M. K. Strong spin-photon coupling in silicon. *Science* *359*, 6380 (2018), 1123–1127. [4](#), [9](#), [30](#), [76](#), [97](#), [103](#), [105](#)
- [125] SCAPPUCCI, G., KLOEFFEL, C., ZWANENBURG, F. A., LOSS, D., MYRONOV, M., ZHANG, J.-J., DE FRANCESCHI, S., KATSAROS, G., AND VELDHORST, M. The germanium quantum information route. *Nature Reviews Materials* *6*, 10 (2021), 926–943. [3](#)
- [126] SCARLINO, P., UNGERER, J. H., VAN WOERKOM, D. J., MANCINI, M., STANO, P., MULLER, C., LANDIG, A. J., KOSKI, J. V., REICHL, C., WEGSCHEIDER, W., IHN, T., ENSSLIN, K., AND WALLRAFF, A. In-situ tuning of the electric dipole strength of a double dot charge qubit: Charge noise protection and ultra strong coupling, 2021. [83](#), [103](#)

- [127] SCHUSTER, D., HOUCK, A. A., SCHREIER, J., WALLRAFF, A., GAMBETTA, J., BLAIS, A., FRUNZIO, L., MAJER, J., JOHNSON, B., DEVORET, M., ET AL. Resolving photon number states in a superconducting circuit. *Nature* 445, 7127 (2007), 515–518. [106](#)
- [128] SHEARROW, A., KOOLSTRA, G., WHITELEY, S. J., EARNEST, N., BARRY, P. S., HEREMANS, F. J., AWSCHALOM, D. D., SHIROKOFF, E., AND SCHUSTER, D. I. Atomic layer deposition of titanium nitride for quantum circuits. *Applied Physics Letters* 113, 21 (2018), 212601. [9](#)
- [129] SHOR, P. Algorithms for quantum computation: discrete logarithms and factoring. In *Proceedings 35th Annual Symposium on Foundations of Computer Science* (1994), pp. 124–134. [1](#)
- [130] SIMMONS, C., PRANCE, J., VAN BAEL, B., KOH, T. S., SHI, Z., SAVAGE, D., LAGALLY, M., JOYNT, R., FRIESEN, M., COPPERSMITH, S., ET AL. Tunable spin loading and t 1 of a silicon spin qubit measured by single-shot readout. *Physical review letters* 106, 15 (2011), 156804. [3](#)
- [131] SIMONS, R. N. *Coplanar Waveguide Circuits, Components, and Systems*. John Wiley & Sons, Inc., 2001. [8](#), [118](#)
- [132] STOCKKLAUSER, A., SCARLINO, P., KOSKI, J. V., GASPARINETTI, S., ANDERSEN, C. K., REICHL, C., WEGSCHEIDER, W., IHN, T., ENSSLIN, K., AND WALLRAFF, A. Strong coupling cavity qed with gate-defined double quantum dots enabled by a high impedance resonator. *Phys. Rev. X* 7 (Mar 2017), 011030. [4](#), [23](#), [24](#), [76](#), [83](#), [103](#)
- [133] SUCHOI, O., ABDO, B., SEGEV, E., SHTEMPLUCK, O., BLENOWE, M. P., AND BUKS, E. Intermode dephasing in a superconducting stripline resonator. *Phys. Rev. B* 81 (May 2010), 174525. [117](#)
- [134] SZE, S. M., LI, Y., AND NG, K. K. *Physics of semiconductor devices*. John wiley & sons, 2007. [73](#)
- [135] TINKHAM, M. *Introduction to superconductivity*. Dover Publications Inc., 2004. [9](#), [44](#)
- [136] TRIF, M., GOLOVACH, V. N., AND LOSS, D. Spin dynamics in inas nanowire quantum dots coupled to a transmission line. *Phys. Rev. B* 77 (Jan 2008), 045434. [4](#), [29](#)
- [137] TYRYSHKIN, A. M., TOJO, S., MORTON, J. J., RIEMANN, H., ABROSI-MOV, N. V., BECKER, P., POHL, H.-J., SCHENKEL, T., THEWALT, M. L., ITOH, K. M., ET AL. Electron spin coherence exceeding seconds in high-purity silicon. *Nature materials* 11, 2 (2012), 143–147. [1](#), [3](#), [24](#)
- [138] VAN DER WIEL, W. G., DE FRANCESCHI, S., ELZERMAN, J. M., FUJISAWA, T., TARUCHA, S., AND KOUWENHOVEN, L. P. Electron transport through double quantum dots. *Rev. Mod. Phys.* 75 (Dec 2002), 1–22. [17](#)
- [139] VANDERSYPEN, L., BLUHM, H., CLARKE, J., DZURAK, A. S., ISHIHARA, R., MORELLO, A., REILLY, D., SCHREIBER, L., AND VELDHOST, M.

- Interfacing spin qubits in quantum dots and donors-hot, dense, and coherent. *npj Quantum Information* 3, 34 (2017). [1](#), [2](#), [34](#)
- [140] VANDERSYPEN, L. M., STEFFEN, M., BREYTA, G., YANNONI, C. S., SHERWOOD, M. H., AND CHUANG, I. L. Experimental realization of shor’s quantum factoring algorithm using nuclear magnetic resonance. *Nature* 414, 6866 (2001), 883–887. [1](#)
- [141] VANELDIK, J. F., WESTRA, K. L., ROUTLEDGE, D., AND BRETT, M. J. Target hysteresis and film properties of sputtered NbN. *Journal of Physics D: Applied Physics* 22, 11 (nov 1989), 1788–1790. [40](#)
- [142] VASYUTIN, M., KUZ’MICHEV, N., AND SHILKIN, D. Upper critical field of niobium nitride thin films. *Physics of the Solid State* 58, 2 (2016), 236–239. [44](#)
- [143] VELDHORST, M., YANG, C. H., HWANG, J. C. C., HUANG, W., DEHOLLAIN, J. P., MUHONEN, J. T., SIMMONS, S., LAUCHT, A., HUDSON, F. E., ITOH, K. M., MORELLO, A., AND DZURAK, A. A two-qubit logic gate in silicon. *Nature* 526 (2015), 410–414. [3](#), [34](#)
- [144] VENITUCCI, B., BOURDET, L., POUZADA, D., AND NIQUET, Y.-M. Electrical manipulation of semiconductor spin qubits within the  $g$ -matrix formalism. *Phys. Rev. B* 98 (Oct 2018), 155319. [25](#)
- [145] VIENNOT, J. J., DARTAILH, M. C., COTTET, A., AND KONTOS, T. Coherent coupling of a single spin to microwave cavity photons. *Science* 349, 6246 (2015), 408–411. [30](#)
- [146] VIENNOT, J. J., DELBECQ, M. R., DARTAILH, M. C., COTTET, A., AND KONTOS, T. Out-of-equilibrium charge dynamics in a hybrid circuit quantum electrodynamics architecture. *Phys. Rev. B* 89 (Apr 2014), 165404. [83](#)
- [147] VOISIN, B., MAURAND, R., BARRAUD, S., VINET, M., JEHL, X., SANQUER, M., RENARD, J., AND DE FRANCESCHI, S. Electrical control of  $g$ -factor in a few-hole silicon nanowire mosfet. *Nano Letters* 16, 1 (2016), 88–92. PMID: 26599868. [25](#)
- [148] WALLRAFF, A., SCHUSTER, D. I., BLAIS, A., FRUNZIO, L., HUANG, R.-S., MAJER, J., KUMAR, S., GIRVIN, S. M., AND SCHOELKOPF, R. J. Strong coupling of a single photon to a superconducting qubit using circuit quantum electrodynamics. *Nature* 431, 7005 (2004), 162–167. [105](#)
- [149] WANG, Z., KAWAKAMI, A., UZAWA, Y., AND KOMIYAMA, B. Superconducting properties and crystal structures of single-crystal niobium nitride thin films deposited at ambient substrate temperature. *Journal of applied physics* 79, 10 (1996), 7837–7842. [44](#)
- [150] WATSON, T., PHILIPS, S., KAWAKAMI, E., WARD, D., SCARLINO, P., VELDHORST, M., SAVAGE, D., LAGALLY, M., FRIESEN, M., COPPERSMITH, S., ET AL. A programmable two-qubit quantum processor in silicon. *Nature* 555, 7698 (2018), 633–637. [3](#), [34](#)

- [151] WERTHAMER, N. R., HELFAND, E., AND HOHENBERG, P. C. Temperature and purity dependence of the superconducting critical field,  $H_{c2}$ . iii. electron spin and spin-orbit effects. *Phys. Rev.* *147* (Jul 1966), 295–302. [43](#)
- [152] WINKLER, R. *Spin—Orbit Coupling Effects in Two-Dimensional Electron and Hole Systems*. Springer Berlin Heidelberg, 2003. [25](#)
- [153] XIAO, M., HOUSE, M., AND JIANG, H. W. Measurement of the spin relaxation time of single electrons in a silicon metal-oxide-semiconductor-based quantum dot. *Physical review letters* *104*, 9 (2010), 096801. [3](#)
- [154] XUE, X., RUSS, M., SAMKHARADZE, N., UNDSETH, B., SAMMAK, A., SCAPPUCCI, G., AND VANDERSYPEN, L. M. Quantum logic with spin qubits crossing the surface code threshold. *Nature* *601*, 7893 (2022), 343–347. [1](#), [3](#)
- [155] YONEDA, J., TAKEDA, K., OTSUKA, T., NAKAJIMA, T., DELBECQ, M. R., ALLISON, G., HONDA, T., KODERA, T., ODA, S., HOSHI, Y., ET AL. A quantum-dot spin qubit with coherence limited by charge noise and fidelity higher than 99.9%. *Nature nanotechnology* *13*, 2 (2018), 102–106. [3](#), [34](#)
- [156] YU, C., ZIHLMANN, S., BERTRAND, B., AND MAURAND, R. Si hole qubits in a cqed architecture. *Bulletin of the American Physical Society* *67* (2022).
- [157] YU, C. X., ZIHLMANN, S., ABADILLO-URIEL, J. C., MICHAL, V. P., RAMBAL, N., NIEBOJEWSKI, H., BEDECARRATS, T., VINET, M., DUMUR, E., FILIPPONE, M., ET AL. Strong coupling between a photon and a hole spin in silicon. *arXiv preprint arXiv:2206.14082* (2022).
- [158] YU, C. X., ZIHLMANN, S., TRONCOSO FERNÁNDEZ-BADA, G., THOMASSIN, J.-L., DUMUR, É., MAURAND, R., AND TRONCOSO, G. Magnetic field resilient high kinetic inductance superconducting niobium nitride coplanar waveguide resonators. *Applied Physics Letters* *118*, 054001 (2021).
- [159] ZAJAC, D. M., HAZARD, T. M., MI, X., NIELSEN, E., AND PETTA, J. R. Scalable gate architecture for a one-dimensional array of semiconductor spin qubits. *Phys. Rev. Applied* *6* (Nov 2016), 054013. [34](#)
- [160] ZAJAC, D. M., SIGILLITO, A. J., RUSS, M., BORJANS, F., TAYLOR, J. M., BURKARD, G., AND PETTA, J. R. Resonantly driven cnot gate for electron spins. *Science* *359*, 6374 (2018), 439–442. [34](#)
- [161] ZHANG, W., KALASHNIKOV, K., LU, W.-S., KAMENOV, P., DiNAPOLI, T., AND GERSHENSON, M. Microresonators fabricated from high-kinetic-inductance aluminum films. *Phys. Rev. Applied* *11* (Jan 2019), 011003. [9](#)